Hydrodynamics of Cardiac Diastole

Kelley Christine Stewart

Dissertation submitted to the faculty of the Virginia Polytechnic Institute and State University in partial fulfillment of the requirements for the degree of

Doctor of Philosophy

In

Mechanical Engineering

Pavlos Vlachos (Committee Chair)

Kenneth Ball

Sunghwan Jung

William Little

Mark Paul

Anne Staples

3.30.2011

Blacksburg, Virginia

Key words: vortex rings, diastole, echocardiography, heart failure, particle image velocimetry

Hydrodynamics of Cardiac Diastole

Kelley Christine Stewart

Abstract

Left ventricular diastole (filling) is a complex process with many features and coupled compensatory mechanisms which coordinate to maintain optimal filling and ejection of the left ventricle. Diastolic filling is controlled by the left ventricular recoil, relaxation, and compliance as well as atrial and ventricular pressures making left ventricular diastolic dysfunction very difficult to understand and diagnose. An improved understanding of these unique flows is important to both the fundamental mechanics of the cardiac diastolic filling as well as the development of novel and accurate diagnostic techniques.

This work includes studies of in-vivo and in-vitro vortex rings. Vortex rings created in the left ventricle past the mitral valve during diastole are produced in a confined domain and are influenced by the left ventricular walls. Therefore, an in-vitro analysis of the formation and decay of vortex rings within confined cylindrical domains using particle image velocimetry was conducted. Varying mechanisms of vortex ring breakdown were observed over a wide range of Reynolds numbers, and an analytical model for vortex ring circulation decay of laminar vortex rings was developed. Also, in this work a novel method for analyzing color M-mode echocardiography data using a newly developed automated algorithm is introduced which examines the pressure gradients and velocities within the left ventricle. From this analysis, a new diagnostic filling parameter is introduced which displays a greater probability of detection of diastolic dysfunction over the conventionally used diagnostic parameter.

Acknowledgements

There are many people that I would like to thank for their help, support, and encouragement throughout my time at Virginia Tech. First, I would like to thank the National Science Foundation for granting me the Graduate Research Fellowship and funding three years of my research at Virginia Tech and allowing me to pursue research opportunities that I may not have otherwise been able.

I would like to thank my advisor Dr. Pavlos Vlachos for helping me learn and grow throughout this process. I appreciate your mentorship, support, and encouragement. I would also like to thank my committee members Dr. Kenneth Ball, Dr. Sunghwan Jung, Dr. William Little, Dr. Mark Paul, and Dr. Anne Staples for your support and suggestions throughout this work. I would especially like to thank Dr. William Little, Dr. Rahul Kumar, and Dr. Takahiro Ohara at Wake Forest Baptist Medical Center for being mentors. You have given us the valuable insight into the medical field that helped to strengthen this work. This work would not have been possible without your contributions.

Thank you to my friends and colleagues in the AEThER Lab both past and present who have helped me in many ways. You have been some of my best friends here and we have supported each other through successes and failures. I would like to thank John Charonko and Cassie Neibel for your help and support on this project. I would especially like to thank Chris Weiland, thank you for supporting and encouraging me over the past few years. I really appreciate the time I have spent with all of you.

Last but not least, I would like to thank my family for consistently being a source of love, inspiration, and encouragement. To my parents, thank you for always being my greatest supporters and believing in me every step of the way. Without your leadership I would not be the person that I am today.

Attribution

This dissertation is composed of an introduction, background chapter, conclusion and four main chapters. These four chapters are written in journal format and will each be submitted to archival journals for separate publication. The following individuals are co-authors on one or more chapters.

Dr. Pavlos P. Vlachos, Ph.D. – (Associate Professor in Mechanical Engineering, Virginia Tech.) is the committee chair and has provided advice on the works presented in each chapter. Dr. Vlachos is a co-author on each of the papers.

Dr. William C. Little, M.D. – (Cardiology Section Head, Wake Forest Baptist Health Sciences) Dr. Little is a committee member who has provided considerable help and insight to our work on left ventricular diastolic dysfunction. Dr. Little is a co-author on Chapters 5 and 6.

Dr. John J. Charonko, Ph.D._– (Research Assistant Professor in Mechanical Engineering, Virginia Tech) Dr. Charonko helped substantially with the initial development of the automated algorithm for the analysis of color M-mode echocardiograms presented in Chapter 6 as well as throughout the entire progression of the work on left ventricular diastolic dysfunction. Dr. Charonko is a co-author on Chapters 5 and 6.

Dr. Sunghwan Jung, Ph.D. – (Assistant Professor in Engineering Science and Mechanics, Virginia Tech) Dr. Jung is a committee member who developed the analytical model presented in Chapter 4 as well as provided help and advice for the work in Chapter 4. Dr. Jung is a co-author on Chapter 4.

Dr. Rahul Kumar, M.D. – (Cardiology Fellow, Wake Forest Baptist Health Sciences) Dr. Kumar acquired the majority of the clinical patient data used in Chapters 5 and 6 as well as significantly helped in analysis of color M-mode echocardiograms. Dr. Kumar is a co-author on Chapter 6.

Dr. Takahiro Ohara, M.D., Ph.D. – (Postdoctoral Research Fellow, Wake Forest Baptist Health Sciences) Dr. Ohara helped in acquiring clinical patient data used in Chapter 6. Dr. Ohara is a co-author on Chapter 6.

Casandra L. Niebel - (Masters Student in Mechanical Engineering, Virginia Tech) Cassie helped to acquire the experimental data used in Chapter 4 and has helped in the progression of the left ventricular diastolic dysfunction work presented in Chapter 5. Cassie is a co-author on Chapters 4 and 5.

Table of Contents

List of Figures

List of Tables

1 Introduction

1.1 Motivation

Left ventricular (LV) diastolic dysfunction and diastolic heart failure are disease conditions associated with the filling dynamics of the heart and may affect up to 27% of the general population [1]. Although this condition is very prevalent, it currently remains difficult to diagnose due to inherent atrio-ventricular compensatory mechanisms including increased heart rate, increased LV contractility, and increased left atrial (LA) pressure. A greater comprehension of the governing flow physics in the LV as the heart remodels has the potential to substantially increase the understanding of the progression of diastolic dysfunction and in-turn advance the diagnostic techniques.

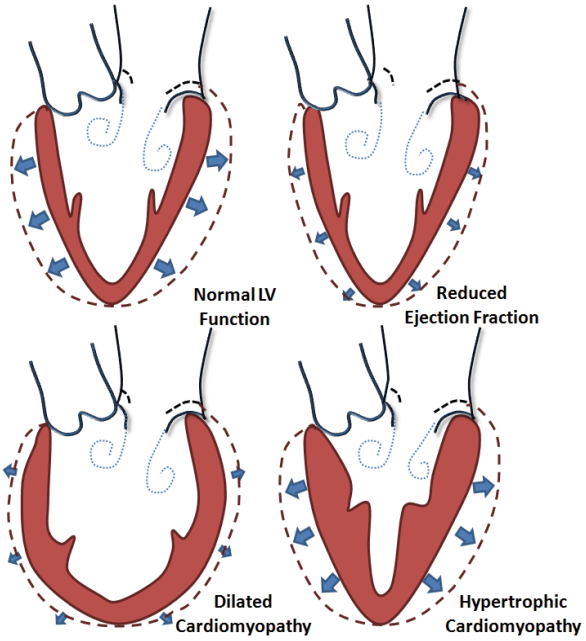

Figure 1.1: Illustration of a range of diastolic filling pathologies

It is well known that a vortex ring forms during left ventricular early filling. Previous researchers have experimentally examined vortex rings within mock ventricles; however a fundamental understanding of confined vortex ring dynamics has not been previously established. Also, vortex rings generated within the ventricle have been compared to vortex rings generated within semi-infinite domains, which is very different than physiological conditions. Vortex rings created in the left ventricle past the mitral valve are produced in a confined domain and are influenced by the LV walls. In this work vortex rings were generated in both confined and unconfined cylindrical domains using a piston cylinder arrangement. We compared the formation and decay of vortex rings generated within confined cylindrical domains with vortex rings created in a semi-infinite downstream volume. Although this work is crucial to the understanding of vortex ring dynamics, the flow within the left ventricle past the mitral valve orifice cannot be entirely represented by these ideal conditions.

Additionally, we hypothesized that there is a correlation between the early diastolic development of a zero pressure difference within the left ventricle and the dynamics of vortex formation past the mitral annulus. Here we discovered that the first onset of the lack of a favorable pressure difference within the

ventricle at the time when the early filling wave deceleration was observed and we show that the left ventricular vortex ring pinch-off occurred simultaneously. In contrast to previous perception, this work shows that the vortex ring pinch-off occurs before the completion of early diastole and its formation time remains invariant to changes of diastolic function. From this analysis we found that early left ventricular filling is not accurately represented with a single propagation velocity, as is conventionally analyzed. Instead, blood rapidly flows into the LV in response to an early diastolic LA to LV pressure gradient which extends a variable distance into the ventricle. We proved that there exists a relationship between the deceleration of the filling and the onset of the loss of a favorable pressure difference within the LV, representing the physical mechanism driving the filling which is universal and independent of filling pathology (Figure 1.2). We found that early diastolic flow propagation occurs with an initial rapid velocity that abruptly decelerates to a terminal velocity. With diastolic dysfunction, the initial velocity is slower and the deceleration point occurs closer to the mitral annulus than with normal filling. A new parameter was developed which combines these two effects and provides a more accurate assessment of diastolic function than the conventional propagation velocity.

1.2 Objective and Structure of Dissertation

The objective of this dissertation was to prove the existence of the relationship between intraventricular pressure differences and the deceleration of early diastolic filling velocity and unravel its mechanics. In this work we further investigated the roll of vortex ring dynamics in the decline of diastolic function and in relationship with the development the loss of a favorable pressure difference within the ventricle. This objective was achieved through integrated analysis of clinical and in-vitro experimental vortex ring analysis. Finally, we developed a new diastolic filling parameter and demonstrated its potential clinical utility.

Each of the four main chapters within this dissertation, chapters 3 through 6, is written in individual journal article format so that each chapter may stand alone for publication. For this reason, some of the background, methodology, and figures within these chapters overlap one another. Chapters 1 and 7 provide an introduction and conclusion and chapter 2 provides an in-depth literature review for the overall work. The main body of the dissertation is divided into two main sections. The first section, chapters 3 and 4, includes the analysis of radially confined vortex ring studies. This section investigates the vortex ring formation and decay of radially confined vortex rings produced with a variety of Reynolds numbers. An improved understanding of the dynamics within simple radially confined domains is essential in order to fully comprehend the role of vortex rings in diastolic filling. The second section includes the analysis of clinical in-vivo color M-mode echocardiography data. This section, Chapters 5

and 6 reveals that the left ventricular vortex ring pinch-off is physically responsible for the deceleration of the diastolic filling wave and also introduces a novel diastolic parameter which may potentially improve current LVDD diagnostic techniques.

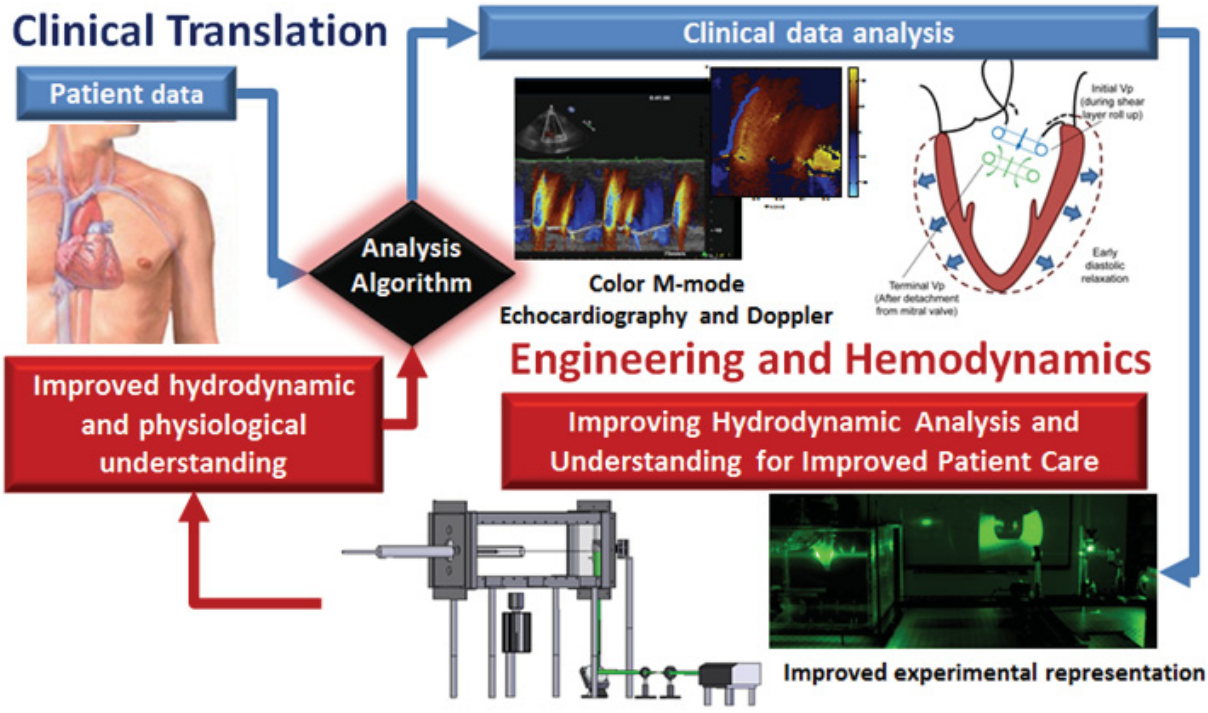

Figure 1.2: Illustration of the dissertation objective: Improved understanding of the progression of diastolic dysfunction by analyzing both clinical and experimental data. (Chest and heart schematic in top left of composite image is used from Medtronic Ablation Frontiers (www.ablationfrontiers.com/us/faq.html))

1.2.1 Statement of Originality

This work introduces a unique analysis of diastolic dysfunction by integrating clinical one-dimensional and experimental high temporal and spatial resolution data. Our studies, for the first time, comprehensively evaluated the physical basis for early diastolic LV filling using an objective CMM quantification methodology and provided a novel, improved measure of LV suction. We departed from

the conventional understanding, which assumes that early diastole occurs with a constant propagation velocity, and recognized the occurrence of an abrupt deceleration during the filling and its association with the development of an adverse pressure gradient. The novel early filling strength parameter and pressure driven deceleration point within early diastolic filling can also be found for higher dimensional clinical data such as MRI.

In addition to the development of a clinical diagnostic parameter and improved understanding of diastolic filling, advancements of fundamental fluid dynamics were obtained by researching wall bounded vortex ring formation and decay for the first time. This research has the potential to influence future studies of left ventricular diastole as well as many other non-biological circumstances.

2 Background

Diastole is the period of the cardiac cycle from the aortic valve closure to the mitral valve closure and contains four parts: isovolumetric relaxation, early rapid diastolic filling, diastasis, and atrial contraction [1]. The early rapid diastolic filling or E-wave, is controlled by the left ventricular recoil, relaxation, and compliance, creating an atrio-ventricular pressure difference which causes blood to accelerate from the left atrium (LA) into the left ventricle (LV) through the mitral valve (MV). The atrial contraction creates the second filling wave, A-wave, where the LA contracts and forces blood from the LA into the LV. Many cardiovascular conditions including aging, coronary artery disease, hypertension, dilated cardiomyopathy and restrictive cardiomyopathy have impaired relaxation, altered LV filling dynamics and elevation of left atrial pressure [2, 3]. This condition decreases the effectiveness of early diastole, forcing an increase in the atrial contraction to compensate for the reduced filling during early diastole.

Diastolic dysfunction is rated by severity from stage 0, healthy filling, to stage 3, restrictive filling. As the diastolic function decreases the ventricular relaxation, left ventricular recoil, and left ventricular compliance decrease [4, 5]. In diseased patients, a decrease in the early diastolic relaxation in addition to a decreased compliance of the LV inhibits the LV from filling normally; the left atrium must increase its pressure and force the blood into the LV [4, 6]. Diastolic function is dependent on the interplay among the LV relaxation, LV recoil, LV compliance, and filling pressures [1, 7, 8] and is therefore difficult to diagnose.

2.1 Assessment of LVDD

2.1.1 Echocardiography

Color M-mode (CMM) Echocardiography has emerged as an extremely useful tool for the noninvasive assessment of patients with cardiovascular diseases including diastolic dysfunction. This technology allows users to measure the velocities within the LV along a scanline aligned with the mitral to apical inflow tract [2, 9]. The propagation velocity (Vp) and the early (E) and atrial (A) velocity magnitudes and durations can be calculated from CMM imaging. Brun et al. first determined the propagation velocity of early diastolic filling using color M-mode echocardiography images by tracking the slope of a line fit to the leading edge of the E-wave, where the CMM image velocity contour begins [9]. Brun et al. demonstrated a strong correlation between propagation velocity and wall relaxation, and he showed a trend of decreasing Vp and consequently wall relaxation as diastolic dysfunction increases

[3, 9]. Similarly, the propagation velocity is often found by measuring the slope of the first color aliasing boundary on the CMM image [10].

Although the conventionally used technique for calculating Vp is very similar to Brun et al.'s original method, many researchers have proposed slight variations. Takatsuji et al. determined the filling wave propagation velocity from color M-mode images using a more complex method. The slope was determined by the point of maximum velocity at the mitral valve and the point at the mid ventricle where the velocity decreased to seventy percent of the maximum velocity [11]. In studies by Yotti et al. and by De Mey et al. the propagation speed was found by creating a line along the fifty percent isovelocity contour on the leading edge of the E-wave [12, 13]. The majority of these methods are manual and dependent upon the interpretation and experience of the clinician performing the test [3]. A semi-automated approach was proposed by Stuggard et al. using eigenvector analysis of the CMM E-wave to calculate the principal components and reconstruct an ellipse representing the E-wave. The angle of rotation of the ellipse was calculated to determine the Vp [14]. The E-wave and A-wave Vp values have also been studied together to determine a diagnostic parameter based on the ratio of these velocities by Parthenakis et al. The study found a stronger correlation between the ratio of propagation velocities to diastolic dysfunction stage than either of the propagation velocities individually [15]. Unfortunately, there is no universally accepted method for calculating Vp. Common methods estimate Vp using isovelocity contours [9, 11, 12] or eigenvector analysis [14] however these methods are inadequate for characterizing diastolic function [16].

Another clinically measured parameter used for diagnosis is the ratio of peak transmitral E-wave inflow velocity (E) to the peak transmitral A-wave inflow velocity (A) which has shown a biphasic filling pattern that depends on age and heart rate. The transmitral velocity ratio also does not significantly distinguish healthy patients from pseudonormal patients [17-19]. The relationship between E-wave peak transmitral flow velocity and the E-wave mitral annulus velocity (E/E') from Doppler tissue imaging has also been used as an indication for diastolic dysfunction by estimating the LV filling pressures with fairly good success [20, 21]. Ommen et al. found that an E/E' value of less than 8 most likely corresponds to a patient with healthy LV diastolic pressures; whereas an E/E' value greater than 15 is associated with increased pressures [21, 22]. In Ommen's study the range of E/E' values between 8 and 15 showed great variability between healthy and elevated pressures.

Despite the great interest and previous efforts there is no standardization of the clinical calculation of the Vp and there is debate about the proper estimation methods [7, 16, 23]. In addition, most current methods for calculating Vp use a single isovelocity contour to estimate a linear slope [24]. This is subject to variations in the estimated Vp caused by noise or artifacts within the contour. More

importantly, characterizing Vp with a single linear slope is physically inappropriate because the filling wave velocity continuously varies throughout diastole. Previous studies reported changes in the wave filling speed; however, this information was not accounted for in the calculation of Vp [7, 25, 26].

2.1.2 Pressure Analysis

The pressures within the LV during the E-wave are crucial for understanding the fluid dynamics of early filling. Measuring pressure magnitudes within the LV is an invasive procedure and is not often performed in routine evaluations [27]. Pulmonary capillary wedge pressure (PCWP) is an invasive measurement of the left atrial pressure and is recognized as a clinical standard for estimating left ventricular filing pressure [28], but this technique is associated with complications and risks, especially in critically ill patients [29, 30]. The intraventricular pressure difference between the ventricular apex and the atrium is more commonly calculated to evaluate LV function [31-35]. Diastolic suction, the intraventricular pressure difference between the ventricular apex and the atrium, is another important factor in LV function [12, 32, 35] but this parameter does not incorporate an overall rise in the ventricular and apical pressures. The velocity scanlines at each time step within a diastolic cycle represent the spatio-temporal velocity distribution and can be utilized to calculate the pressure field by using the Euler equation [1, 5, 6, 12, 36]. This analysis results in relative pressures between the mitral valve location and the apical position of the LV. Any inaccuracies within the CMM velocity values, caused by misalignment in the CMM scanline, can translate into errors in the calculated pressure differences. However, Greenberg et al. concluded that a scanline positioned within the center 60% of the mitral valve will generate resultant values with a very small error, due to misalignment, compared to actual values [36-38]. Therefore, the accuracy is not diminished by the typically encountered variations in the position of the scanning line [32].

Using CMM and the Euler equation Yotti et al. calculated IVPD for healthy patients and patients with dilated cardiomyopathy (DCM). The healthy patients had a mean IVPD of 2.5 mmHg whereas the IVPD for patients with dilated cardiomyopathy was 1.2 mmHg (Yotti, Bermejo et al. 2005). They also examined the spatial pressure distribution along the length of the LV. The IVPD for healthy patients was found to be larger than the IVPD for DCM patients. The filling pressure waveform was found to be different for the two filling types. The healthy patients have a constantly increasing pressure relative to the LV base along the ventricular length, whereas the DCM patients have a relative pressure that increased more suddenly and then remained constant for the remainder of the LV (Yotti, Bermejo et al. 2005). Popović et al. calculated the LVPD in young healthy patients and sedentary elderly patients. The range of IVPG for young patients was 2-3 mmHg and the elderly sedentary patients had LVPD values just

above 1 mmHg [34]. Smiseth et al. conducted an invasive catheter study to calculate the LVPD driving early diastole. The mean LVPD for eight healthy adult males was 3.5 ± 0.3 mmHg [39].

Two and three dimensional pressure fields can be obtained using the magnetic resonance (MR) velocity and acceleration maps [40-42]. The pressure poisson equation, the divergence of the Navier-Stokes equation, is used to calculate relative pressure fields from MR velocity fields and is used because of possible noise associated with the velocity fields [40, 43, 44]. Ebbers et al. calculated the intraventricular pressure differences from a time-resolved three-dimensional vector field taken from a healthy female subject. The intraventricular pressure differences found are in agreement with animal studies [40], although inflow velocities and pressure differences seem to be much lower than similar echocardiography studies of healthy patients. Buyens et al. calculated LV intraventricular pressure differences from magnetic resonance acceleration fields of five healthy volunteers, showing good agreement with physiologically expected pressure differences. However, these studies are limited to healthy volunteers and do not investigate the intraventricular pressure differences in patients with LVDD [42]

2.1.3 Left Ventricular Simulations and Investigation Vortex Ring Formation In-vitro and In-vivo Studies

In addition to the clinical analysis of diastole, diastolic inflow has been studied both numerically and experimentally. A common difficulty in the numerical simulation of LV flows is the complex dynamics of the mitral valve; therefore numerical models often use a fixed open mitral valve [45]. The complexity of CFD left ventricular models has increased greatly from previous models which used ellipsoidal LV geometry [46] or modeled the LV base as a planar boundary with inlet and outlet orifices [47]. Saber et al. and Schenkel et al. have simulated patient specific LV geometries based on MRI data with fairly good agreement between simulated and MRI acquired flow fields [48, 49].

Left ventricular experimental simulators have also been studied with varying levels of complexity and physiological accuracy. Pierrakos et al. used a piston driven simulator with atrial and systemic pressures controlled hydrostatically to investigate the vortex dynamics downstream of mechanical and bioprosthetic heart valves using TRDPIV [50, 51]. Mouret et al. was the first to develop a dual activation left heart simulator which controls and activates both the left atrium and the left ventricle to simulate physiological velocity and pressure waveforms [52]. De Mey et al. studied the effects of LV properties including the relaxation time constant (τ), the LV compliance, and the LV filling pressures using a pneumatically actuated LV simulator. Similar to the previous simulators, the mock left ventricle is a compliant model which varies its geometry based on the surrounding pressures. But unlike the previous

models, the LV simulator used by De Mey does not function continuously, completing both systolic and diastolic motions, but is designed to complete a single diastolic motion before being reset [13].

2.1.4 Vortex Rings

The fluid dynamics associated with left ventricular filling are believed to be beneficial to the filling efficiency and an indication of overall cardiac function [53, 54]. The diastolic inflow jet through the mitral valve often produces a vortex ring from the inflow shear layer roll-up past the mitral annulus. It has been suggested that the presence of vortex rings during diastole provides a means for valve closure following early diastole [40, 55, 56]. Variations in size and propagation of the vortex ring at the base of the mitral annulus have been observed but have not been specifically linked to LV filling conditions or geometry.

Vortex rings have been studied extensively with a wide variety of investigation methods and applications, although the majority of vortex ring research involves laminar vortex rings [57-60]. The formation and propagation of vortex rings created using a piston cylinder arrangement has been studied while varying a variety of generator parameters including tube and orifice opening geometries and piston velocity programs [57, 59]. Two models are used to analyze the formation of laminar vortex rings. First is the slug flow model and second is the similarity model.

Gharib et al. investigated vortex ring formation using a piston cylinder arrangement. Their work demonstrated a non-dimensional time scale formation number which is the time at which the maximum circulation that a vortex ring can achieve is met and correspondingly the vortex ring pinch off. The formation number is defined in Equation 2.1,

$$T = \frac{\overline{U}_p t}{D}, \qquad 2.1$$

where $\bar{U}p$ is the running mean of the piston velocity, t is the duration of piston travel, and D is the orifice diameter [61]. Further research has also shown the importance of vortex formation in biological systems for the transport of fluid [62, 63].

A smaller number of studies have also been performed on turbulent vortex rings. There are two main types of turbulent vortex rings: high Reynolds number vortex rings which are initially turbulent and vortex rings which are initially laminar and transition to turbulence by azimuthal bending instabilities. Maxworthy studied the first type of turbulent vortex rings which had Reynolds numbers between 5000 and 15000 [64]. Glezer and Coles also studied a wide range of this type of turbulent vortex rings using laser-Doppler velocimetry and flow visualization techniques while specifically investigating the similarity

properties [65]. Weigand and Gharib studied vortex rings with initial Reynolds number of 7500 which underwent azimuthal bending instabilities and transitioned to turbulent vortex rings. The circulation and propagation velocity of the vortex rings were found to decrease in time corresponding with the shedding of vortical structures from the ring [66].

2.1.5 In-vivo Experiments

Gharib et al. investigated the dimensionless formation time associated with left ventricular diastolic filling using echocardiography and pulsed wave Doppler images. The formation time is calculated using the mean E-wave transmitral velocity obtained from pulse wave Doppler images, the duration of the E-wave filling and maximum diastolic mitral valve diameter. The formation time of 80 blindly tested patients was plotted against the patient's age showing a large percentage of the patients had a formation number within the optimal range of 3.5 to 5.5. A small population of patients suffering from DCM was included in the study with their formation time falling below the optimal range [54]. Unfortunately the main population of the study was blindly studied meaning that the cardiac health of the individuals was unknown. Additional diseased patient categories should be tested to confirm the hypothesis that diseased filling conditions modify the formation time value.

PCMRI allows for the 2D or 3D investigation of velocities within the heart which allows users to investigate velocity flow fields which were unavailable in the conventional Doppler Echocardiography[67]. Wong et al. examined the velocity fields within the right atrium, right ventricle and left atrium of a single young healthy male and tracked the occurrence of large-scale vortices within the chambers throughout systole and diastole [67]. Kerwin et al. published a conference proceeding which investigated the blood flow within the left ventricle during diastole and hypothesized that variability within the vorticity field of the LV may be an indicator of heart abnormality. Kerwin et al. reported that vortices were detected in all normal patients but not present in 2 of the 3 patients with congestive heart failure [68].

Other clinical imaging techniques have been used in tracking vortices within the LV both during systole and diastole. A study by Hong et al. utilized two dimensional contrast echocardiography which used a perfluoro-propane gas-filled, lipid-stabilized microbubble as the echo-enhancing agent to study normal filling and patients with systolic dysfunction. Vortices were identified and their location with respect to the long and short axes of the ventricle was recorded at each time instant of the 2D contrast echocardiogram. [69]

Overall, clinical studies of vortices within the LV indicate that the size and strength of the vortices within the LV are correlated with the left ventricular function. Studies have shown that the

anterior LV vortex is much stronger and more indicative of the patients LV function than the LV posterior vortex [53, 69].

2.1.6 In-vitro Experiments

Time-resolved digital particle velocimetry (TRDPIV) is a non-invasive visualization technique which images flow tracer particle movement within a plane at high-frequencies to capture spatio-temporal fluid dynamics. A region of interest is illuminated using a laser sheet and a series of consecutive images is acquired and the displacement of the particles between images is calculated using a correlation algorithm [70]. There is an extensive and progressing body of literature on DPIV processing algorithms and techniques which is driven by decreasing imaging limitations, increasing imaging magnification, decreasing measurement and calculation errors, and minimizing computational time [70-73]. Within this study, a robust phase correlation (RPC) DPIV processing algorithm will be used to analyze acquired data [74-76].

The formation of vortex rings within the left ventricle has also been studied in-vitro with several different techniques including left ventricular simulators and CFD studies. Shortland et al. studied vortex generation, area, and travel within 2 different valve less compliant ventricle geometries using flow visualization techniques. The effects of the ventricular size, filling curve, orifice diameter, and ventricular wall were studied with respect to vortex velocity with the orifice diameter showing the greatest dependence on vortex velocity [56]. Domenichini et al. compared the computational and experimental fluid dynamics of a healthy functioning LV with fixed open mitral and aortic valves. The numerical and PIV data showed the inflow mitral jet presented itself initially as two counter-rotating vortices where the posterior vortex approached the ventricular wall and the anterior vortex moved towards the apex [45]. Mouret et al. experimentally studied the flow past a monoleaflet prosthetic valve using PIV. In this study, in contrast to the previously presented experimental studies and the in-vivo studies, two co-rotating vortices were discovered where the posterior vortex grows and propagates towards the apex [77].

2.2 References

1. Khouri, S.J., G.T. Maly, D.D. Suh, and T.E. Walsh, *A practical approach to the echocardiographic evaluation of diastolic function.* Journal of the American Society of Echocardiography, 2004. **17**(3): p. 290-297.
2. Garcia, M.J., J.D. Thomas, and A.L. Klein, *New Doppler echocardiographic applications for the study of diastolic function.* Journal of the American College of Cardiology, 1998. **32**(4): p. 865-875.
3. Oh, J.K., *Echocardiography in heart failure: Beyond diagnosis.* European Journal of Echocardiography, 2007. **8**(1): p. 4-14.
4. Lew, W.Y.W., *Evaluation of Left-Ventricular Diastolic Function.* Circulation, 1989. **79**(6): p. 1393-1397.
5. Rovner, A., L. de las Fuentes, A.D. Waggoner, N. Memon, R. Chohan, and V.G. Davila-Roman, *Characterization of left ventricular diastolic function in hypertension by use of Doppler tissue imaging and color M-mode techniques.* Journal of the American Society of Echocardiography, 2006. **19**(7): p. 872-879.
6. Claessens, T.E., J. De Sutter, D. Vanhercke, P. Segers, and P.R. Verdonck, *New echocardiographic applications for assessing global left ventricular diastolic function.* Ultrasound in Medicine and Biology, 2007. **33**(6): p. 823-841.
7. Quinones, M.A., *Assessment of diastolic function.* Progress in Cardiovascular Diseases, 2005. **47**(5): p. 340-355.
8. Vandervoort, P.M., N.L. Greenberg, P.M. McCarthy, and J.D. Thomas. *Estimation of Left-Ventricular Filling Gradients Using Digital Analysis of Color Doppler M-Mode Velocities*. In *20th Annual Meeting of Computers in Cardiology*. 1993. London, England.
9. Brun, P., C. Tribouilloy, A.M. Duval, L. Iserin, A. Meguira, G. Pelle, and J.L. Duboisrande, *Left-Ventricular Flow Propagation During Early Filling is Related to Wall Relaxation - A Color M-Mode Doppler Analaysis.* Journal of the American College of Cardiology, 1992. **20**(2): p. 420-432.
10. Moller, J.E., E. Sondergaard, J.B. Seward, C.P. Appleton, and K. Egstrup, *Ratio of left ventricular peak E-wave velocity to flow propagation velocity assessed by color M-mode Doppler echocardiography in first myocardial infarction - Prognostic and clinical implications.* Journal of the American College of Cardiology, 2000. **35**(2): p. 363-370.
11. Takatsuji, H., T. Mikami, K. Urasawa, J.I. Teranishi, H. Onozuka, C. Takagi, Y. Makita, H. Matsuo, H. Kusuoka, and A. Kitabatake, *A new approach for evaluation of left ventricular diastolic function: Spatial and temporal analysis of left ventricular filling flow propagation by color M-mode Doppler echocardiography.* Journal of the American College of Cardiology, 1996. **27**(2): p. 365-371.
12. Yotti, R., J. Bermejo, J.C. Antoranz, M.M. Desco, C. Cortina, J.L. Rojo-Alvarez, C. Allue, L. Martin, M. Moreno, J.A. Serrano, R. Munoz, and M.A. Garcia-Fernandez, *A noninvasive method for assessing impaired diastolic suction in patients with dilated cardiomyopathy.* Circulation, 2005. **112**(19): p. 2921-2929.
13. De Mey, S., J. De Sutter, P. Vandervoort, M. De Buyzere, and P. Verdonck, *Assessment of LV Diastolic Filling Using Color M-Mode Doppler Echocardiography: Validation in a New Hydraulic Model*, in *Biomechan Model Mechanobiol*. 2004. p. 127-138.
14. Stugaard, M., N.L. Greenberg, J.H. Zhou, and J.D. Thomas. *Automated eigenvector analysis for quantification of color M-mode Doppler filling patterns of the left ventricle in an ischemic canine model*. In *24th Annual IEEE Computers in Cardiology Conference*. 1997. Lund, Sweden.
15. Parthenakis, F.I., A.P. Patrianakos, P.G. Tzerakis, D.M. Kambouraki, S.I. Chrysostomakis, and P.E. Vardas, *Late left ventricular diastolic flow propagation velocity determined by color M-mode Doppler in the assessment of diastolic dysfunction.* Journal of the American Society of Echocardiography, 2004. **17**(2): p. 139-145.

16. Thomas, J.D. and Z.B. Popovic, *Assessment of left ventricular function by cardiac ultrasound.* Journal of the American College of Cardiology, 2006. **48**(10): p. 2012-2025.
17. Chapman, J.N., J. Mayet, R.A. Foale, and S.A. Thom, *Intraventricular dispersion of E wave velocity: an alternative measure of left ventricular diastolic function in hypertensive patients?* Journal of Human Hypertension, 1999. **13**(12): p. 867-869.
18. Bella, J.N., V. Palmieri, M.J. Roman, J.E. Liu, T.K. Welty, E.T. Lee, R.R. Fabsitz, B.V. Howard, and R.B. Devereux, *Mitral ratio of peak early to late diastolic filling velocity as a predictor of mortality in middle-aged and elderly adults - The strong heart study.* Circulation, 2002. **105**(16): p. 1928-1933.
19. Galderisi, M., *Diastolic dysfunction and diastolic heart failure: diagnostic, prognostic and therapeutic aspects.* Cardiovascular Ultrasound 2005. **3**(9).
20. Hillis, G.S., J.E. Moller, P.A. Pellikka, B.J. Gersh, R.S. Wright, S.R. Ommen, G.S. Reeder, and J.K. Oh, *Noninvasive estimation of left ventricular filling pressure by E/e ' is a powerful predictor of survival after acute myocardial infarction.* Journal of the American College of Cardiology, 2004. **43**(3): p. 360-367.
21. Ommen, S.R., R.A. Nishimura, C.P. Appleton, F.A. Miller, J.K. Oh, M.M. Redfield, and A.J. Tajik, *Clinical utility of Doppler echocardiography and tissue Doppler imaging in the estimation of left ventricular filling pressures - A comparative simultaneous Doppler-Catheterization study.* Circulation, 2000. **102**(15): p. 1788-1794.
22. Nagueh, S.F., N.M. Lakkis, K.J. Middleton, W.H. Spencer, W.A. Zoghbi, and M.A. Quinones, *Doppler estimation of left ventricular filling pressures in patients with hypertrophic cardiomyopathy.* Circulation, 1999. **99**(2): p. 254-261.
23. Seo, Y., T. Ishimitsu, T. Ishizu, K. Obara, N. Moriyama, S. Kawano, S. Watanabe, and I. Yamaguchi, *Assessment of propagation velocity by contrast echocardiography for standardization of color Doppler propagation velocity measurements.* Journal of the American Society of Echocardiography, 2004. **17**(12): p. 1266-1274.
24. Nagueh, S.F., C.P. Appleton, T.C. Gillebert, P.N. Marino, J.K. Oh, O.A. Smiseth, A.D. Waggoner, F.A. Flachskampf, P.A. Pellikka, A. Evangelisa, and E. Amer Soc, *Recommendations for the Evaluation of Left Ventricular Diastolic Function by Echocardiography.* European Journal of Echocardiography, 2009. **10**(2): p. 165-193.
25. Sessoms, M.W., J. Lisauskas, and S.J. Kovacs, *The left ventricular color M-mode Doppler flow propagation velocity V-p: In vivo comparison of alternative methods including physiologic implications.* Journal of the American Society of Echocardiography, 2002. **15**(4): p. 339-348.
26. Asada-Kamiguchi, J., M. Jones, N.L. Greenberg, Z.B. Popovic, H. Tsujino, A.D. Zetts, J.X. Qin, M.J. Garcia, J.D. Thomas, and T. Shiota, *Intraventricular pressure gradients in left ventricular aneurysms determined by color M-mode Doppler method: An animal study.* Journal of the American Society of Echocardiography, 2006. **19**(9): p. 1112-1118.
27. Dorosz, J.L., K.G. Lehmann, and J.R. Stratton, *Comparison of tissue Doppler and propagation velocity to invasive measures for measuring left ventricular filling pressures.* American Journal of Cardiology, 2005. **95**(8): p. 1017-1020.
28. Chaliki, H.P., D.G. Hurrell, R.A. Nishimura, R.A. Reinke, and C.P. Appleton, *Pulmonary venous pressure: Relationship to pulmonary artery, pulmonary wedge, and left atrial pressure in normal, lightly sedated dogs.* Catheterization and Cardiovascular Interventions, 2002. **56**(3): p. 432-438.
29. Dokainish, H., W.A. Zoghbi, N.M. Lakkis, F. Al-Bakshy, M. Dhir, M.A. Quinones, and S.F. Nagueh, *Optimal noninvasive assessment of left ventricular filling pressures - A comparison of tissue Doppler echocardiography and B-type natriuretic peptide in patients with pulmonary artery catheters.* Circulation, 2004. **109**(20): p. 2432-2439.
30. Little, W.C. and J.K. Oh, *Echocardiographic Evaluation of Diastolic Function Can Be Used to Guide Clinical Care.* Circulation, 2009. **120**(9): p. 802-809.
31. Little, W.C., *Diastolic dysfunction beyond distensibility - Adverse effects of ventricular dilatation.* Circulation, 2005. **112**(19): p. 2888-2890.

32. Greenberg, N.L., P.M. Vandervoort, M.S. Firstenberg, M.J. Garcia, and J.D. Thomas, *Estimation of diastolic intraventricular pressure gradients by Doppler M-mode echocardiography.* American Journal of Physiology-Heart and Circulatory Physiology, 2001. **280**(6): p. H2507-H2515.
33. Rovner, A., N.L. Greenberg, J.D. Thomas, and M.J. Garcia, *Relationship of diastolic intraventricular pressure gradients and aerobic capacity in patients with diastolic heart failure.* American Journal of Physiology-Heart and Circulatory Physiology, 2005. **289**(5): p. H2081-H2088.
34. Popovic, Z.B., A. Prasad, M.J. Garcia, A. Arbab-Zadeh, A. Borowski, E. Dijk, N.L. Greenberg, B.D. Levine, and J.D. Thomas, *Relationship among diastolic intraventricular pressure gradients, relaxation, and preload: impact of age and fitness.* American Journal of Physiology-Heart and Circulatory Physiology, 2006. **290**(4): p. H1454-H1459.
35. Thomas, J.D. and Z.B. Popovic, *Intraventricular pressure differences - A new window into cardiac function.* Circulation, 2005. **112**(12): p. 1684-1686.
36. Greenberg, N.L., S. Krucinski, J.D. Thomas, and I. Ieee. *Significance of color Doppler M-mode scanline orientation in the non-invasive assessment of intraventricular pressure gradients*. In *24th Annual Computers in Cardiology Conference*. 1997. Lund, Sweden.
37. Greenberg, N.L., P.L. Castro, J. Drinko, M.J. Garcia, and J.D. Thomas. *Effect of scanline orientation on ventricular flow propagation: Assessment using high frame-rate color Doppler Echocardiography*. In *37th Annual Rocky Mountain Bioengineering Symposium/37th International ISA Biomedical Sciences Instrumentation Symposium*. 2000. Colorado Springs, Co.
38. De Boeck, B.W.L., J.K. Oh, P.M. Vandervoort, J.A. Vierendeels, R. van der Aa, and M.J.M. Cramer, *Colour M-mode velocity propagation: a glance at intra-ventricular pressure gradients and early diastolic ventricular performance.* European Journal of Heart Failure, 2005. **7**(1): p. 19-28.
39. Smiseth, O.A., K. Steine, G. Sandbaek, M. Stugaard, and T.O. Gjolberg, *Mechanics of intraventricular filling: study of LV early diastolic pressure gradients and flow velocities.* American Journal of Physiology-Heart and Circulatory Physiology, 1998. **44**(3): p. H1062-H1069.
40. Ebbers, T., L. Wigstrom, A.F. Bolger, B. Wranne, and M. Karlsson, *Noninvasive measurement of time-varying three-dimensional relative pressure fields within the human heart.* Journal of Biomechanical Engineering-Transactions of the Asme, 2002. **124**(3): p. 288-293.
41. Yang, G.Z., P.J. Kilner, N.B. Wood, S.R. Underwood, and D.N. Firmin, *Computation of flow pressure fields from magnetic resonance velocity mapping.* Magnetic Resonance in Medicine, 1996. **36**(4): p. 520-526.
42. Buyens, F., O. Jolivet, A. De Cesare, J. Bittoun, A. Herment, J.P. Tasu, and E. Mousseaux, *Calculation of left ventricle relative pressure distribution in MRI using acceleration data.* Magnetic Resonance in Medicine, 2005. **53**(4): p. 877-884.
43. Long, Q., R. Merrifield, X.Y. Xu, P. Kilner, D.N. Firmin, and G.Z. Yang, *Subject-specific computational simulation of left ventricular flow based on magnetic resonance imaging.* Proceedings of the Institution of Mechanical Engineers Part H-Journal of Engineering in Medicine, 2008. **222**(H4): p. 475-485.
44. Charonko, J.J., P.P. Vlachos, and Asme. *Keynote paper: Time-accurate measurement of pressure from particle image velocimetry data*. In *5th Joint ASME/JSME Fluids Engineering Summer Conference*. 2007. San Diego, CA.
45. Domenichini, F., G. Querzoli, A. Cenedese, and G. Pedrizzetti, *Combined experimental and numerical analysis of the flow structure into the left ventricle.* Journal of Biomechanics, 2007. **40**(9): p. 1988-1994.
46. Cheng, Y., H. Oertel, and T. Schenkel, *Fluid-structure coupled CFD simulation of the left ventricular flow during filling phase.* Annals of Biomedical Engineering, 2005. **33**(5): p. 567-576.

47. Saber, N., A. Gosman, N. Wood, P. Kilner, C. Charrier, and D. Firmin, *Computational flow modeling of the left ventricle based on in vivo MRI data: initial experience.* Annals of Biomedical Engineering, 2001. **29**(4): p. 275-283.
48. Saber, N., N. Wood, A. Gosman, R. Merrifield, G. Yang, C. Charrier, P. Gatehouse, and D. Firmin, *Progress towards patient-specific computational flow modeling of the left heart via combination of magnetic resonance imaging with computational fluid dynamics.* Annals of Biomedical Engineering, 2003. **31**(1): p. 42-52.
49. Schenkel, T., M. Malve, M. Reik, M. Markl, B. Jung, and H. Oertel, *MRI-Based CFD Analysis of Flow in a Human Left Ventricle: Methodology and Application to a Healthy Heart.* Annals of Biomedical Engineering, 2009. **37**(3): p. 503-515.
50. Pierrakos, O. and P.P. Vlachos, *The effect of vortex formation on left ventricular filling and mitral valve efficiency.* Journal of Biomechanical Engineering-Transactions of the Asme, 2006. **128**(4): p. 527-539.
51. Pierrakos, O., P.P. Vlachos, and D.P. Telionis, *Time-resolved DPIV analysis of vortex dynamics in a left ventricular model through bileaflet mechanical and porcine heart valve prostheses.* Journal of Biomechanical Engineering-Transactions of the Asme, 2004. **126**(6): p. 714-726.
52. Mouret, F., V. Garitey, T. Gandelheid, J. Fuseri, and R. Rieu, *A new dual activation simulator of the left heart that reproduces physiological and pathological conditions.* Medical & Biological Engineering & Computing, 2000. **38**(5): p. 558-561.
53. Kilner, P.J., G.Z. Yang, A.J. Wilkes, R.H. Mohiaddin, D.N. Firmin, and M.H. Yacoub, *Asymmetric redirection of flow through the heart.* Nature, 2000. **404**(6779): p. 759-761.
54. Gharib, M., E. Rambod, A. Kheradvar, D.J. Sahn, and J.O. Dabiri, *Optimal vortex formation as an index of cardiac health.* Proceedings of the National Academy of Sciences of the United States of America, 2006. **103**(16): p. 6305-6308.
55. Bellhouse, B.J., *Fluid Mechanics of a Model Mitral Valve and Left Ventricle.* Cardiovascular Research, 1972. **6**: p. 199-210.
56. Shortland, A.P., R.A. Black, J.C. Jarvis, F.S. Henry, F. Iudicello, M.W. Collins, and S. Salmons, *Formation and travel of vortices in model ventricles: Application to the design of skeletal muscle ventricles.* Journal of Biomechanics, 1996. **29**(4): p. 503-511.
57. Krueger, P., *Circulation and trajectories of vortex rings formed from tube and orifice openings.* Physica D: Nonlinear Phenomena, 2008. **237**(14-17): p. 2218-2222.
58. Weigand, A. and M. Gharib, *On the evolution of laminar vortex rings.* Experiments in Fluids, 1997. **22**(6): p. 447-457.
59. Pullin, D., *Vortex ring formation at tube and orifice openings.* Physics of Fluids, 1979. **22**: p. 401.
60. Didden, N., *On the formation of vortex rings: rolling-up and production of circulation.* Zeitschrift für Angewandte Mathematik und Physik (ZAMP), 1979. **30**(1): p. 101-116.
61. Gharib, M., E. Rambod, and K. Shariff, *A universal time scale for vortex ring formation.* Journal of Fluid Mechanics, 1998. **360**: p. 121-140.
62. Dabiri, J.O., *Optimal Vortex Formation as a Unifying Principle in Biological Propulsion.* Annual Review of Fluid Mechanics, 2009. **41**: p. 17-33.
63. Dabiri, J.O. and M. Gharib, *The role of optimal vortex formation in biological fluid transport.* Proceedings of the Royal Society B-Biological Sciences, 2005. **272**(1572): p. 1557-1560.
64. Maxworthy, T., *Turbulent vortex rings.* Journal of Fluid Mechanics, 1974. **64**(02): p. 227-240.
65. Glezer, A. and D. Coles, *An experimental study of a turbulent vortex ring.* Journal of Fluid Mechanics, 1990. **211**: p. 243-283.
66. Weigand, A. and M. Gharib, *On the decay of a turbulent vortex ring.* Physics of Fluids, 1994. **6**: p. 3806.
67. Wong, K.K.L., R.M. Kelso, S.G. Worthley, P. Sanders, J. Mazumdar, and D. Abbott, *Cardiac Flow Analysis Applied to Phase Contrast Magnetic Resonance Imaging of the Heart.* Annals of Biomedical Engineering, 2009. **37**(8): p. 1495-1515.

68. Kerwin, W., J. Hertzberg, J. Cooke, H. Chluda, R. Shandas, and E. Gill. *Vorticity imaging of diastolic cardiac inflow by phase-contrast MRI*. In *2nd IEEE International Symposium on Biomedical Imaging*. 2004. Arlington, VA: Ieee.
69. Hong, G.-R., G. Pedrizzetti, G. Tonti, P. Li, Z. Wei, J.K. Kim, A. Baweja, S. Liu, N. Chung, H. Houle, J. Narula, and M.A. Vannan, *Characterization and Quantification of Vortes Flow in the Human Left Ventricle by Contrast Echocardiography Using Vector Particle Image Velocimetry.* JACC: Cardiovascular Imaging, 2008. **1**(6): p. 705-717.
70. Grant, I., *Particle image velocimetry: a review.* Proceedings of the Institution of Mechanical Engineers, Part C: Journal of Mechanical Engineering Science, 1997. **211**(1): p. 55-76.
71. McKenna, S. and W. McGillis, *Performance of digital image velocimetry processing techniques.* Experiments in Fluids, 2002. **32**(1): p. 106-115.
72. Huang, H., D. Dabiri, and M. Gharib, *On errors of digital particle image velocimetry.* Measurement Science and Technology, 1997. **8**: p. 1427-1440.
73. Adrian, R., *Twenty years of particle image velocimetry.* Experiments in Fluids, 2005. **39**(2): p. 159-169.
74. Eckstein, A. and P. Vlachos, *Assessment of advanced windowing techniques for DPIV*. Measurement Science and Technology, 2009. **20**: p. 075402.
75. Eckstein, A. and P.P. Vlachos, *Digital particle image velocimetry (DPIV) robust phase correlation.* Measurement Science and Technology, 2009. **20**: p. 055401.
76. Eckstein, A.C., J. Charonko, and P. Vlachos, *Phase correlation processing for DPIV measurements.* Experiments in Fluids, 2008. **45**(3): p. 485-500.
77. Mouret, F., L. Kadem, E. Bertrand, J. Dumesnil, P. Pibarot, and R. Rieu, *Mitral prosthesis opening and flow dynamics in a model of left ventricle: an in vitro study on a monoleaflet mechanical valve.* Cardiovascular Engineering, 2005. **5**(1): p. 13-20.

3 Vortex Ring Breakdown in Wall-Bounded Domains

Kelley C. Stewart and Pavlos P. Vlachos
Department of Mechanical Engineering, Virginia Tech, Blacksburg, VA 24061, USA

3.1 Abstract

The dynamics of vortex rings generated in semi-infinite domains has been extensively studied. However, vortex ring dynamics within radial confinements has received very little attention to date despite its relevance to important processes; for example in cardiovascular flows. This study addresses this limitation and studies vortex dynamics in radially confined domains to analyze the effect of vortex-ring wall interaction. Radially confined vortex rings were studied using Time Resolved Digital Particle Image Velocimetry. We found that the vortex ring formation process was unaffected by the introduction of the confinement domain. However, the vortex rings with increased confinement displayed an onset of enhanced circulation decay after the time of vortex ring formation. The circulation decay rate after pinch-off remained constant for all vortex rings generated within a single severe confinement with varying generation conditions, implying the decay rate is dependent on the ratio of piston cylinder to confinement diameters.

3.2 Introduction

Vortex rings have been extensively studied with a wide variety of investigation methods and applications, with the majority of vortex ring research involving laminar vortex rings generated within semi-infinite volumes [1-4]. Gharib et al.[5] investigated vortex ring formation using a piston cylinder arrangement and showed that the formation number with the nondimensional time shown in equation 3.1, where $\bar{U}p$ is the running mean of the piston velocity, t is the duration of piston travel and D_0 is the orifice diameter,

$$\frac{L}{D_0} = \frac{\overline{U}_p t}{D_0} \tag{3.1}$$

This relationship is equivalent to the length of piston travel normalized by the piston cylinder diameter (L/D_0). Furthermore the effect of variations in generator parameters including tube and orifice opening geometries and piston velocity programs, for other studies using piston cylinder arrangements, on the formation and propagation of vortex rings has also been studied [1, 3].

In addition, vortex ring interactions with solid bodies have been previously studied both numerically and experimentally [6]. One of the most commonly studied vortex ring interactions involves a vortex ring impacting a wall normal to its direction of propagation [7-10]. Such studies describe the formation of secondary and tertiary vortical structures at the wall using flow visualization and numerical studies. Lim [11] expanded on these studies and investigated the interaction of a vortex ring with an inclined wall, in which he describes the deformation and stretching of the vortex ring as it approaches the wall and the following helical vortex lines as the vortex ring unevenly impinges on the wall. He identified an asymmetric rebound phenomenon and formation of a secondary vortical structure. Walker [12] first studied the numerical problem of a rectilinear vortex near an infinite plane wall where he assumed two counter rotating vortices were translating in an unbounded incompressible fluid and at time t=0 an infinite plate was placed between them causing the vortex below the plate to be interpreted as an image vortex. The study investigated the thin unsteady boundary layer, which developed on the plate. Separation in the boundary layer was found to occur shortly after the plate was inserted and was defined as corresponding to the first closed recirculating eddy in the boundary layer. Most closely related to the current work, Chang et al. [13] studied numerically and with flow visualization an elliptical vortex ring between two no-slip parallel walls, where counter rotating secondary vortical structures were formed at the wall. Vortices within confined domains have been used to study swirling flows most commonly in association with axial-flow turbomachinery applications [14, 15]. Fundamental vortex ring wall interactions have been explored and these studies are critical to understanding vortex ring interactions with more complex boundaries such as radially confined domains which are less understood.

The current study investigates vortex ring dynamics generated within radially confined domains and compares these with vortex rings created in semi-infinite domains. The vortex ring circulation strength is examined using time resolved digital planar particle image velocimetry (TRDPIV) to determine the effects of confinement. The vortex ring wall interactions are investigated to determine the method of vortex ring breakdown over a wide range of Reynolds numbers generated in confined domains.

3.3 Methods

3.3.1 Experimental Setup and Vortex Ring Generation Conditions

Vortex rings were generated by a discharge of fluid from a piston cylinder arrangement over a finite time interval. For each trial the piston cylinder's target travel distance was determined based on the chosen piston stroke to diameter ratio (L/D_0) which varied between 1 and 7. This process can be estimated by considering the slug-flow model where we assume uniform flow over the circular outlet jet and we neglect the initial transient period [1, 4, 16].

A pneumatic cylinder was used in combination with a Teflon piston cap to produce the vortex rings. The piston moved inside a 0.0127 meter inner diameter (D_0) cylinder and the region of interest began immediately downstream of the small piston cylinder's end. Radial confinement domains were created using optically clear acrylic tubing concentrically positioned around the piston cylinder as shown Figure 3.1. The velocity of the piston cylinder varied in time associated with a specific velocity program and was measured using a Novotechnik linear TLH series potentiometer (<0.01mm resolution). Mean velocity with respect to time was calculated using equation 3.2, where $u_p(t)$ is the velocity of the piston cylinder at time t, which is assumed to be constant over the jet area, and T is the total ejection time interval,

$$\overline{U}_p = \frac{1}{T}\int_0^T u_p(t)dt. \tag{3.2}$$

Under experimental conditions there exist variations within the orifice exit velocity with respect to time which strays from the slug flow model. The variations within the velocity of the orifice exit can be accounted for by a velocity program factor, P calculated in equation 3.3, as introduced by Glezer [17],

$$P = \int_0^1 \left(\frac{U_p^2}{\overline{U}_p^2}\right) d\left(\frac{t}{T}\right) = \frac{\overline{U_p^2}}{\overline{U}_p^2}. \tag{3.3}$$

Program factors for a square wave, ramp wave, and haversine wave were calculated by Diddens as 1, 4/3, and 3/2 respectively [17]. The velocity program factor accounts for increases in vortex ring circulation and momentum associated with variations in the velocity program [17].

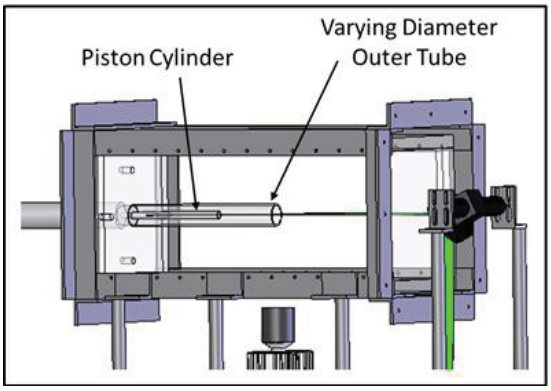

Figure 3.1: Schematic of vortex ring formation experimental setup with varying downstream diameter conditions.

3.3.2 Experimental Testing Conditions

The experimental testing conditions, L/D_0 values, were chosen to produce a range of Reynolds numbers (Γ_{slug}/ν) where circulation, Γ_{slug} is calculated using equation 3.4,

$$\Gamma_{slug} = \frac{1}{2} t \overline{U}_p^2. \qquad 3.4$$

Table 3.1 displays the experimental test matrix. Three downstream confinement conditions were studied which include semi-infinite conditions with no downstream radial confinement and two confined downstream conditions with D/D_0 values of 2 and 3.

Table 3.1: Experimental Test Matrix

Confinement Parameters			Re	L/D_0
Semi-infinite	D/D_0=2	D/D_0=3	~1,400	1
Semi-infinite	D/D_0=2	D/D_0=3	~2,600	1.5
Semi-infinite	D/D_0=2	D/D_0=3	~3,500	2
Semi-infinite	D/D_0=2	D/D_0=3	~5,500	2.5
Semi-infinite	D/D_0=2	D/D_0=3	~7,000	3
Semi-infinite	D/D_0=2	D/D_0=3	~13,000	4
Semi-infinite	D/D_0=2	D/D_0=3	~18,000	5.5
Semi-infinite	D/D_0=2	D/D_0=3	~27,000	7

3.3.3 TRDPIV Experimental Procedures

Planar TRDPIV is an optical flow measurement technique which typically uses a coherent light source to illuminate a region of interest. The coherent light source is expanded into a thin plane and directed over a region of interest parallel to a high-speed camera lens face. The flow is seeded with neutrally-buoyant flow tracer particles; the movement of these flow tracer particles is captured by high speed images. Cross correlation techniques are used to obtain planes of velocity vectors within the region of interest from the flow tracer displacements between images.

The laser plane was positioned parallel to and slicing through the center of the piston cylinder, as shown in Figure 3.1, and the high speed camera was positioned below the test setup perpendicular to the laser plane. All data was acquired using a kHz Nd:YAG dual head New Wave Pegasus laser. Laser pulses separated by 0.02 – 0.003 seconds depending on L/D_0, and were synchronized with an IDT XS-5 CMOS camera firing at 500 pairs per second. The images acquired were 1280 by 800 pixels, and the magnification was set at 62 microns per pixel. Approximately neutrally-buoyant polystyrene spheres with a mean diameter of 10 μm were used as flow tracers.

Cross correlation algorithms were used to calculate the velocity fields on a uniform grid of 199x319 locations with a vector grid spacing of 4 pixels or 248μm. Three passes of a robust phase correlation based deformation method algorithm were used with a grid resolution of 16x16 vectors and a window resolution of 32x32 vectors on the first two passes [18-21]. The final pass had a grid resolution of 4x4 and a window resolution of 16x16 vectors. Area validation using median filters on grids of 7x7 vectors was implemented in order to remove stray vectors [22]. Based on the magnification and the laser timing, a typical displacement of the flow tracers between correlated frames was on the order of 3-6 pixels. The mean error of this correlation technique was estimated between 0.05-0.15 pixels [18].

3.3.4 Proper Orthogonal Decomposition

Proper Orthogonal Decomposition is a technique for decomposing a flow field into its fundamental components. The method calculates the optimal basis functions for data reduction and determines the energy contained in each of these modes [23, 24]. POD was used to post process the TRDPIV results in order to remove high frequency noise, in essence producing a low order model of the flow. In this analysis the flow fields were reconstructed with the fundamental eigenmodes which contained 95% of the total energy in the system.

3.3.5 Generated Vortex Rings

Vortex rings were generated at eight Reynolds numbers into a semi-infinite downstream volume. The piston velocity factor calculated using equation 3.3 varied from 1.10 to 1.39, corresponding to Glezer's value for a ramp velocity program of 4/3, which is most similar to this study's velocity program. The calculated velocity program is used as a modified Reynolds number shown in equation 3.5 as defined by Glezer [17],

$$\mathrm{Re}_J = \frac{P\bar{U}_p L_0}{\nu} \qquad 3.5$$

The modified Reynolds number parameter, Re_J, accounts for the piston velocity profile and provides a non-dimensional parameter for characterizing vortex ring circulation strength.

3.3.6 Vortex Identification Scheme

A local vortex identification scheme was used to determine the location of vortex rings using the λ_{ci} criterion where the vortex core is defined using the imaginary part of the complex eigenvalue of the velocity gradient tensor, as described by Zhou and Chakraborty et al. [25, 26]. Using this method, vortex centers were located. A Compact-Richardson finite difference scheme was used to calculate vorticity fields, providing low noise amplification and bias error [27]. The circulation strength of each vortex was calculated by integrating the vorticity (ω) over the area determined by a constant λ_{ci} value of λ_{ci}^2=7% of the maximum value,

$$\Gamma = \int_A \omega \cdot n dS. \qquad 3.6$$

3.3.7 Determining the Vortex Ring Formation Time

The vortex ring formation time is the time at which the maximum vortex ring circulation occurs and the vortex ring pinches off. This time was statistically calculated using the change point method where the cumulative-sum of the rate of change of the vortex ring circulation vs. nondimensional time, $\bar{U}_p t/D_0$ is maximum. The time of the peak cumulative sum is the time of the most statistically significant change within the circulation contour, and was designated to be the formation time.

3.4 Results

In this study the behavior of the unconfined vortex rings was consistent with previously studied vortex rings produced by a piston cylinder arrangement [5]. Vortex rings generated within the confined domains were compared to the conventional vortex rings in semi-infinite domains to explore the variations caused by the confinement. Figure 3.2A displays the circulation normalized by peak circulation, Γ_0, versus the nondimensional timescale, $T=\bar{U}_p t/D_0$, for the unconfined and D/D_0=2 cases with L/D_0=3. The two contours follow the same trend of circulation increase until the maximum circulation value is attained at $T\approx$3.5. After this point, the circulation values remain similar until $T\approx$6.5 when the confined circulation begins to rapidly decay. Figure 3.2 a-c and d-f display the vorticity fields for the unconfined and confined vortex rings, where $W^*=\omega D_0/U_{max\ piston}$. In the confined case, vorticity is generated along the length of the cylinder surface due to the tangential pressure gradient at the wall during the piston motion. Once the vortex ring was formed, opposite sign vorticity is generated at the wall region adjacent to the vortex core where the fluid is moving in the negative X/D_0 direction (back

toward the orifice). This induced vorticity layer separates from the wall and a secondary vortical structure is formed trailing the primary vortex core. In Figure 3.2 frames e and f, secondary vortical structures are visible in the confined case behind the primary vortex core leading to the breakdown of the translating vortex ring that are not present in the unconfined case.

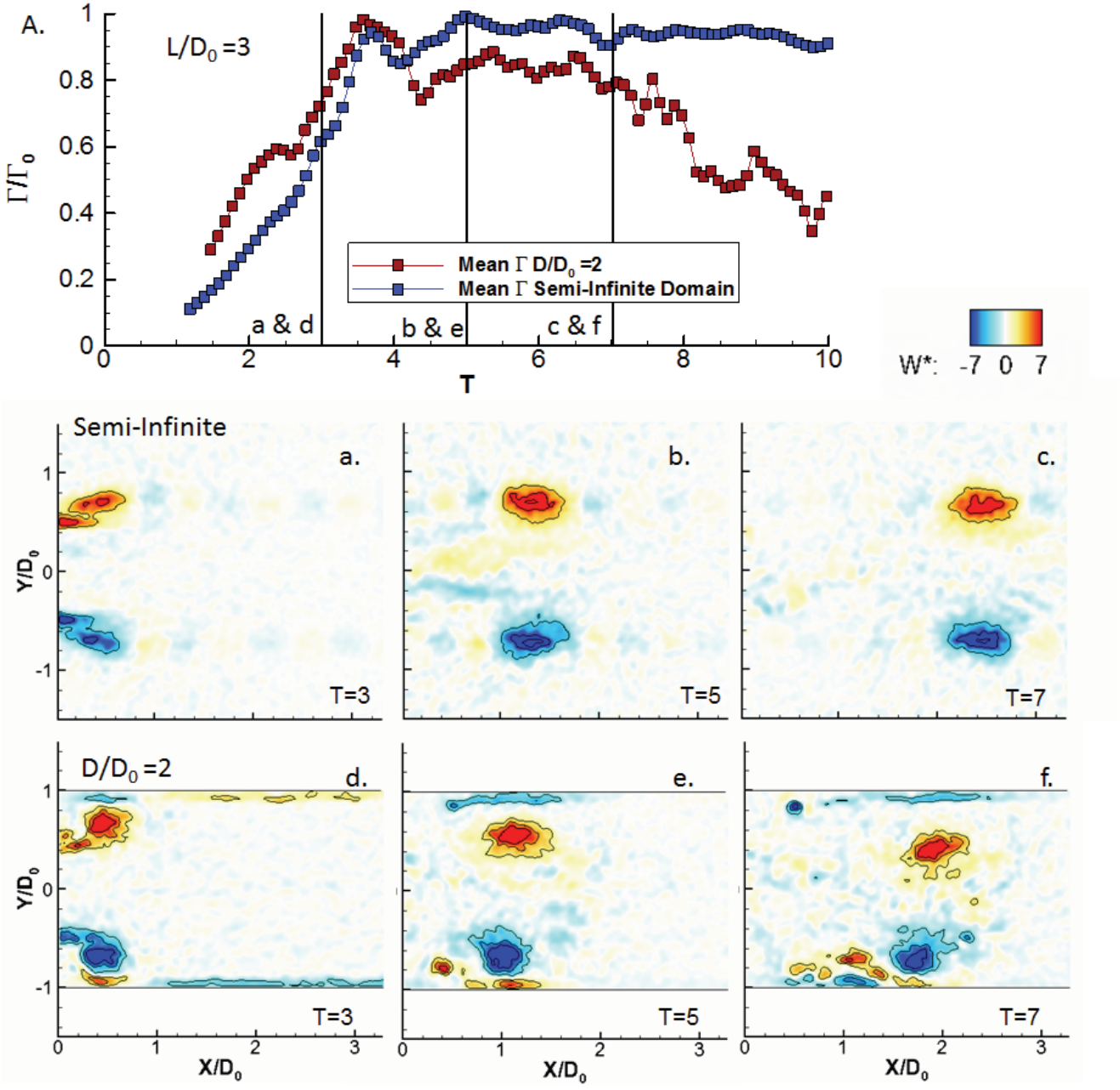

Figure 3.2: Comparison of L/D_0=3 semi-infinite and D/D_0=2 cases. A. Plot of normalized circulation versus nondimensional time T. a.-c. Vorticity field for unconfined vortex ring. d.-f. Vorticity fields for D/D_0=2 confinement case.

The formation phase of the vortex rings was further investigated with respect to the confinement domain. Figure 3.3 displays the peak circulation divided by the kinematic viscosity (Γ_{peak}/ν) versus the Re_J parameter. The solid line represents the best fit trend line from Glezer's analysis [17] of Didden's data where the data collapsed onto a single trend line when plotted versus the modified Reynolds number (Re_J) calculated in equation 3.5. The data analyzed by Glezer, to which the trend line was fit, only included L/D_0 values of 0.6-2.2. In our data, the Γ_{peak}/ν versus Re_J relationship as well as the peak circulation strength values is not affected by the confinement, as shown in Figure 3.3. The data points for L/D_0 values of 3 and below, left most four data points for each confinement case, approximately follow Glezer's previously reported data trend line. The higher L/D_0 values deviate from the linear trend of the lower laminar L/D_0 values.

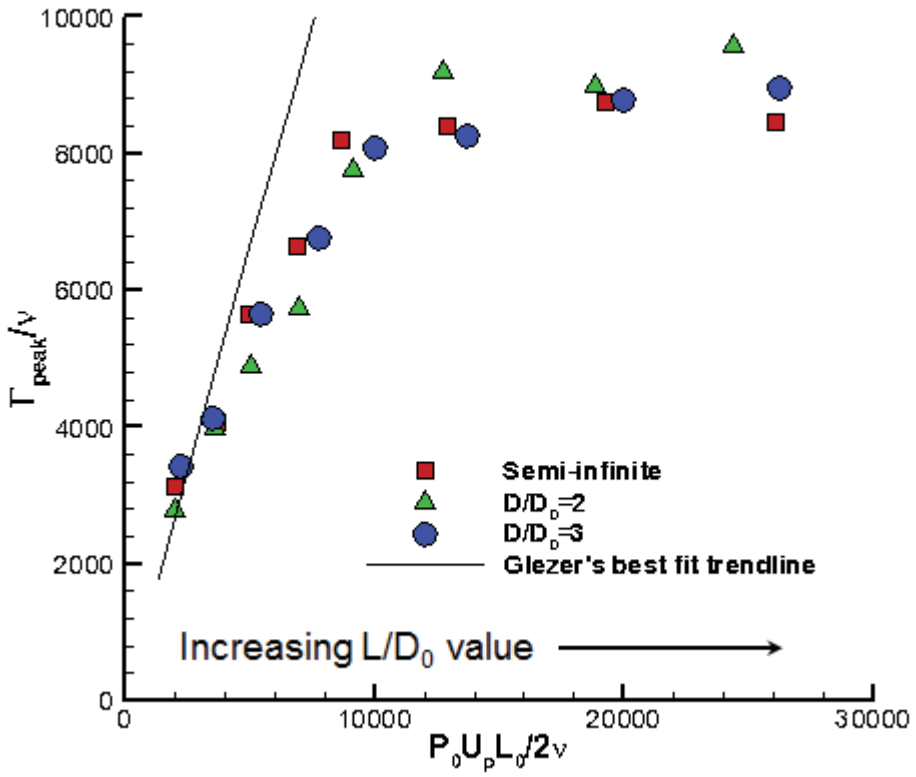

Figure 3.3: Circulation of generated vortex rings with varying downstream domain conditions

Vortex rings generated with an L/D_0>4 were expected to have a decreased circulation from the estimated slug flow circulation, calculated in equation 3.6, since the maximum attainable circulation is achieved and the remaining vorticity is shed into the trailing jet. Similarly, the vortex ring pinch-off time increases

linearly until L/D_0 values of 4 and remains constant at higher L/D_0 values, shown in Figure 3.4. The nondimensional pinch-off time and generating L/D_0 parameter follow approximately a forty-five degree line for L/D_0 cases <4. The L/D_0 cases 4 and above plateau at approximately T=4 with the D/D_0 =2 confined case falling slightly above 4.

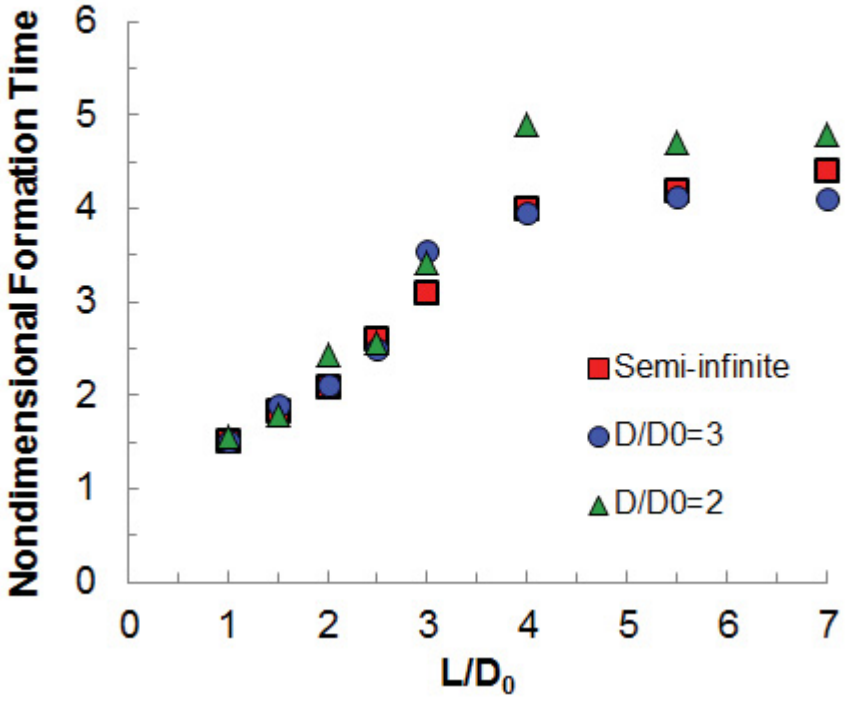

Figure 3.4: Nondimensional time of vortex ring pinch-off versus L/D_0 generation case

Although the initial vortex ring formation was relatively uninfluenced by the addition of confined downstream boundaries, the time varying circulation strength was greatly altered. The circulation strengths for each vortex ring case, are plotted versus T in Figure 3.5A and B with no outer confinement and D/D_0=2 respectively. In Figure 3.5A, the circulation strengths of the unconfined vortex rings grow as T increases until a maximum was reached at the formation time, at which point the circulation plateaus. The vortex ring formation time corresponds to the L/D_0 generating conditions of the vortex ring up until a value of 4, as shown in Figure 3.4.

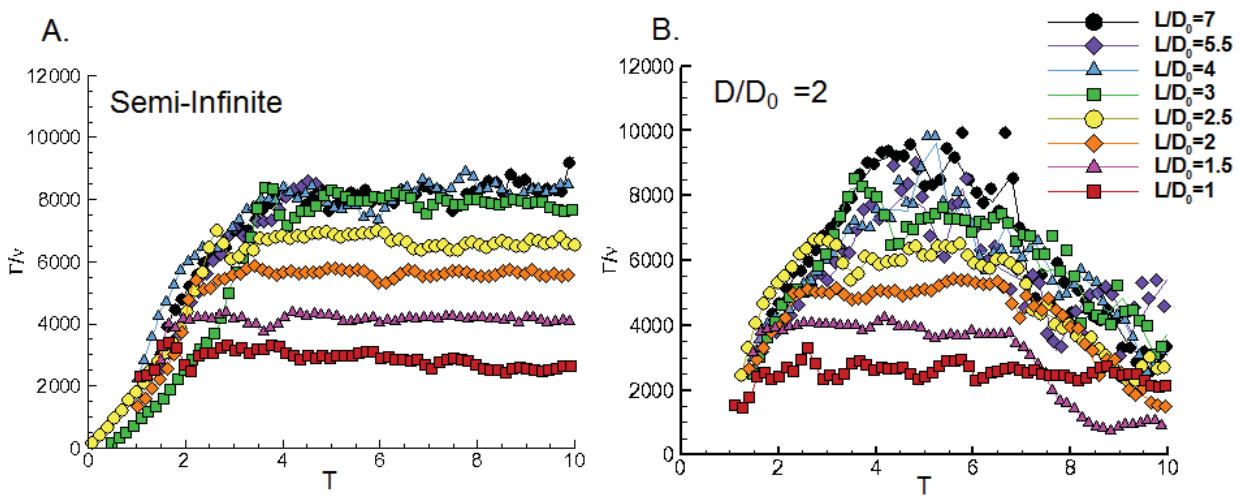

Figure 3.5: Circulation strength versus formation time for vortex rings generated with A.) semi-infinite domain and B.) D/D_0=2 confinement.

Figure 3.5B displays the normalized circulation strength versus formation time for the D/D_0=2 confinement cases. The circulation strength contours for each L/D_0 case show a drastically different pattern than the unconfined cases. The D/D_0=3 confinement domain did not display substantially different circulation versus T contours from the unconfined vortex ring domain values, therefore is not shown. For the D/D_0=2 case, the initial formation and growth region remains relatively unaltered. However after the peak circulation strength is achieved, the Γ/ν values begin to decline at a similar decay rate for all L/D_0 cases >1. This time of the onset of decay varies with L/D_0. Increasing L/D_0 values result in both elevated vortex circulation as well as slightly increased vortex ring diameter which may make the onset of circulation decay occur earlier. Equation 3.7 displays the normalized diameter of the vortex ring generated by a tube with $1500 \leq Re \leq 4500$ estimated by Auerbach based on the piston travel (L), a similar equation is available for $L/D_0<1$ [28],

$$D_{VR} / D_0 = 1.18(L / D_0)^{1/5} \text{ for } 1 \leq L/D_0 \leq 3.3. \qquad 3.7$$

From this equation, we can see that the vortex ring diameter normalized by the piston cylinder diameter slightly grows with increasing L/D_0 value. Figure 3.6 displays the L/D_0 case versus the D_{VR}/D_0 values for the unconfined, D/D_0=3 and D/D_0=2 cases. Additionally, the estimated unconfined vortex ring diameters, calculated using equation 3.7, are plotted as a black line, although this relationship is only valid through a L/D_0 of 3.3. The unconfined experimental vortex ring diameters closely follow the estimated vortex ring diameters and continue to increase similar to an extrapolation of the line by Auerbach. An exponential

curve was fit to the diameters of each of the confinement cases as shown in Figure 3.6. For each L/D_0 case the vortex ring diameter decreases with increasing confinement. Additionally, the unconfined and D/D_0=3 cases display similar rates of diameter increase with L/D_0 case, however the D/D_0=2 case has a much smaller rate of diameter increase the vortex ring diameters appear to remain constant at approximately D_{VR}/D_0=1.4 for L/D_0 cases of 4 and above.

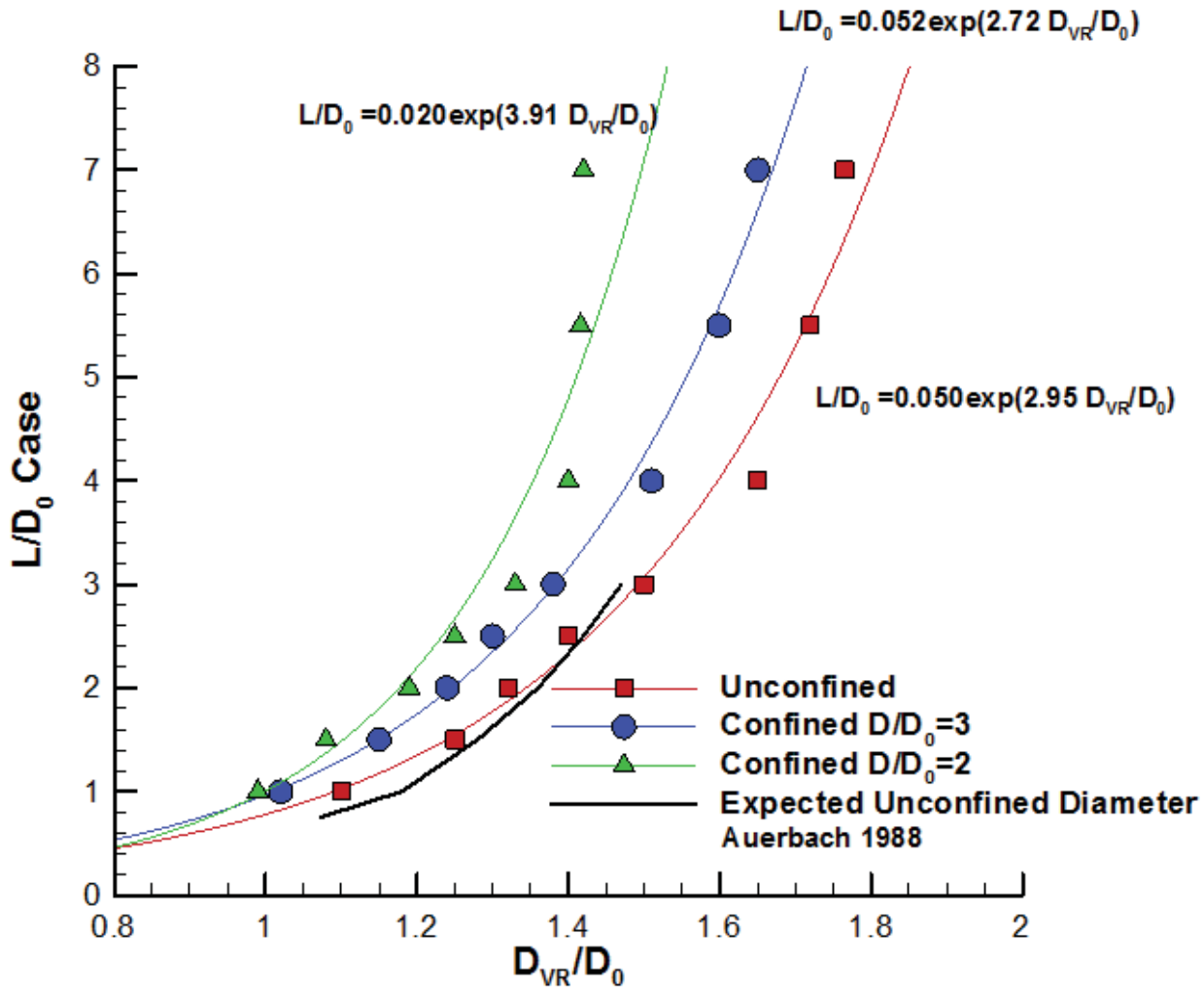

Figure 3.6: Normalized vortex ring diameter versus all L/D_0 cases, displaying the unconfined, confined, and calculated vortex ring diameter values.

The onset of circulation decay time for each D/D_0=2 confinement case was determined as the time at which the circulation began to decrease. These nondimensional times, shown as orange circles, along with the previously reported (Figure 3.4) nondimensional time of pinch-off, shown as green triangles, are displayed in Figure 3.7A versus the L/D_0 case. From this analysis, we see that the nondimensional time between pinch-off and the onset of circulation decay decreases with the L/D_0 value, therefore with increasing circulation strength and vortex ring diameter. Two breakdown timescale regions are present and are separated by the vertical line in Figure 3.7A. The first is the L/D_0 <4 cases which show a substantial lag between the vortex ring pinch-off and the onset of circulation decay. The second consists of the L/D_0 =4 and greater cases where the maximum attainable circulation is reached, which display circulation decay beginning immediately after pinch-off.

Also displayed in Figure 3.7 is the nondimensional time at which the vortex ring breaks down, shown as purple diamonds. The breakdown was defined as the time when the vortex core vorticity fell below one third of its peak vorticity value. The time between the onset of circulation decay and the vortex ring break down increases with L/D_0, this is due to the relatively constant circulation decay rate and increasing circulation strength of the vortex rings with increasing L/D_0. The normalized circulation decay rate over nondimensional time T is displayed in Table 3.2 showing similar decay rates for all L/D_0 cases greater than 1. As the peak circulation strength grows with increasing L/D_0 value and the decay rate remains the same, the time delay between the onset of circulation decay and vortex ring breakdown grows.

Previous work by Paireau et al. [29] on a single vortex subject to external adverse shear displays a decay of the vortex vorticity within increasing external shear. In their work, vortices generated within regions of low shear do not display decreasing vorticity over time. Vortices produced within intermediate ranges of shear display maximum vorticity values which initially remain constant and then sharply decrease. Vortices produced within regions of high shear display an immediate decrease in vorticity due to rapid stretching of the vortex in the direction of shear. The transition from constant vorticity values to abruptly decreasing vorticity was attributed to a transition from the initial stage of deformation and breakdown of the external layers of the vortex to the second stage which includes stretching and distortion of the vortex core. The study found that the onset of the transition from the first stage to the second stage occurred earlier with increasing shear magnitude.

Similarly in our study, increasing circulation value in combination with increasing vortex ring diameter results in increasing shear on the vortex cores. Figure 3.7B displays the same three times of interest plotted versus a ratio of confinement to dissipative length scales of $\alpha=(D-D_{VR})/2\sqrt{(vt)}$, where t is

the time of interest in seconds and v is the kinematic viscosity. In this figure, we see that α of the vortex ring pinch-off is dependent on the L/D_0 value with the inverse of the relationship sown in Figure 3.7A. The α values of the onset of circulation decay and the vortex ring breakdown are approximately constant with L/D_0 values >2. The vortex ring pinch-off α value asymptotically decreases to the constant α value of the onset of circulation decay as vortex rings begin to pinch-off after the maximum attainable circulation is reached at a L/D_0>=4 where the vortex ring circulation immediately begins to decay after pinch-off.

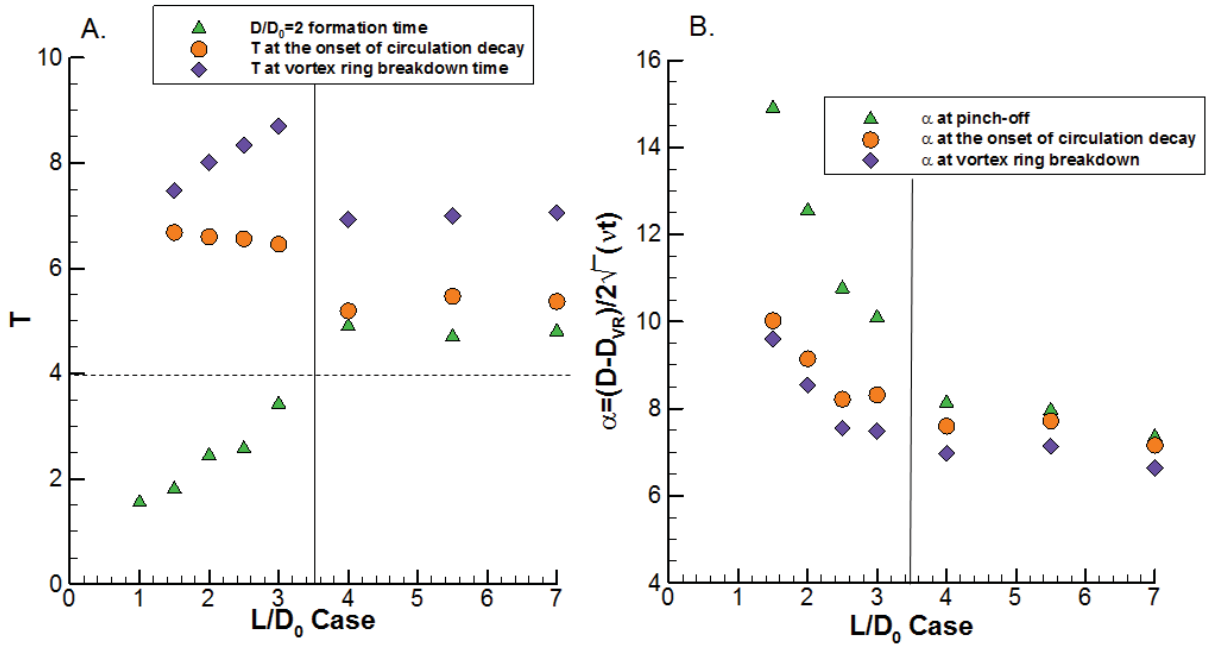

Figure 3.7: Three important times of interest within the formation and progression of the D/D_0 =2 confined vortex rings shown as nondimensional time T in A. and shown as a ratio of confinement to dissipative length scales $\alpha=(D-D_{VR})/2\sqrt{(tv)}$ in B. First, the time of the vortex ring pinch-off. Second, the time when the circulation begins to decay compared to an identical unconfined vortex ring. Third, the time at with the vortex ring breakdown occurs.

Table 3.2: Normalized circulation decay rate over nondimensional time for each L/D_0 case. Normalized circulation decay rate is $-d(\Gamma/\nu)/dT$.

L/D_0 Case	Normalized Circulation Decay
1	98
1.5	1191
2	909
2.5	818
3	1001
4	863
5.5	1182
7	1091

An in depth analysis of the vortex ring dynamics over time was necessary to study the physical mechanism responsible for the vortex ring breakdown. Figure 3.8A and Figure 3.9A display the positive and negative core circulations for two representative cases with L/D_0=2 and L/D_0=4 confinement. The L/D_0=2 case displays a vortex ring which has a time delay between the onset of circulation decay and the vortex ring breakdown. A secondary vortex ring is generated along the confinement walls behind the primary vortex core. The development of this ring leads to a slow decrease in the primary vortex ring circulation due to vorticity annihilation by cross-diffusion between the primary vortex core and the opposite sign vorticity generated at the walls. As the primary vortex core vorticity continues to diffuse the vortex ring diameter slightly decreases and the primary vortex core areas slightly grow in size and begin to interact with one another along the centerline of the confinement domain. This trend of a long nondimensonal time between pinch-off and the onset of decay was shown on the L/D_0 =2 through L/D_0=3 cases and is demonstrated by the schematics in Figure 3.8B. The L/D_0=4 case displays a much shorter time delay between vortex ring circulation decay and breakdown. Once again a secondary vortex ring is generated behind the primary vortex ring although in this case, the secondary vortex ring is smaller in size and strength to the primary vortex ring, although larger in size and strength than the L/D_0=2 case. This stronger secondary vortex ring in addition to the increased shear on the vortex core leads to a much more rapid breakup of the primary vortex ring before the ring propagates within the confinement domain. Similar to the work by Paireau et al. [29], this case displays a deformation of the vortex core, causing the primary vorticies to elongate along the shearing direction before vortex ring breakdown. This trend was displayed on the L/D_0=4 through L/D_0=7 cases and is demonstrated in the schematic in Figure 3.9B.

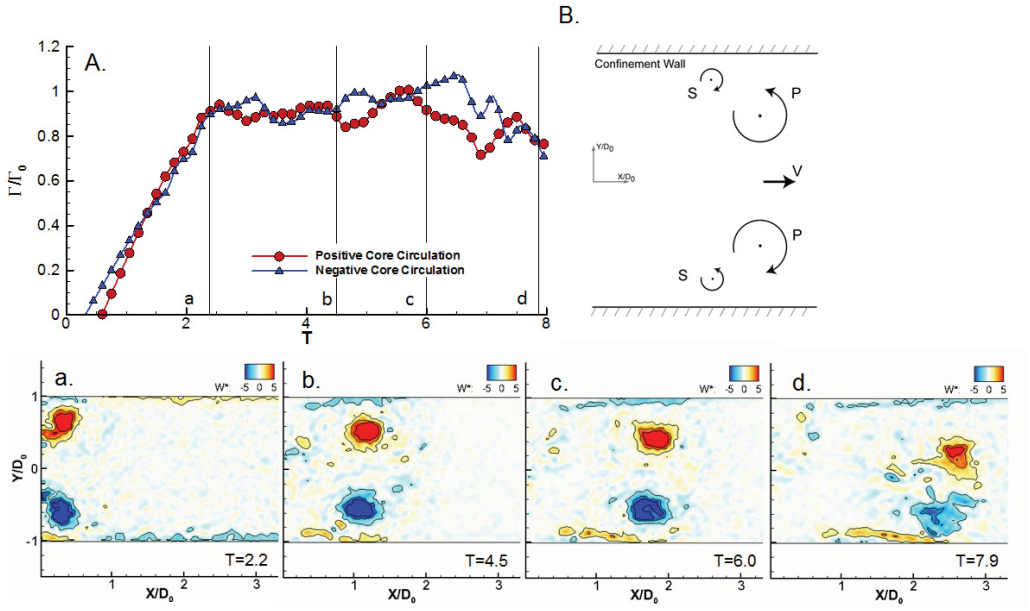

Figure 3.8: Circulation versus nondimensional time T and vorticity fields for the $D/D_0=2$ $L/D_0=2$ case. A. Positive and negative core circulation values versus nondimensional time T. B. Schematic of the primary and secondary vortex rings. a-d. Vorticity fields at four nondinensional times indicated by the vertical lines in A.

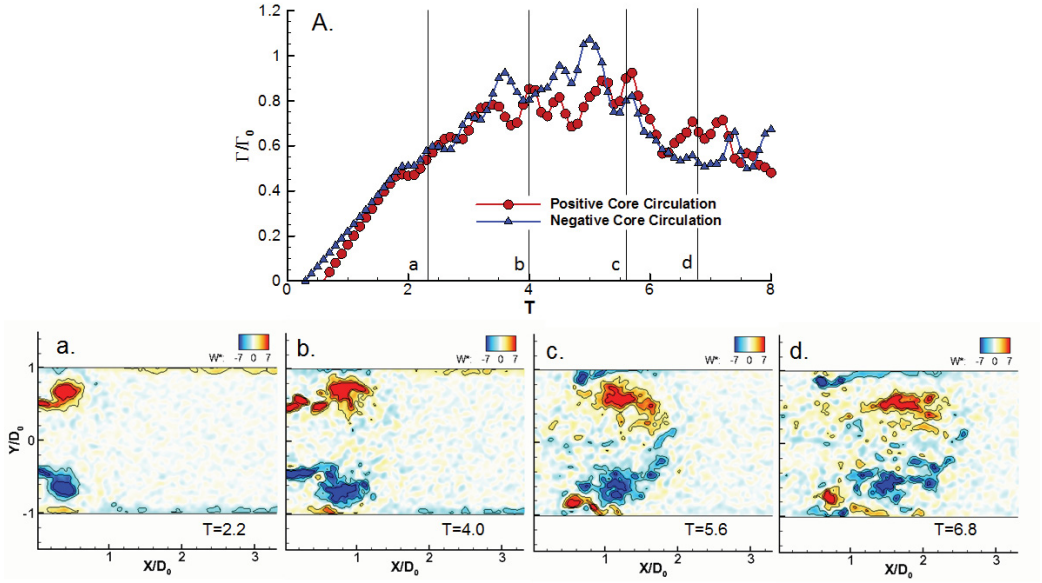

Figure 3.9: Circulation versus nondimensional time T and vorticity fields for the $D/D_0=2$ $L/D_0=4$ case. A. Positive and negative core circulation values versus nondimensional time T. a-d. Vorticity fields at four nondinensional times indicated by the vertical lines in A.

3.5 Discussion

The dynamics of vortex rings produced by a piston cylinder arrangement with downstream confinement was investigated to determine the effect of confined downstream domains on vortex ring formation and decay. Within this work we found that the formation and peak circulation strength of the generated vortex ring are relatively unaltered by the confinement. However, a decay in circulation strength over time rate was seen in the D/D_0=2 confined vortex rings. The time at which the circulation began to decay decreased with increasing L/D_0, whereas the smallest case, L/D_0=1, was relatively unaffected by the confinement. This can be attributed to the slight increase in vortex ring diameter with increasing L/D_0 value as shown in equation 3.7 and Figure 3.6 [30]. Although this equation only explains the increase in the vortex ring diameter for laminar vortex rings, it is assumed that the diameter of a turbulent vortex ring will also grow with increasing L/D_0 value. The increased diameter of the generated vortex ring caused an increased interaction with the shear layer at the confinement boundary. The interaction of the vortex and the opposite sign vorticity generated at the confinement wall leads to a decrease in circulation.

Three important times of interest along the progression to complete vortex ring breakdown were investigated within this study. The first is the time of vortex ring pinch-off. As expected, the vortex ring pinch-off for both confinement domains occurred at approximately the L/D_0 generating condition until an L/D_0>4, after which the vortex ring pinch-off remained at a nondimensional time of 4. For a vortex ring generated with an L/D_0>4, the maximum attainable circulation is reached at approximately T=4 causing the vortex ring to pinch-off. The second time of interest was the onset of circulation decay for vortex ring generated within confined domains. This time was investigated for vortex rings generated in a D/D_0=2 domain. The nondimensional time delay between the vortex ring pinch-off and the onset of circulation decay was shown to decrease with increasing L/D_0 value and the confinement length scale normalized by the dissipative length scale for the confined vortex rings remained constant with varying L/D_0. The third time of interest within the vortex ring progression is the vortex ring breakdown time. This nondimensional time delay between the onset of circulation decay and the inevitable breakdown lengthened with increasing L/D_0 and the normalized circulation decay rate $d(\Gamma/\nu)/dT$ was shown to be approximately constant over the range of L/D_0 cases studied (Table 3.2).

Secondary vortex rings were generated within the confinement domains just behind the primary vortex rings which led to the decay of the primary vortex ring circulation and ultimate breakdown of the primary vortex ring. As the vortex ring moves towards the confinement wall there is a thickening of the boundary layer which results in the generation of a secondary counter rotating vortical structure. The strength of the secondary vortical structure was determined by the strength of the primary vortex ring as

well as the proximity of the primary vortex core to the confinement wall. These two parameters scaled the tangential pressure gradient along the wall which was the mechanism of generation for the vorticity along the wall. Therefore, in the case of a smaller vortex ring formed with an L/D_0=2, a weak secondary vortex ring was developed behind the primary vortex ring which gradually led to the dissipation of the primary vortex ring and its breakdown. This was observed in cases in which the vortex ring diameters were less than 70% of the confinement diameter at L/D_0 values of 2 through 3. In the case of the stronger vortex ring in the L/D_0=4 and greater cases, the strong vortex core which was located very close to the confinement walls generated a strong secondary vortex ring. High shear on the vortex core led to the immediate deformation of the vortex core and the decay of the primary vortex ring circulation which was followed by the vortex ring breakdown. In these cases the vortex ring diameters were greater than 70% of the confinement diameter and the vortex ring growth is hindered by the confinement domain as shown in Figure 3.6 by the plateauing of the vortex ring diameters with increasing L/D_0 value.

This work is the first to investigate radially confined vortex rings over a range of Reynolds numbers. Previous work has been presented on simple vortex wall interaction [7, 12, 24] and elliptical vortex rings translating between two no-slip parallel walls [13] but completely confined vortex rings were not previously studied. The dynamics of the vortex ring past the formation time were greatly altered by the presence of the D/D_0=2 confined domain but the drastic circulation decay was not present in the D/D_0=3 confined domain. In the severely confined case, where the vortex ring diameter before the vortex ring breakdown was significantly decreased, the vortex ring pinch-off was shown to not be affected by the confinement domain. However, the onset of the circulation decay was shown to be dependent on the ratio of confinement to dissipative length scales. Further investigation including a wide variety of confinement domains and vortex ring Reynolds numbers is necessary to further understand the full extent of the breakdown mechanism for all confined vortex ring confinements.

3.6 References

1. Krueger, P., *Circulation and trajectories of vortex rings formed from tube and orifice openings.* Physica D: Nonlinear Phenomena, 2008. **237**(14-17): p. 2218-2222.
2. Weigand, A. and M. Gharib, *On the evolution of laminar vortex rings.* Experiments in Fluids, 1997. **22**(6): p. 447-457.
3. Pullin, D., *Vortex ring formation at tube and orifice openings.* Physics of Fluids, 1979. **22**: p. 401.
4. Didden, N., *On the formation of vortex rings: rolling-up and production of circulation.* Zeitschrift für Angewandte Mathematik und Physik (ZAMP), 1979. **30**(1): p. 101-116.
5. Gharib, M., E. Rambod, and K. Shariff, *A universal time scale for vortex ring formation.* Journal of Fluid Mechanics, 1998. **360**: p. 121-140.
6. Rockwell, D., *Vortex-body interactions.* Annual Review of Fluid Mechanics, 1998. **30**(1): p. 199-229.
7. Walker, J.D.A., C.R. Smith, A.W. Cerra, and T.L. Doligalski, *The Impact of a Vortex Ring on a Wall.* Journal of Fluid Mechanics, 1987. **181**: p. 99-140.
8. Orlandi, P. and R. Verzicco, *Vortex rings impinging on walls: axisymmetric and three-dimensional simulations.* Journal of Fluid Mechanics, 2006. **256**: p. 615-646.
9. Lim, T., T. Nickels, and M. Chong, *A note on the cause of rebound in the head-on collision of a vortex ring with a wall.* Experiments in Fluids, 1991. **12**(1): p. 41-48.
10. Luton, J. and S. Ragab, *The three-dimensional interaction of a vortex pair with a wall.* Physics of Fluids, 1997. **9**: p. 2967.
11. Lim, T., *An experimental study of a vortex ring interacting with an inclined wall.* Experiments in Fluids, 1989. **7**(7): p. 453-463.
12. Walker, J.D.A., *The Boundary Layer Due to Rectilinear Vortex.* Proceedings of the Royal Society of London. Series A, Mathematical and Physical Sciences, 1978. **359**(1697): p. 167-188.
13. Chang, T., J. Hertzberg, and R. Kerr, *Three dimensional vortex/wall interaction: Entrainment in numerical simulation and experiment.* Physics of Fluids, 1997. **9**: p. 57.
14. Escudier, M.P., J. Bornstein, and T. Maxworthy, *The Dynamics of Confined Vortices.* Proceedings of the Royal Society of London. Series A, Mathematical and Physical Sciences, 1982. **382**(1783): p. 335-360.
15. Gharakhani, A. and A.F. Ghoniem, *Simulation of the Piston Driven Flow Inside a Cylinder With an Eccentric Port.* Journal of Fluids Engineering, 1998. **120**(2): p. 319-326.
16. Shariff, K. and A. Leonard, *Vortex Rings.* Annual Review of Fluid Mechanics, 1992. **24**: p. U235-U279.
17. Glezer, A., *The formation of vortex rings.* Physics of Fluids, 1988. **31**: p. 3532.
18. Eckstein, A. and P. Vlachos, *Digital particle image velocimetry (DPIV) robust phase correlation.* Measurement Science and Technology, 2009. **20**: p. 055401.
19. Scarano, F., *Iterative image deformation methods in PIV.* Measurement Science and Technology, 2002. **13**: p. R1-R19.
20. Eckstein, A. and P. Vlachos, *Assessment of advanced windowing techniques for DPIV.* Measurement Science and Technology, 2009. **20**: p. 075402.
21. Eckstein, A.C., J. Charonko, and P. Vlachos, *Phase correlation processing for DPIV measurements.* Experiments in Fluids, 2008. **45**(3): p. 485-500.
22. Westerweel, J. and F. Scarano, *Universal outlier detection for PIV data.* Experiments in Fluids, 2005. **39**(6): p. 1096-1100.
23. Sirovich, L., *Turbulence and the dynamics of coherent structures. I- Coherent structures. II- Symmetries and transformations. III- Dynamics and scaling.* Quarterly of applied mathematics, 1987. **45**: p. 561-571.
24. Doligalski, T., C. Smith, and J. Walker, *Vortex interactions with walls.* Annual Review of Fluid Mechanics, 1994. **26**(1): p. 573-616.

25. Zhou, J., R. Adrian, S. Balachandar, and T. Kendall, *Mechanisms for generating coherent packets of hairpin vortices in channel flow.* Journal of Fluid Mechanics, 1999. **387**: p. 353-396.
26. Chakraborty, P., S. Balachandar, and R. Adrian, *On the relationships between local vortex identification schemes.* Journal of Fluid Mechanics, 2005. **535**: p. 189-214.
27. Etebari, A. and P. Vlachos, *Improvements on the accuracy of derivative estimation from DPIV velocity measurements.* Experiments in Fluids, 2005. **39**(6): p. 1040-1050.
28. Auerbach, D., *Some open questions on the flow of circular vortex rings.* Fluid Dynamics Research, 1988. **3**(1-4): p. 209-213.
29. Paireau, O., P. Tabeling, and B. Legras, *A vortex subjected to a shear: an experimental study.* Journal of Fluid Mechanics, 1997. **351**(-1): p. 1-16.
30. Lim, T. and T. Nickels, *Vortex rings.* Fluid Vortices, 1995: p. 95–153.

4 Circulation Decay of Laminar Vortex Rings in Radially Confined Domains

Kelley C. Stewart[1], Casandra L. Niebel[1], Sunghwan Jung[2], and Pavlos P. Vlachos[1]
[1]Department of Mechanical Engineering, Virginia Tech, Blacksburg, VA 24061, USA
[2]Department of Engineering Science and Mechanics, Virginia Tech, Blacksburg, VA 24061, USA

4.1 Abstract

Vortex rings (VR) have been studied extensively for many decades; however VR dynamics within radially confined domains have not received much attention despite their importance. Here we investigate the decay of circulation for laminar vortex rings using particle image velocimetry and develop a new analytical model for the evolution of the VR circulation subject to confinement. A parameter indicating the rate of vorticity production due to the presence of confinement was calculated and was shown to exponentially decay with increasing confinement. Our model displays strong agreement with experimental circulation data and for the first time allows us to predict the circulation decay based on vortex ring confinement.

4.2 Introduction

Vortex rings have been widely studied using a variety of investigation methods, with the majority of vortex ring research involving laminar vortex rings in semi-infinite domains[1-4]. The formation and propagation of piston cylinder generated vortex rings have been studied with varying generator parameters including tube and orifice opening geometries and variable piston velocity programs[1, 3, 5]. The formation time, the time at which the vortex ring attains its maximum circulation, has been shown to be influenced by the presence of co-flow and counterflow during generation[6, 7]. Vortex ring stability has also been an important subject. Within semi-infinite domains, the development of Kelvin waves has been reported for vortex rings of moderate Reynolds numbers which act to decelerate the vortex ring propagation[8, 9].

In addition vortex ring interactions with bodies and walls have been previously studied [10]. One of the most commonly studied vortex ring wall interactions involves a vortex ring impacting a wall normal to its direction of propagation. Such studies have been conducted by Walker et al.[11], Orlandi et al.[12], and others[13, 14]. They describe the formation of secondary and tertiary vortical structures at the wall using flow visualization and numerical studies. Lim[15] explored a variation of this flow by

studying the interaction of a vortex ring with an inclined wall. The study described the deformation and stretching of the vortex ring as it approached the wall and the following helical vortex lines as the vortex ring unevenly impinged the wall[15]. More complex interactions have also been reported, for example, Chang et al. studied numerically and with flow visualization, an elliptical vortex ring between two no-slip parallel walls, where counter rotating secondary vortical structures were formed at the wall[16]. Additionally, confined domains have been used to study swirling flows most commonly in association with axial-flow turbomachinery applications[17, 18].

A physical understanding of vortex ring dynamics in the presences of simple bodies and walls can augment our comprehension of vortex ring interactions within complicated domains. Vortex rings formed within radially confined domains will experience complex wall interactions compared to the case involving plane walls. However, the development of secondary vortical structures and deformation of the primary vortex ring structure are still expected to play a dominant role in the vortex ring evolution. The current study is the first that investigates the evolution of vortex rings in radially confined domains, and to develop an analytical model for predicting the decay of the vortex ring circulation as a function of this interaction.

4.3 Methods

Time resolved digital particle image velocimetry (TRDPIV) studies allowed for the investigation of vortex ring dynamics within radially wall-bounded domains. Six different cylindrical confinements were studied with diameters ranging from 1.25 to 3 times the diameter of the piston cylinder, D_0, where $D_0 = 0.0127$ meters. The optically clear cylindrical tubes were made of Fluorinated Ethylene-Proplyene (FEP). The FEP index of refraction matches that of water; hence no optical distortion was introduced. A case with no downstream confinement (semi-infinite domain) was also investigated for comparison. For all cases, the piston stroke-to-diameter ratio (L/D_0) was $L/D_0=1.2$ and the piston velocity program remained the same, with a corresponding Reynolds number of approximately 1,700 to ensure the vortex rings remained laminar

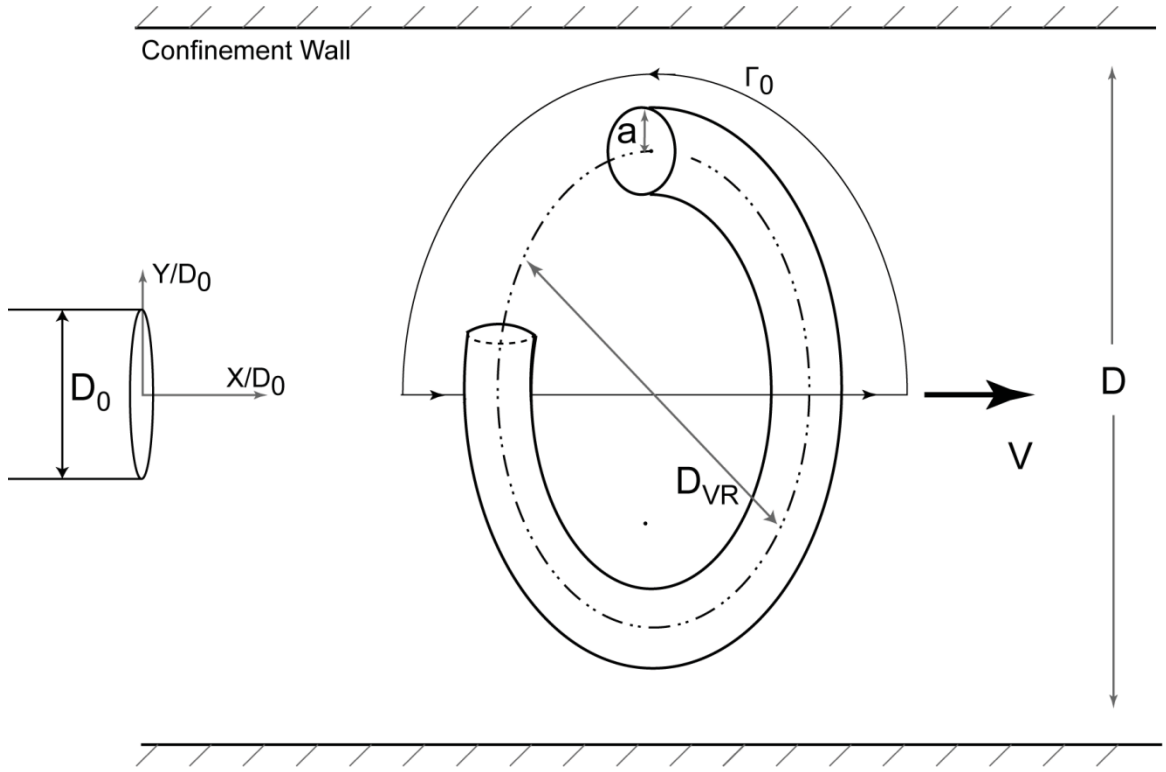

Figure 4.1: Radially confined vortex ring schematic, where the piston cylinder is located on the left with diameter D_0, the vortex ring diameter, D_{VR}, and core radius, a, are shown as well as the confinement domain diameter D.

Each test condition was repeated three times for a total of 21 test cases. After the TRDPIV data was analyzed, Proper Orthogonal Decomposition (POD) was used in order to remove high frequency noise. POD is a technique for decomposing a flow field into its fundamental components. The method calculates the optimal basis functions and determining the energy contained in each of these modes[19, 20]. In this analysis the flow fields were reconstructed with the fundamental eigenmodes which contained 95% of the total energy in the system. A local vortex identification scheme was then used to determine the location of vortex rings using the λ_{ci} criterion where the vortex core is defined using the imaginary part of the complex eigenvalue of the velocity gradient tensor, refer to Zhou and Chakraborty et al. [21, 22]. Using this method, the vortex cores were located. The circulation strength of each vortex was calculated using

$$\Gamma = \int_A \omega \cdot n ds \qquad 4.1$$

over the area determined by a constant λ_{ci} value of λ_{ci}^2=7% of the maximum value. A Compact-Richardson finite difference scheme was used to calculate vorticity fields, with low noise amplification and bias error[23].

In an effort to understand the decaying process of the confined vortex rings we developed an analytical model for the evolution of the vortex ring circulation subject to the effect of the confinement. We began by investigating the self-induced propagation velocity of a thin vortex ring [24],

$$V = \frac{\Gamma C_1}{2\pi D_{VR}} \tag{4.2}$$

where

$$C_1 = \ln \frac{4D_{VR}}{a} - \frac{1}{4}. \tag{4.3}$$

the core radius a is much smaller than the vortex ring radius $D_{VR}/2$, as shown in Figure 4.1. This provided us with a relationship between propagation velocity and circulation for a thin-cored ring with a given core radius and ring diameter.

Our problem consists of an object, in our case a coherent structure or vortex ring bubble (as referred to by Maxworthy[9]), propagating within a radially confined domain. A drag force, which is a function of the size of both the object and the confinement domain, will act on the object. This was shown by Happel and Brenner [25] who analyzed a sphere moving through a tube at low Reynolds numbers. We used the drag term to incorporate all mechanisms that will decelerate the ring such as entrainment, vorticity shedding, and the effect of the confinement walls. The drag force on the vortex ring is $F_d=C_d\rho\pi D_{VR}aV^2$, where the drag coefficient, C_d, incorporates the dependence on the confinement geometry. The drag force on the vortex ring has the similar functional form to the viscous dissipation using the potential theory by Pedley[26] and Hershberger et al.[8].

The drag force causes a loss of impulse, $I=\rho\Gamma\pi(D_{VR}/2)^2$, of the vortex ring. By assuming a constant vortex ring diameter and a constant drag coefficient, and incorporating the relationship between velocity and circulation, an equation for the time varying circulation was calculated. Equation 4.4 displays a time varying estimate of the circulation based on the peak circulation, Γ_0, at time t_0 and a constant parameter β for all values of t greater than t_0,

$$\Gamma(t) = \frac{\Gamma_0}{\Gamma_0 \beta (t - t_0) + 1} \tag{4.4}$$

where β is defined as

$$\beta = \frac{a C_d C_1^2}{\pi^2 D_{VR}^{\ 3}}. \tag{4.5}$$

The parameter β, is the only variable which is influenced by the confinement geometry. For a given condition, the rate of decay of Γ(t) is controlled by β. The parameter β represents the rate of vorticity production at the confinement walls which interacts with the vortex ring cores. As the confinement diameter decreases, the vorticity production at the wall increases and the distance between the wall and the vortex ring core decreases. These changes cause the opposite signed vorticity regions to increasingly interact and annihilate therefore raising the rate of circulation decay.

4.4 Results

Analysis of the experimental vortex ring data resulted in clear differences in the evolution of the calculated circulation values between confined and unconfined cases. Representative velocity fields for the unconfined and confined D/D_0=1.75 case are shown in Figure 4.2A and Figure 4.3A with the identified vortex cores displayed by red contours (λ_{ci}). The corresponding normalized circulation values, instantaneous circulation normalized by the peak circulation, core mean vorticity and core area values are also displayed versus the nondimensional time scale, $T=\bar{U}_p t/D_0$, in subplots B and C. It is clear that the vortex ring generated in the semi-infinite domain exhibits very little variation in circulation, core area, or core mean vorticity for T>2, after the ring is formed. However, for the D/D_0=1.75 case, as the vortex ring propagates it begins to slightly rotate its axis counterclockwise (towards the positive confinement wall) as the circulation decays and the core vorticity decreases. This continues until the vortex ring disperses at approximately T=7.5. The apparent variations between the upper and lower core circulation is caused by fluctuations in both the core areas and mean core vorticity values over time and indicates a possible instability within the confined vortex ring after formation. The vortex ring diameter remains reasonably constant among corresponding runs for the D/D_0=1.5 through D/D_0=3 cases and the semi-infinite domain. Table 4.1 displays the mean vortex ring diameter value of the three runs for each D/D_0 case and the corresponding standard deviation of diameter fluctuations. The vortex ring generated within the D/D_0=1.25 domain did not fully form in any of the runs due to the severely constricted domain. For this reason, the vortex ring diameter is not presented in Table 4.1.

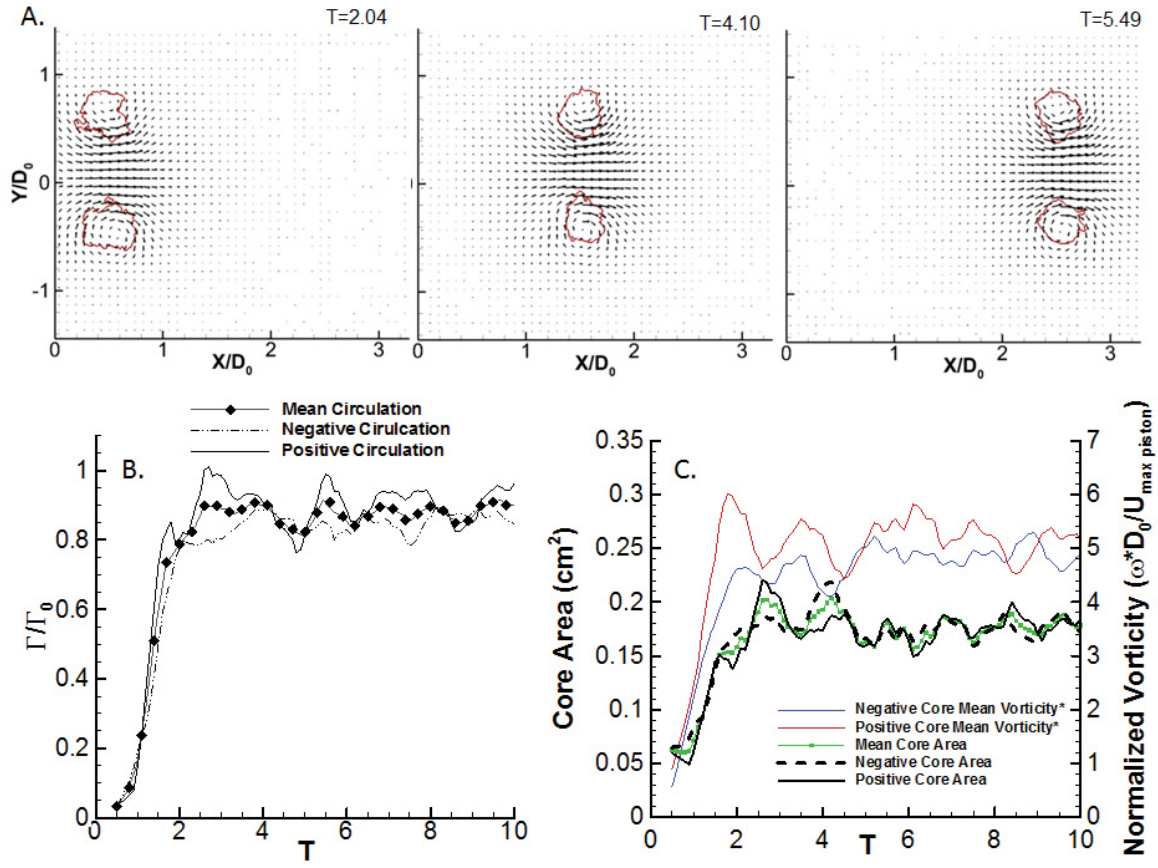

Figure 4.2: Unconfined vortex ring case. A: Velocity flow fields at three time instants. The red contours display the λ_{ci} boundaries determined for the vortex ring cores. B. Circulation versus the nondimensional time scale displaying the mean circulation as well as the negative and positive core circulation contours. C. Positive and negative vortex ring cores versus nondimensional time as well as the positive and negative core mean vorticity versus nondimensional time.

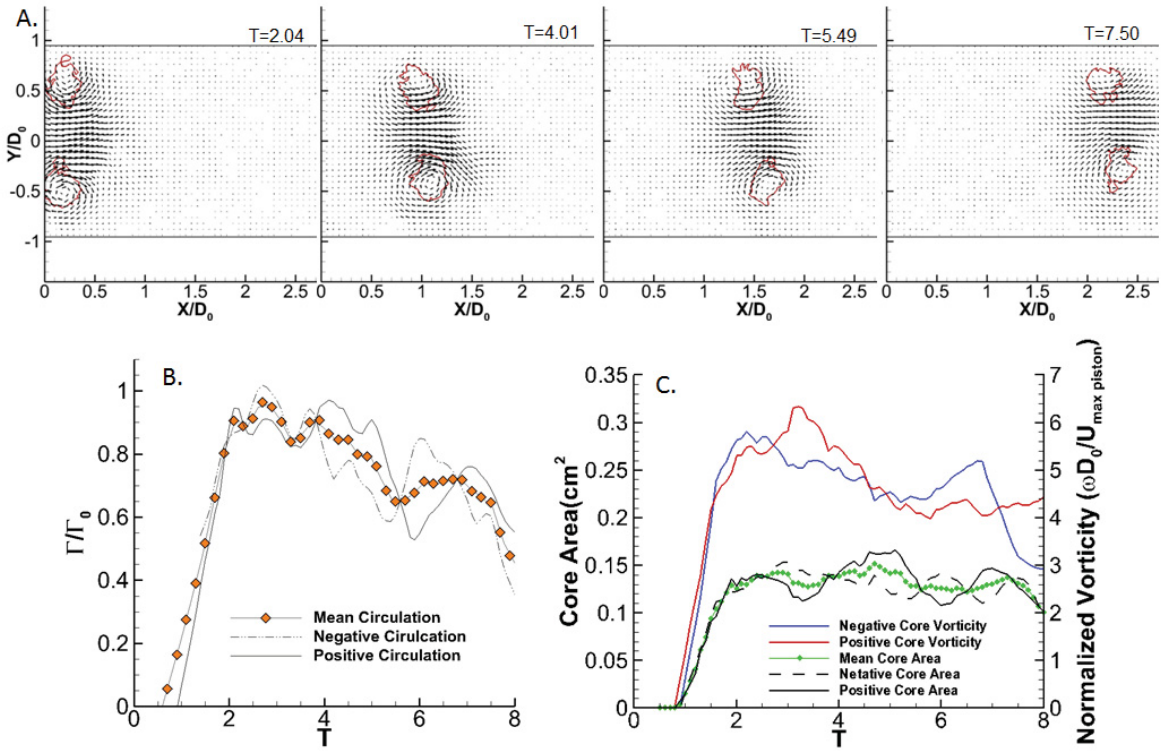

Figure 4.3: D/D_0=1.75 Confinement Case.. A: Velocity flow fields at three time instants. The red contours display the λ_{ci} boundaries determined for the vortex ring cores. B. Circulation versus the nondimensional time scale displaying the mean circulation as well as the negative and positive core circulation contours. C. Positive and negative vortex ring cores versus nondimensional time as well as the positive and negative core mean vorticity versus nondimensional time.

Table 4.1: Normalized vortex ring diameters and standard deviations for each D/D_0 case

D/D_0	Mean D_{VR}/D_0	Standard deviation of D_{VR}/D_0
1.5	0.790	0.109
1.75	0.923	0.140
2	1.014	0.106
2.5	0.990	0.123
3	0.990	0.044
semi-infinite	0.988	0.064

The formation phase and the nondimensional formation time at which pinch-off occurred was unaffected by the introduction of the downstream confinement as shown in Figure 4.4. The points displayed in Figure 4.4 are averaged values from the total data set for each case within 0.015 second time bins where the error bars display one standard deviation from the mean on every other data point for clarity. In the unconfined semi-infinite case, the circulation normalized by peak circulation, Γ_0, rises to peak just before T=2 and then plateaus. The introduction of the outer confinement causes the normalized circulation to decay with increasing severity as the confinement ratio (D_{VR}/D) increases and the ratio of the confinement diameter to piston cylinder diameter (D/D_0) decreases.

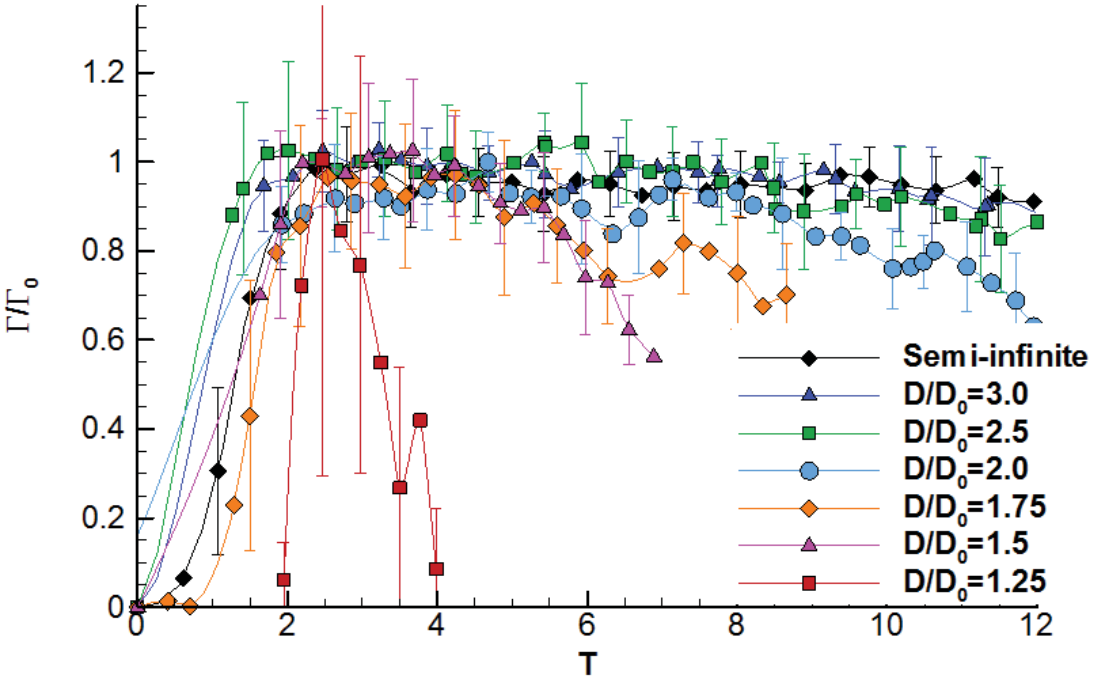

Figure 4.4: Normalized circulation versus the nondimensional time scale. Data points display the mean circulation value for 0.015 second windows of data versus the nondimensional time. The error bars display plus or minus one standard deviation on the circulation mean. The error bars and displayed for every other data point for viewing clarity.

The duration over which the vortex ring circulation decayed was further investigated. An experimental β value was calculated for each confinement condition, using equation 4.4 where $\Gamma(t)$ was the total circulation data set for each case. The experimental values, shown on the semi-log plot in Figure 4.5 in blue squares, follow an exponential decay with decreasing vortex ring confinement ratio (D_{VR}/D). Only the D/D_0=1.5-3.0 data sets were used to calculate experimental β values because the D/D_0=1.25 case violated the model assumption of constant diameter due to the incomplete formation of a vortex ring.

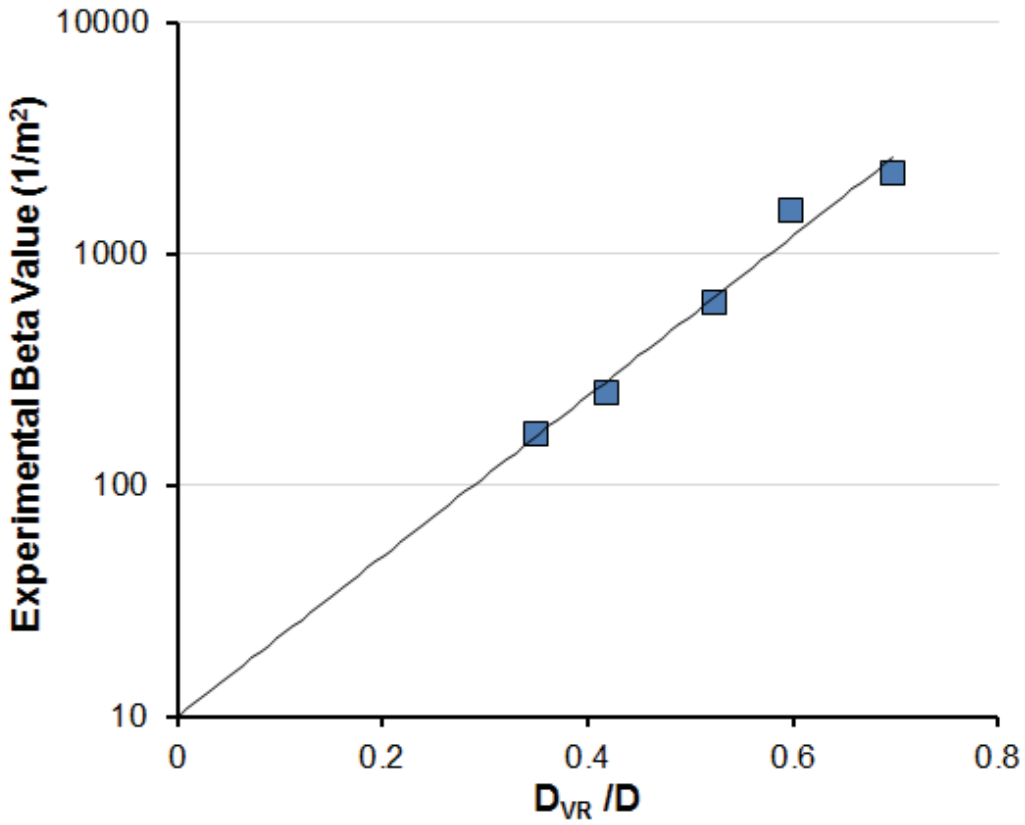

Figure 4.5: Experimentally calculated Beta values versus the vortex ring confinement ratio (vortex ring diameter versus confinement domain diameter) displaying an exponential decay with increasing vortex ring confinement.

The exponential fit of the experimental β values was used to replace the unknown confinement ratio function in C_d as shown in equation 4.6. The exponential fit y-intercept value 4.38/m^2 was then used to estimate the C_d^0 as the limit of D_{VR}/D goes to zero representing semi-infinite conditions. The resulting C_d^0 was 0.0052,

$$C_d = C_d^0 \exp\left(9.50 \frac{D_{VR}}{D}\right). \qquad 4.6$$

From this analysis, a constant model derived β value was calculated for each confinement ratio, assuming that the vortex ring diameter and core radius are constant. The varying circulation, $\Gamma(t)$, was then estimated for a given confinement ratio and peak circulation during the decay region using equation 4.4. The model calculated and experimental circulation decay values are plotted in Figure 4.6 versus the nondimensional deceleration time,

$$T^*_{deceleration} = \frac{(t - t_0)\Gamma_0}{D^2_{VR}} \quad . \qquad 4.7$$

Figure 4.6 displays the linear least squares fit of the relationship

$$\frac{\Gamma(t)}{\Gamma_0} = \frac{1}{\Gamma_0 \beta (t - t_0) + 1} \qquad 4.8$$

for the complete data set of all three runs for each case with corresponding one standard deviation error bars. The error observed within the data was primarily due to fluctuations in the mean core vorticity as shown in Figure 4.3C as opposed to simply experimental error. It is important to note that Figure 4.6 only displays time past the peak circulation time, t_0. The model calculated circulation contours strongly agree with the experimental data. Similarly, the model fit of the experimental data is shown in Figure 4.7 which is recast to collapse onto a single linear line with a slope of one.

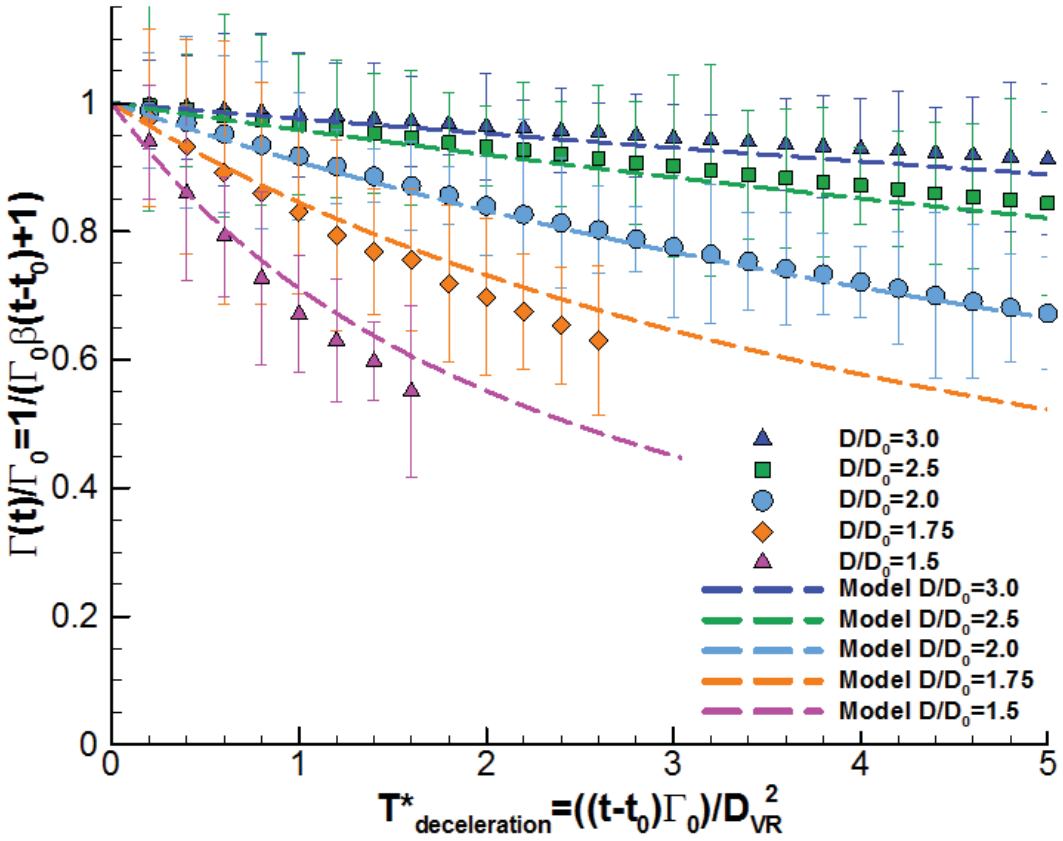

Figure 4.6: Modeled and experimental normalized circulation values versus nondimensional deceleration time of the circulation decay, where the $T^*_{deceleration} = ((t-t_0)\Gamma_0)/D_{VR}^2$. The error bars display plus or minus one standard deviation on the $\Gamma(t)/\Gamma_0 = 1/(\Gamma_0\beta(t-t_0)+1)$ linear least squares fit.

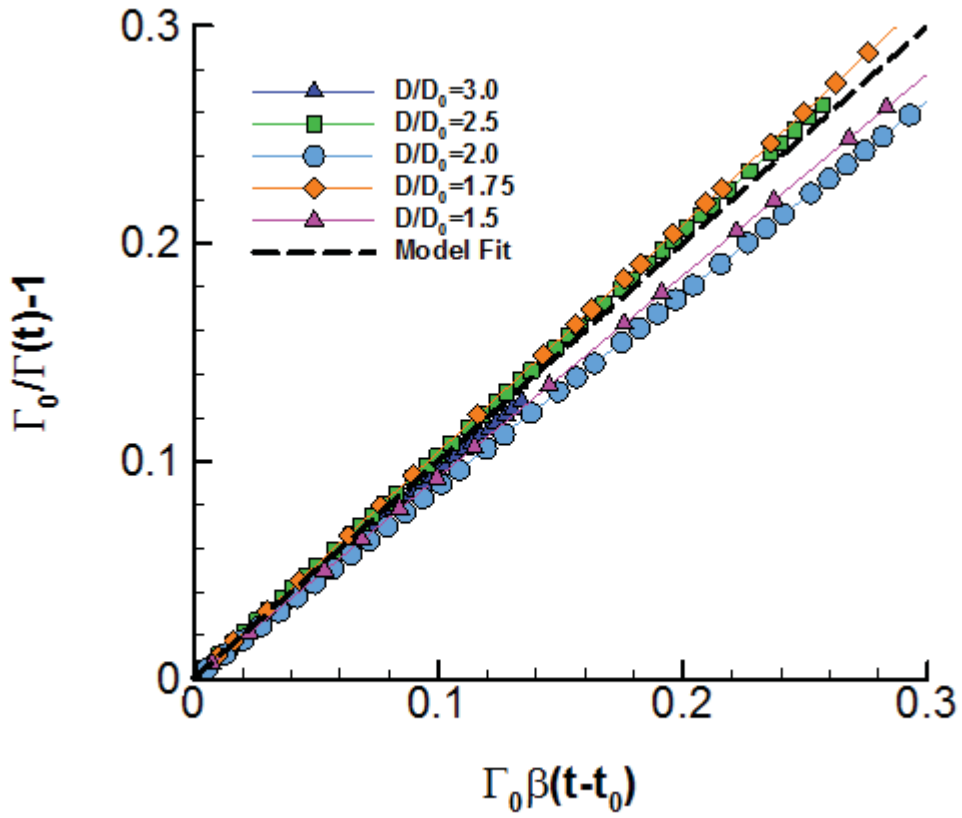

Figure 4.7 : Modeled and experimental data displaying strong agreement between the experimental data and model fits with a single linear line with a slope of one. Data displays the linear least squares fit for the relationship $\Gamma_0/\Gamma(t)-1 = \Gamma_0\beta(t-t_0)$.

4.5 Discussion

Although a range of vortex ring wall interaction studies have been previously considered, the effects of radial confinement ratio on vortex ring dynamics has received very little attention to date. In our experimental analysis, the vortex ring formation was unaffected by the introduction of the confinement. However the normalized vortex ring circulation decayed in the presence of the radial confinement and the decay rate was amplified by increasing vortex ring confinement. Hence, we developed a semi-empirical model for physically representing the circulation decay for a thin-core vortex ring traveling in a cylindrical domain. The experimentally calculated decay coefficient, β, was found to exponentially grow with decreasing domain size leading to increased circulation decay. The vortex ring "drag coefficient" was estimated using the exponential fit of the experimental β values as the limit of D_{VR}/D approaches 0 approximating semi-infinite conditions. In this work, the "drag" on the vortex ring is

used as the combination of effects that act to oppose the motion of the vortex ring. The estimated "drag coefficient" for a semi-infinite domain is C_d=0.0052. This drag coefficient can be most similarly related to the drag coefficient of an air bubble in water due to the internal circulation of the moving bubble and decreased velocity gradients on the bubble surface

The time varying circulation was estimated by the semi-empirical model for the six confined conditions beginning after peak circulation time. The model circulation decay values displayed a strong agreement with the experimental circulation values for the D/D_0=1.5 to 3.0 cases. In all confined cases, the presence of the confinement walls affected the propagation and decay of the vortex ring after formation. Induced surface vorticity was generated at the domain wall, due to tangential pressure gradient [27], which was of opposite sign of the near wall vortex. The interaction of the opposite sign vorticities of the vortex and confinement wall led to decreased circulation of the vortex. Fluctuations within the vortex core areas were observed for all confined vortex rings. Similar core-area fluctuations have been previously reported for vortex rings impacting an inclined wall[15], vortex rings cut by a thin plate[16], and elliptic vortex rings interacting with two no-slip parallel walls[15, 16, 28]. In the later study, the core-area fluctuations are generated by vortex stretching at the impacted wall, these fluctuations were not taken into account in the current model.

We illustrated that the circulation decay rate increased exponentially with increasing vortex ring confinement. However this relationship only holds above a specific confinement bound where the laminar vortex ring properly forms and maintains a relatively constant diameter. When too severely confined, as in the case of the D/D_0=1.25 confinement, the vortex ring does not fully form due to increased viscous shear stresses at the wall. In this case the vortex ring is not present and the circulation does not decay as the model predicts. As the confinement diameter grows with respect to the piston cylinder diameter, the model is completely valid and the vortex ring begins to resemble an unconfined vortex ring as in the D/D_0=3 case. With increasing confinement diameter, the vortex ring circulation will decay much slower and begin to mimic a semi-infinite domain vortex ring with a constant circulation after the formation time.

Estimating the rate of vortex ring circulation decay within important physical processes is essential to fully understanding the beneficial or unfavorable effects the production of vortex rings will produce. For example vortex ring production within the left ventricle during early diastolic filling is beneficial to efficient filling and to the redirection of blood for ejection. When the heart becomes diseased and loses its ability to properly relax, the left ventricular walls provide increasing confinement for the incoming fluid and the vortex ring dynamics are drastically altered. This improved understanding

of vortex ring circulation decay and the model for predicting the decay rate in confined domains can be utilized in a wide range of applications to more completely understand the role of laminar vortex ring dynamics in confined domains.

4.6 References

1. Krueger, P., *Circulation and trajectories of vortex rings formed from tube and orifice openings.* Physica D: Nonlinear Phenomena, 2008. **237**(14-17): p. 2218-2222.
2. Weigand, A. and M. Gharib, *On the evolution of laminar vortex rings.* Experiments in Fluids, 1997. **22**(6): p. 447-457.
3. Pullin, D., *Vortex ring formation at tube and orifice openings.* Physics of Fluids, 1979. **22**: p. 401.
4. Didden, N., *On the formation of vortex rings: rolling-up and production of circulation.* Zeitschrift für Angewandte Mathematik und Physik (ZAMP), 1979. **30**(1): p. 101-116.
5. Dabiri, J. and M. Gharib, *Starting flow through nozzles with temporally variable exit diameter.* Journal of Fluid Mechanics, 2005. **538**: p. 111-136.
6. Dabiri, J. and M. Gharib, *Delay of vortex ring pinchoff by an imposed bulk counterflow.* Physics of Fluids, 2004. **16**: p. L28.
7. Krueger, P., J. Dabiri, and M. Gharib, *The formation number of vortex rings formed in uniform background co-flow.* Journal of Fluid Mechanics, 2006. **556**: p. 147-166.
8. Hershberger, R., D. Bolster, and R. Donnelly, *Slowing of vortex rings by development of Kelvin waves.* Physical Review E 2010. **82**: p. 036309.
9. Maxworthy, T., *The structure and stability of vortex rings.* Journal of Fluid Mechanics, 1972. **51**(01): p. 15-32.
10. Rockwell, D., *Vortex-body interactions.* Annual Review of Fluid Mechanics, 1998. **30**(1): p. 199-229.
11. Walker, J.D.A., C.R. Smith, A.W. Cerra, and T.L. Doligalski, *The Impact of a Vortex Ring on a Wall.* Journal of Fluid Mechanics, 1987. **181**: p. 99-140.
12. Orlandi, P. and R. Verzicco, *Vortex rings impinging on walls: axisymmetric and three-dimensional simulations.* Journal of Fluid Mechanics, 2006. **256**: p. 615-646.
13. Lim, T., T. Nickels, and M. Chong, *A note on the cause of rebound in the head-on collision of a vortex ring with a wall.* Experiments in Fluids, 1991. **12**(1): p. 41-48.
14. Luton, J. and S. Ragab, *The three-dimensional interaction of a vortex pair with a wall.* Physics of Fluids, 1997. **9**: p. 2967.
15. Lim, T., *An experimental study of a vortex ring interacting with an inclined wall.* Experiments in Fluids, 1989. **7**(7): p. 453-463.
16. Chang, T., J. Hertzberg, and R. Kerr, *Three dimensional vortex/wall interaction: Entrainment in numerical simulation and experiment.* Physics of Fluids, 1997. **9**: p. 57.
17. Escudier, M.P., J. Bornstein, and T. Maxworthy, *The Dynamics of Confined Vortices.* Proceedings of the Royal Society of London. Series A, Mathematical and Physical Sciences, 1982. **382**(1783): p. 335-360.
18. Gharakhani, A. and A.F. Ghoniem, *Simulation of the Piston Driven Flow Inside a Cylinder With an Eccentric Port.* Journal of Fluids Engineering, 1998. **120**(2): p. 319-326.

19. Sirovich, L., *Turbulence and the dynamics of coherent structures. I- Coherent structures. II- Symmetries and transformations. III- Dynamics and scaling.* Quarterly of applied mathematics, 1987. **45**: p. 561-571.
20. Doligalski, T., C. Smith, and J. Walker, *Vortex interactions with walls.* Annual Review of Fluid Mechanics, 1994. **26**(1): p. 573-616.
21. Zhou, J., R. Adrian, S. Balachandar, and T. Kendall, *Mechanisms for generating coherent packets of hairpin vortices in channel flow.* Journal of Fluid Mechanics, 1999. **387**: p. 353-396.
22. Chakraborty, P., S. Balachandar, and R. Adrian, *On the relationships between local vortex identification schemes.* Journal of Fluid Mechanics, 2005. **535**: p. 189-214.
23. Etebari, A. and P. Vlachos, *Improvements on the accuracy of derivative estimation from DPIV velocity measurements.* Experiments in Fluids, 2005. **39**(6): p. 1040-1050.
24. Saffman, P., *Vortex dynamics*. 1995: Cambridge Univ Pr.
25. Happel, J. and H. Brenner, *Low Reynolds number hydrodynamics*: Noordhoff International Publishing.
26. Pedley, T., *The toroidal bubble.* Journal of Fluid Mechanics, 1968. **32**(01): p. 97-112.
27. Morton, B., *The generation and decay of vorticity.* Geophysical & Astrophysical Fluid Dynamics, 1984. **28**(3): p. 277-308.
28. Weigand, A., *The response of a vortex ring to a transient, spatial cut*. 1993, California Univ., San Diego, La Jolla, CA (United States).

4.7 Supplementary Material

4.7.1 Experimental Setup

Time resolved digital particle image velocimetry (TRDPIV) studies allowed for the investigation of vortex ring dynamics within radially wall-bounded domains. Six different cylindrical confinements were studied with diameters ranging from 1.25 to 3 times the diameter of the piston cylinder, D_0, where D_0 = 0.0127 meters. The optically clear cylindrical tubes were made of Fluorinated Ethylene-Proplyene (FEP). The FEP index of refraction matches that of water; hence no optical distortion was introduced. A case with no downstream confinement (semi-infinite domain) was also investigated for comparison. For all cases, the piston stroke-to-diameter ratio (L/D_0) was L/D_0=1.2 and the piston velocity program remained the same, with a corresponding Reynolds number of approximately 1,700 to ensure the vortex rings remained laminar

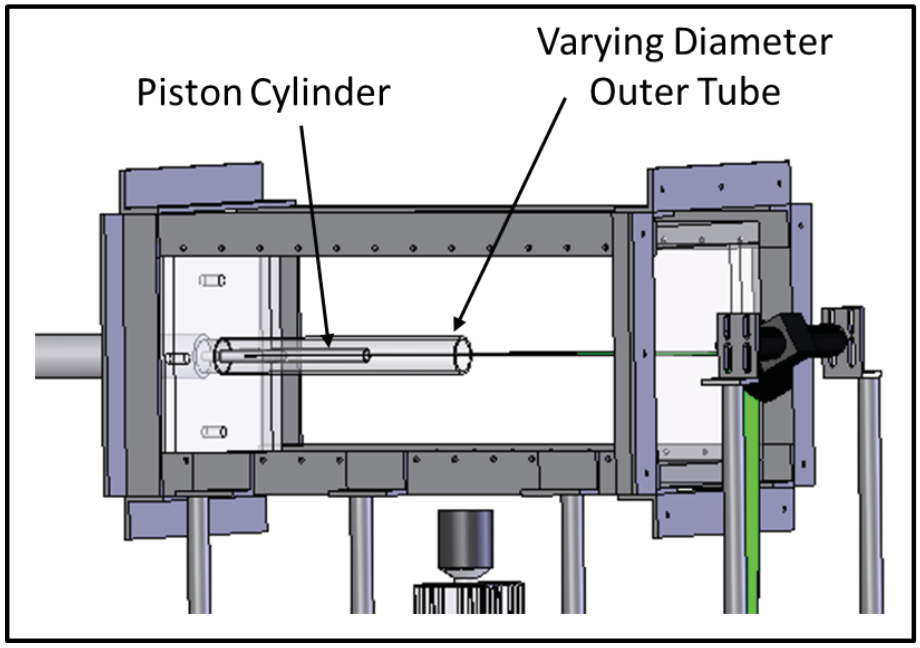

Figure 4.8: Schematic of vortex ring formation experimental setup with varying downstream diameter conditions.

Vortex rings were generated by a discharge of fluid from a piston cylinder arrangement driven by a pneumatic cylinder over a finite time interval. The piston cylinder's travel remained constant for all cases based on the L/D_0 value. This process can be approximated by considering the slug-flow model where we assume uniform flow over the circular outlet jet and we neglect the initial transient period [1-3]. The pneumatic cylinder was used in combination with a Teflon piston cap to produce the vortex rings.

The region of interest began immediately downstream of the small piston cylinder's end. The velocity of the piston was measured using a Novotechnik linear TLH series potentiometer. The mean velocity with respect to time was calculated using

$$\overline{U}_p = \frac{1}{T}\int_0^T u_p(t)dt, \tag{4.9}$$

where $u_p(t)$ is the velocity of the piston, which is assumed to be equal to the jet outflow velocity and assumed constant over the jet area, at time t and T is the total ejection time interval.

Planar TRDPIV is an optical flow measurement technique which uses a coherent light source to illuminate a region of interest. The coherent light source is expanded into a thin plane and directed over a region of interest parallel to a high speed camera lens face. The flow is seeded with neutrally-buoyant flow tracer particles; the movement of these flow tracer particles is captured by high speed images. Cross correlation techniques are used to obtain planes of velocity vectors within the region of interest from the flow tracer displacements between high speed images.

The laser plane was positioned parallel to the piston cylinder and the high speed camera was positioned beside the test setup perpendicular to the laser plane. All data was acquired using a 1 kHz Nd:YAG dual Head laser. Double pulsed laser pulses separated by 0.02 seconds were used to acquire data synchronized with an IDT XS-3 CMOS camera. The images acquired within this region were 1280 pixels by 288-700 pixels based on ROI size. The magnification was optimized at 58 or 62 microns per pixel based on ROI size. Neutrally-buoyant silver coated hollow glass spheres 85 μm were used as flow tracers.

Cross correlation algorithms were performed to calculate the velocity fields on a uniform grid of 319 x 70-173 locations with a vector grid spacing of 4 pixels equaling 232 or 248μm. Five passes of a robust phase correlation based deformation method algorithm were used with a grid resolution of 16x16 vectors and a window resolution of 32x32 vectors on the first two passes [4-7]. The final passes had a grid resolution of 4x4 and a window resolution of 16x16 vectors. Area validation using median filters were implemented in order to remove stray vectors. Based on the magnification and the laser timing, a typical displacement of the flow tracers between correlated frames was on the order of 4-8 pixels.

Proper Orthogonal Decomposition is a technique for decomposing a flow field into its fundamental components. The method calculates the optimal basis functions and determining the energy contained in each of these modes [8, 9]. POD was used to post process the TRDPIV results in order to

remove high frequency noise. In this analysis the flow fields were reconstructed with the fundamental eigenmodes which contained 95% of the total energy in the system.

A local vortex identification scheme was used to determine the location of vortex rings using the λ_{ci} criterion where the vortex core is defined using the imaginary part of the complex eigenvalue of the velocity gradient tensor, refer to Zhou and Chakraborty et al. [10, 11]. Using this method, the vortex cores were located. The circulation strength of each vortex was calculated using

$$\Gamma = \int_A \omega \cdot n ds \tag{4.10}$$

over the area determined by a constant λ_{ci} criterion function value of λ_{ci}^2=7% of the maximum value. A Compact-Richardson finite difference scheme was used to calculate vorticity fields, providing low noise amplification and bias error [12].

4.7.2 Model Derivation

In an effort to understand the decaying process of the confined vortex rings we developed an analytical model for the evolution of the vortex ring circulation subject to the effect of the confinement. We began by investigating the self-induced propagation velocity of a thin vortex ring, equation 4.11 [13], where the core radius a is much smaller than the vortex ring radius $D_{VR}/2$, as shown in Figure 4.1,

$$V = \frac{\Gamma C_1}{2\pi D_{VR}} \left(\ln \frac{4D_{VR}}{a} - \frac{1}{4} \right), \tag{4.11}$$

where

$$C_1 = \ln \frac{4D_{VR}}{a} - \frac{1}{4}. \tag{4.12}$$

This provided us with a relationship between propagation velocity and circulation for a thin-cored ring with a given core radius and ring diameter.

Our problem consists of an object, in our case a coherent structure or vortex ring bubble (as referred to by Maxworthy [14]), propagating within a radially confined domain. A drag force, which is a function of the size of both the object and the confinement domain, will act on the object. This was

shown by Happel and Brenner [15] who analyzed a sphere moving through a tube at low Reynolds numbers, equation 4.13,

$$F_d \approx 6\pi\mu a_b U_b \left(1 + f\left(\frac{D_b}{D}\right)\right), \tag{4.13}$$

where D_b is the object diameter, D is the tube diameter, a_b and U_b are the radius and velocity of the moving object respectively. Following work by Hershberger et al. and Sullivan et al. we aim to define a "drag coefficient" of the vortex ring [16, 17]. In our work, we use the drag term to incorporate all mechanisms that will slow the ring down such as entrainment, vorticity shedding, and the effect of the confinement walls. The drag force on the vortex ring is:

$$F_d = C_d \rho \pi D_{VR} a V^2, \tag{4.14}$$

where the drag coefficient, C_d, incorporates the dependence on the confinement geometry as shown in equation 4.15. The drag force on the vortex ring has the similar functional form to the viscous dissipation using the potential theory by Pedley[18] and Hershberger et al.[17],

$$C_d = C_d^0 \left[1 + g\left(\frac{D_{VR}}{D}\right)\right]. \tag{4.15}$$

The drag force causes a loss of impulse, $I=\rho\Gamma\pi(D_{VR}/2)^2$, of the vortex ring resulting in the following equation,

$$\frac{1}{2}\rho C_d V^2 \pi \left(\frac{D_{VR}}{2}\right)^2 = -\frac{dI}{dt}. \tag{4.16}$$

By assuming a constant vortex ring diameter and a constant drag coefficient, and incorporating the relationship between velocity and circulation in equation 4.11, the following relationship is derived,

$$\rho C_d \pi D_{VR} a \left(\frac{\Gamma C_1}{2\pi D_{VR}}\right)^2 = -\frac{d}{dt}\left(\rho\pi\Gamma (D_{VR}/2)^2\right) \tag{4.17}$$

$$\frac{C_d C_1^2 a \Gamma^2}{\pi^2 D_{VR}^3} = -\frac{d\Gamma}{dt}. \tag{4.18}$$

In our study, assuming a constant vortex ring diameter is valid for the laminar vortex rings generated in confinement domains larger than D/D_0=1.25. All confinement domains larger than this produced vortex rings with a relatively constant equilibrium diameter. The D/D_0=1.25 domain did not produce a true vortex ring which propagated along the length of the tube. Instead, the ring immediately dissipated after formation. By defining a parameter β,

$$\beta = \frac{aC_d C_1^2}{\pi^2 D_{VR}{}^3} \tag{4.19}$$

this equation becomes,

$$\beta\Gamma^2 = -\frac{d\Gamma}{dt} \tag{4.20}$$

This results in equation 4.21,

$$\Gamma(t) = \frac{\Gamma_0}{\Gamma_0\beta(t-t_0)+1}, \tag{4.21}$$

which displays a time varying estimate of the circulation based on the peak circulation, Γ_0, at time t_0 and a constant parameter β for all values of t greater than t_0, where Γ_0 is the peak circulation and t_0 is the time at peak circulation.

4.7.3 Calculation of the Drag Coefficient

The vortex ring "drag coefficient" was estimated using the exponential fit of the experimental β values as the limit of D_{VR}/D approaches 0 approximating semi-infinite conditions. In this work, the "drag" on the vortex ring is used as the combination of effects that act to oppose the motion of the vortex ring. The estimated "drag coefficient" for a semi-infinite domain is C_d=0.0052. This drag coefficient can be related to the drag coefficient of an air bubble in water due to the internal circulation of the moving bubble and decreased velocity gradients on the bubble surface. The bubble drag coefficient at a Reynolds number of approximately 500 is 0.15; however at increased Reynolds numbers, the bubble begins to deform, loses its internal circulation, and the drag is then dominated by the deformation [19]. To estimate

the drag coefficient on a bubble at higher Reynolds numbers assuming there is no bubble deformation, we extrapolated the drag coefficient curve presented by Sanada et al., Clift et al., and Moore et al. [19-21] past the deformation point to a Reynolds number of 1,700, the resulting C_d value is approximately 0.05. This value is used to ensure that our C_d value for the vortex ring of 0.0052 is within the appropriate range.

4.7.4 References

1. Didden, N., *On the formation of vortex rings: rolling-up and production of circulation.* Zeitschrift für Angewandte Mathematik und Physik (ZAMP), 1979. **30**(1): p. 101-116.
2. Shariff, K. and A. Leonard, *Vortex Rings.* Annual Review of Fluid Mechanics, 1992. **24**: p. U235-U279.
3. Krueger, P., *Circulation and trajectories of vortex rings formed from tube and orifice openings.* Physica D: Nonlinear Phenomena, 2008. **237**(14-17): p. 2218-2222.
4. Eckstein, A. and P. Vlachos, *Digital particle image velocimetry (DPIV) robust phase correlation.* Measurement Science and Technology, 2009. **20**: p. 055401.
5. Eckstein, A. and P. Vlachos. *A robust phase correlation DPIV processing algorithm for time resolved measurements*. 2007.
6. Scarano, F., *Iterative image deformation methods in PIV.* Measurement Science and Technology, 2002. **13**: p. R1-R19.
7. Eckstein, A. and P. Vlachos, *Assessment of advanced windowing techniques for DPIV.* Measurement Science and Technology, 2009. **20**: p. 075402.
8. Sirovich, L., *Turbulence and the dynamics of coherent structures. I- Coherent structures. II- Symmetries and transformations. III- Dynamics and scaling.* Quarterly of applied mathematics, 1987. **45**: p. 561-571.
9. Doligalski, T., C. Smith, and J. Walker, *Vortex interactions with walls.* Annual Review of Fluid Mechanics, 1994. **26**(1): p. 573-616.
10. Zhou, J., R. Adrian, S. Balachandar, and T. Kendall, *Mechanisms for generating coherent packets of hairpin vortices in channel flow.* Journal of Fluid Mechanics, 1999. **387**: p. 353-396.
11. Chakraborty, P., S. Balachandar, and R. Adrian, *On the relationships between local vortex identification schemes.* Journal of Fluid Mechanics, 2005. **535**: p. 189-214.
12. Etebari, A. and P. Vlachos, *Improvements on the accuracy of derivative estimation from DPIV velocity measurements.* Experiments in Fluids, 2005. **39**(6): p. 1040-1050.
13. Saffman, P., *Vortex dynamics*. 1995: Cambridge Univ Pr.
14. Maxworthy, T., *The structure and stability of vortex rings.* Journal of Fluid Mechanics, 1972. **51**(01): p. 15-32.
15. Happel, J. and H. Brenner, *Low Reynolds number hydrodynamics*: Noordhoff International Publishing.
16. Sullivan, I., J. Niemela, R. Hershberger, D. Bolster, and R. Donnelly, *Dynamics of thin vortex rings.* Journal of Fluid Mechanics, 2008. **609**: p. 319-347.
17. Hershberger, R., D. Bolster, and R. Donnelly, *Slowing of vortex rings by development of Kelvin waves.* Physical Review E 2010. **82**: p. 036309.
18. Pedley, T., *The toroidal bubble.* Journal of Fluid Mechanics, 1968. **32**(01): p. 97-112.
19. Clift, R., J. Grace, and M. Weber, *Bubbles, drops, and particles*. Vol. 380. 1978: Academic press New York.
20. Sanada, T., K. Sugihara, M. Shirota, and M. Watanabe, *Motion and drag of a single bubble in super-purified water.* Fluid Dynamics Research, 2008. **40**(7-8): p. 534-545.
21. Moore, D., *The velocity of rise of distorted gas bubbles in a liquid of small viscosity.* Journal of Fluid Mechanics, 1965. **23**(04): p. 749-766.

5 Vortex Ring Formation during Left Ventricular Early Diastolic Filling

Kelley C. Stewart[1], John C. Charonko[1], Casandra L. Niebel[1], William C. Little[2], and Pavlos P. Vlachos[1]
[1] Department of Mechanical Engineering, Virginia Tec, Blacksburg, Virginia
[2] Cardiology Section, Wake Forest University School of Medicine, Winston-Salem, North Carolina

5.1 Abstract

Normal left ventricular (LV) filling occurs rapidly early in diastole from a low left atrial pressure. This normal diastolic function is altered in patients with heart failure. Such impairment of diastolic filling is manifested as an abrupt deceleration of the early filling wave velocity [1]. Although variations within the early filling wave have been observed previously [2-4], the underlying hydrodynamic mechanisms are not well understood. Here we discover that the favorable pressure difference within the ventricle driving early diastolic filling first falls to zero at the time when the early filling wave deceleration is observed and we show that the LV vortex ring pinch-off occurs simultaneously. In contrast to previous analysis, this study shows that the vortex ring pinch-off occurs before the completion of early diastole and its formation time remains invariant to changes of diastolic function.

5.2 Introduction

The heart is continuously adapting and remodeling, and these changes manifest in its ability to alter filling pressures, heart rate, and stroke volume in response to stress, exercise, or disease [5, 6]. In order for the heart to normally function, the left ventricle (LV) must not only eject blood during systole but rapidly fill during diastole without requiring an elevated left atrial pressure both at rest and when the cardiac output increases during exercise. In a healthy heart this is accomplished by the left ventricle functioning as a suction pump. Early in diastole there is a progressive pressure difference that pulls blood from the left atrium to the LV apex [7]. In left ventricular diastolic dysfunction (LVDD), the LV compliance and ability of the heart to relax and expand decrease, negatively impacting the left heart's capacity to fill and generate the favorable pressure difference from the left atrium to the left ventricle during diastole. In patients with LVDD, maintenance of LV filling requires an elevated left atrial pressure [8, 9]. This becomes especially apparent during exercise [10, 11]. Almost all patients with heart failure (HF) have abnormalities of the LV filling dynamics and over 50% of patients with HF have preserved ejection fraction (EF) [12],. Therefore, improved understanding of LVDD fluid dynamics can have a significant impact on the diagnosis and treatment across all heart failure conditions [13].

As blood flows across the mitral valve from the left atrium into the LV in early diastole, the inflow jet produces a vortex ring. These vortical structures formed within the LV during diastole have been studied both in-vivo and in-vitro [14-18]. The time at which the vortex ring's strength of hydrodynamic circulation reaches a maximum is referred to as the vortex ring formation time. At this point, the primary vortex ring detaches from the inflow jet and pinches-off. Beyond the vortex ring formation time, any additional energy does not contribute to the primary vortex ring but instead is shed into a trailing jet. The formation vortex ring within the LV inflow tract may improve the efficiency of early diastole LV filling and might be a useful metric of cardiac function [14, 19, 20]. Gharib et al. [21] hypothesized that a universal timescale may be present for formation time of optimal left ventricular filling by a vortex ring within the ventricle.

Gharib et al. [21] proposed that for a vortex ring generated by a piston-cylinder in a semi-infinite domain, a dimensionless formation time (FT) of approximately 4 represents the asymptotic limit of the circulation at which the maximum vortex ring propulsive efficiency is attained. Later, Gharib et al. calculated the dimensionless FT associated with left ventricular diastolic filling as:

$$\text{Formation Time} = \frac{U_{Mean} t_{E-wave}}{D}, \qquad 5.1$$

where U_{Mean} is the mean filling velocity, $t_{E\text{-}wave}$ is the duration of the early filling, and D is the maximum mitral valve diameter [20]. The dimensionless formation time was used as opposed to the actual time to account for variations among patients. Gharib et al. proposed that the FT can be used as a specific indicator of cardiac function. However, this analysis is based on the assumption that the vortex ring FT coincides with the duration of early diastolic filling; however this assumption has not been verified.

In this work we hypothesize that the formation of the vortex ring changes with diastolic dysfunction due to the changing geometry of the left ventricle and the decreased relaxation of the left ventricular myocardium during early filling. Color M-mode (CMM) echocardiography is a clinical imaging modality that provides a temporal special map of blood velocities during diastole along a scan line from the LV apex to the mitral valve [22] and will be used in this study to investigate the velocities and pressures within the left ventricle throughout early diastolic filling. The CMM data can be used to integrate the Euler equation providing a measurement of the intraventricular pressure difference (IVPD). The IVPD represents the strength of LV suction and therefore is an important parameter for characterizing diastolic function [8, 23-25]. Early diastolic propagation velocity (Vp), which is the velocity of propagation of the left ventricular filling wave, can also be calculated from the CMM [26].

In summary, previous studies have investigated early diastolic filling wave velocities and vortex ring dynamics with respect to cardiac function. However, the relationship between the early diastolic filling wave deceleration and the vortex ring dynamics within the left ventricle has not been considered in depth. Hence, to-date there is no established association between vortex ring FT and impaired filling dynamics as manifested by changes in the early filling Vp. This work reveals for the first time the interplay among vortex ring FT, the loss of favorable pressure difference, and early diastolic wave deceleration within the LV. In this work, we examine the early diastolic filling wave deceleration and show its relationship to the pinch-off of the vortex ring formed beyond the mitral annulus inlet. Additionally, we investigate whether the vortex ring formation characteristics are altered with the development of diastolic impairment.

5.3 Results

A cohort of 128 patients with varying diastolic health were studied, including a subset of 46 patients with normal filling classified based on an E/E' (ratio of peak transmitral inflow velocity to mitral annulus velocity) value of <8 [27]. Analysis of patient CMM data provided quantitative information for three characteristic events during diastole and the respective time at which they occurred. First, the "deceleration point time" is the time of the most statistically significant change (deceleration) of the early filing wave propagation velocity as shown in Figure1A by the change in the slope of the Vp (green line). The "peak IVPD time" corresponds to the instant during diastole at which the intra-ventricular pressure difference as calculated from the CMM data reaches a peak value (Figure 5.1C, dashed). Finally, the "onset of zero pressure difference time" corresponds to the time when the relative pressure along the scanline first falls to zero, eliminating the favorable pressure difference within the ventricle driving early filling (Figure 5.1C, solid). Figure1B illustrates the succession of these events.

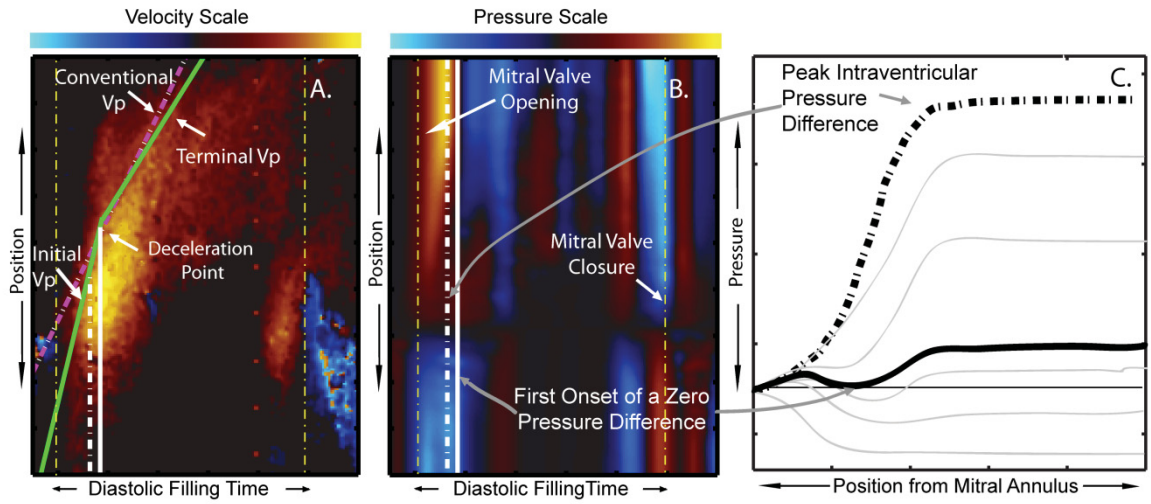

Figure 5.1: Representative CMM Data A.) Color M-mode Echocardiogram of a single diastolic period displaying initial and terminal velocities before and after the deceleration point. B.) Corresponding IVPD spatiotemporal distribution C.) Spatial pressure contours along the length of the left ventricle shown with progressing time from top to bottom. IVPD at the time of peak early diastolic mitral to apical pressure difference (dashed black) and the time of the onset of a zero pressure difference within the LV (solid black).

The nondimensional time at which the onset of a zero pressure difference occurred and the deceleration point occurred was calculated from the CMM data as shown in equation 5.2,

$$\text{Nondimensional Time} = \frac{U_{Mean} t}{D} \qquad 5.2$$

where t is the time of the zero pressure difference or deceleration point time referenced from the start of the early filling wave. The nondimensional time was used, as opposed to the actual time, to scale the time in order to compare among patients with different mitral valve diameters and mean inflow velocities.

Figure 5.2 displays the relationship of the CMM nondimensional deceleration point time with the nondimensional time of the onset of zero pressure difference within the LV. The solid line represents the linear regression, while the shaded area captures the one standard deviation band of the data points. The nondimensional time of the onset of zero pressure difference is positively correlated with the nondimensional deceleration point time (slope=0.90, r^2=0.27, $p<0.0001$). The nondimensional time of the

onset of zero pressure difference is nearly equivalent to the nondimensional deceleration point time as shown by a slope of 0.90 when the intercept is constrained to zero. This implies that the two times are associated with the same physical event. Baccani et al. also found a change in the early filling wave propagation velocity within a computational fluid dynamics study of filling for normal and dilated cardiomyopathy conditions. By performing a CMM type of analysis on the numerical data, they found two distinct propagation velocities and reported a decrease in the propagation velocity after the vortex ring detached from the mitral annulus [28]. The present study in combination with the work by Stewart et al. [1] provides support and validation, using clinical data, to Baccani et al. However Baccani et al. did not quantify the precise deceleration point time.

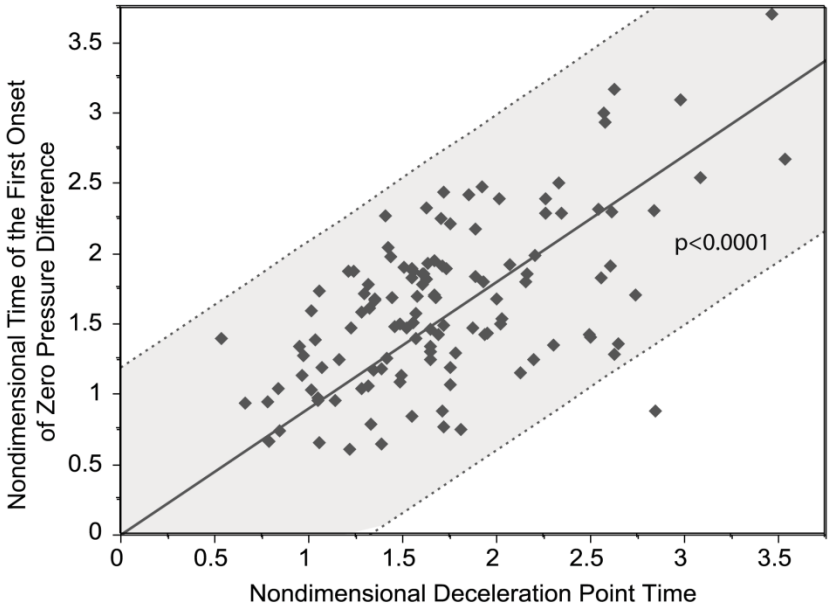

Figure 5.2: Nondimensional time of the onset of zero pressure difference calculated from the CMM versus the nondimensional deceleration point time. The centerline displays the linear fit and the shaded region represents the 95% confidence interval.

Synthesizing the results in Figure 5.2, with the work by Baccani et al. [28], reveals that the vortex ring pinch-off within the LV occurs at the time of the diastolic filling wave deceleration point, and that both events correspond to the loss of a favorable pressure difference within the LV. These observations further suggest that pinch-off occurs before the completion of early diastole (E-wave). An overview of this process is demonstrated in Figure 5.3. During the initial stage of diastole, a continuous jet issues

through the mitral valve that generates a rapid initial propagation velocity (Vp). At the time of the vortex ring pinch-off, the supply of momentum to the wave front (led by the vortex ring) in the flow is abruptly reduced, thus resulting in a sudden deceleration of the velocity wave as shown by the reduced terminal Vp slope.

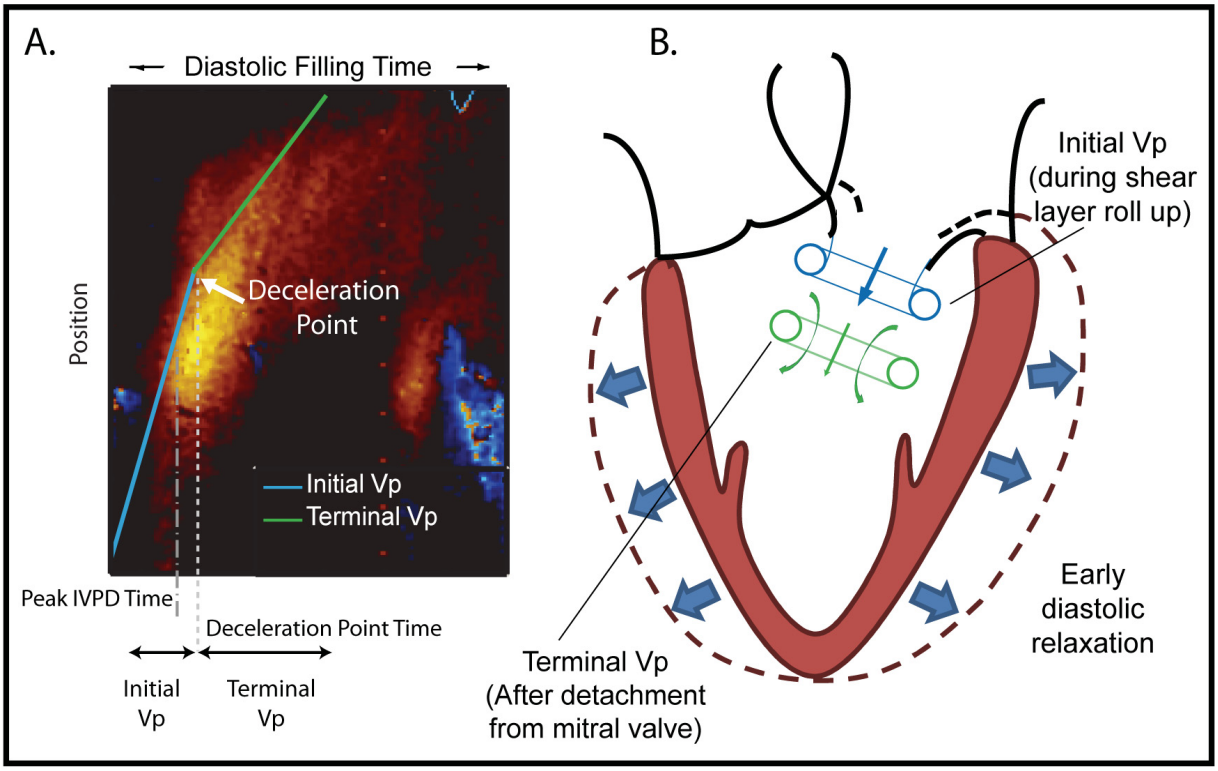

Figure 5.3: Hypothesized relationship between the early diastolic vortex ring pinch off and early diastolic filling dynamics as shown by the initial and terminal propagation velocities before and after the deceleration point time.

We calculated two formation times for the 46 patients with normal filling. First, based on our results indicating that the vortex ring pinch-off occurs at the deceleration point time, a FT was calculated using that time (FT_{dec}). Second, $FT_{E\text{-}wave}$ was calculated using the total early filling wave time following the assumption of Gharib et al.'s work [20]. In Figure 5.4A, we plot both FT_{dec} and $FT_{E\text{-}wave}$ against age (FT_{dec}: slope =-0.0034/year, r^2 =0.014, p<0.43; $FT_{E\text{-}wave}$: slope =-0.037/year, r^2=0.30, p<0.0001). $FT_{E\text{-}wave}$ displays a very similar inverse relationship to that presented by Gharib et al. [20], with the lower and upper quartile values of the FT distribution at 3.9 and 5.4. The slope of the $FT_{E\text{-}wave}$ versus age relationship for our normal patient cohort was -0.037/year versus a slope of approximately -0.031/year for

Gharib et al.'s patient cohort that was primarily composed of normal filling patients. As such, our results corroborate their measurements. However, FT_{dec} (blue diamonds) which we showed better represents the vortex ring pinch-off time, as opposed to $FT_{E\text{-}wave}$ calculated using the duration of early diastole, shows that the vortex ring formation time does not vary with age (slope =-0.0034/year, r^2 =0.014, p = 0.043), and has a mean value of 1.65 for healthy patients.

Early filling IVPD provides an independent measure of the strength of early diastolic suction and allows delineation between healthy and diseased patients as well as stage of diastolic dysfunction [23]. In Figure 5.4B we show the same formation time scales as above, but for 128 patients with varying diastolic function (including the 46 normals), as represented by the variation of the IVPD on the x-axis. The $FT_{E\text{-}wave}$ displays an inverse relationship with the early filling wave peak IVPD (slope =-0.41/mmHg, r^2 =0.14, $p<0.0001$). Thus the nondimensional duration of the early diastolic filling wave is changing with decreasing peak IVPD values, indicating decreased diastolic function. In both Figure 5.4A and B the $FT_{E\text{-}wave}$ value decreases as the heart is compromised by age or disease, as suggested by Gharib et al. [20], although in their data they had a very limited number of diseased subjects (approximately 7). Work by Ghosh et al. [29] also showed that $FT_{E\text{-}wave}$ decreased with diastolic dysfunction therefore indicating variations in LV stiffness, viscoelasticity, and load. This clearly implies that the LV and its operation are adapting with the progression of diastolic impairment. However, FT_{dec} remains nearly invariant as a function of early diastolic IVPD and the deceleration point occurs at an approximate nondimensional time of 1.7 regardless of the severity of diastolic impairment. This value is essentially unchanged compared to the healthy patients shown in Figure 5.4A.

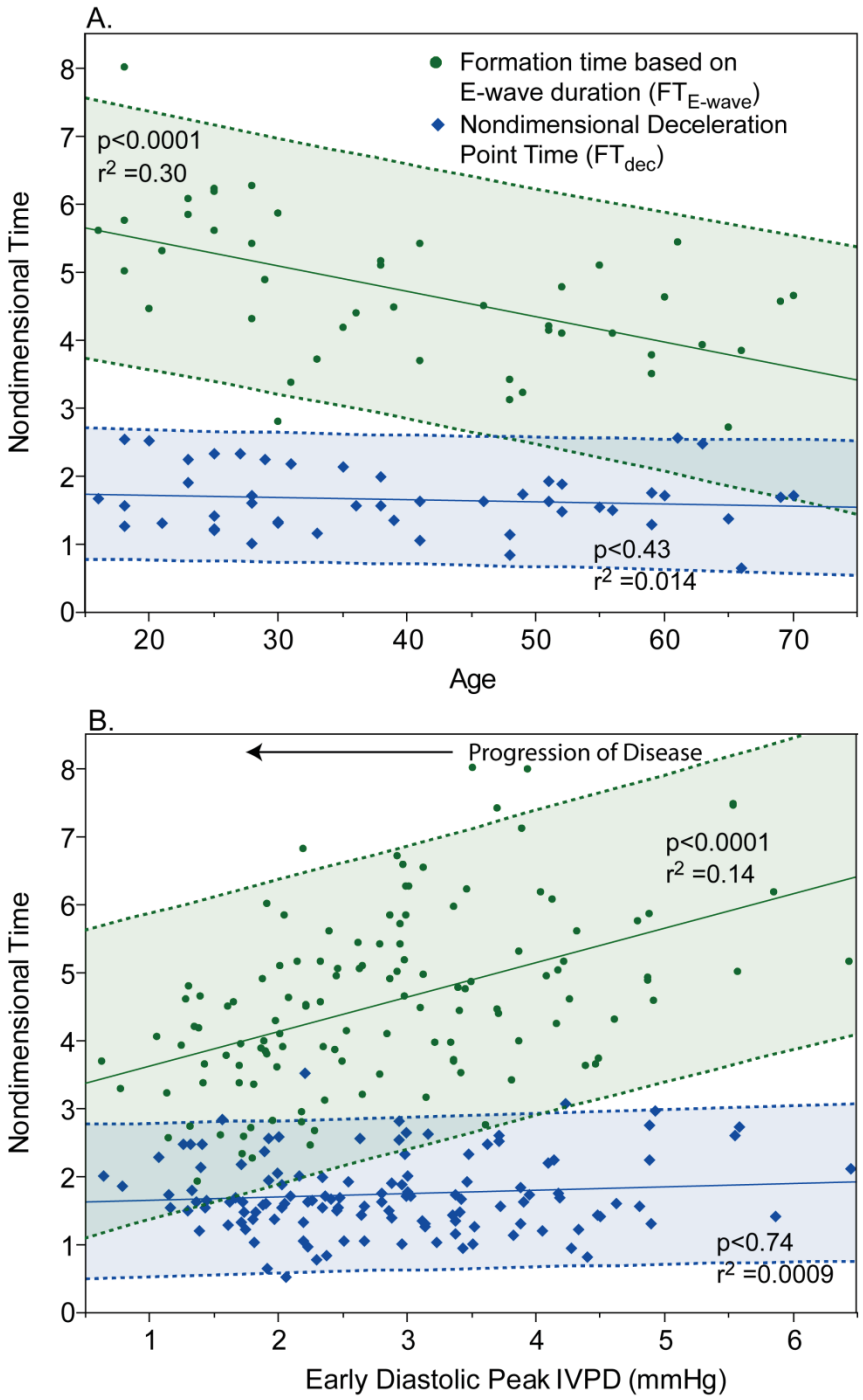

Figure 5.4: Formation time versus A.) age in years for 46 healthy patients as classified by E/E' < 8, B.) Early diastolic peak IVPD in mmHg for 128 patients with varying diastolic health. The centerline displays the linear fit and the shaded region represents the 95% confidence interval.

5.4 Discussion

The results presented in this study show that the vortex ring pinch-off corresponds to a decrease in the early filling propagation velocity and to the simultaneous onset of the loss of a favorable pressure difference along the vortex ring centerline (Figure 5.2). These findings, in combination with the results by by Baccani et al. [28] displaying the relationship between a decrease in the filling wave velocity with the vortex ring pinch-off, reveal for the first time that the vortex pinch-off is responsible for the deceleration point calculated within early diastolic filling. Moreover, both events occur simultaneously with the first onset of a zero pressure difference within the LV.

The nondimensional early filling duration time (FTE-wave) was shown to vary with age and peak IVPD, specifically the E-wave FT decreased as the heart was compromised by age or disease. These results are in agreement with previous work by Gharib et al. [20] and Ghosh et al. [29] and suggest that LV remodeling is occurring [5]. However, their FT calculation based on the early diastolic filling wave duration assumes that the vortex ring does not pinch-off until the end of early diastole. In this study, we showed that the vortex ring pinch-off occurs at the deceleration point time before the completion of early diastole. Consistent with this, we calculated FTdec, and we discovered that it remains unaffected by age or diastolic impairment, with a mean of approximately 1.7. This value is much lower than the previously reported formation time, of approximately 4, reported for vortex rings formed using a piston cylinder configuration in semi-infinite domains. Changes in the inflow velocity profile, orifice geometry, and downstream domain over time will affect the vortex ring generation and therefore alter the formation time, in this case decreasing its value.

In conclusion, this study is the first to demonstrate that the nondimensional vortex ring pinch-off time does not vary with age or diastolic dysfunction condition. In contrast with the previously hypothesized concept that variations in vortex ring dynamics may reflect the decline of diastolic function [20], our results suggest that vortex ring formation beyond the mitral valve remains invariant to pathophysiological changes associated with diastolic dysfunction. Previous work on left ventricular vortex formation time assumed that the vortex ring does not pinch-off until the end of the early diastolic filling wave. By using the total early filling wave duration time to calculated the vortex formation time, previous researchers have reported decreasing formation time values which actually correspond to variations within the early diastolic filling wave duration due to changes in left ventricular stiffness and relaxation. This study is the first to calculate the left ventricular vortex formation time by accounting for the time of vortex ring pinch-off as calculated by the deceleration point time. The formation time based on the deceleration point time results in a formation time which is invariant to pathophysiological changes associated with diastolic dysfunction. This result implies that there may remain a timescale for the

optimum left ventricular filling regardless of diastolic function as hypothesized by Gharib et al. [21]. These findings enhance our understanding of early diastolic physics, potentially leading to improved diagnostic techniques [17, 20, 28, 30].

5.5 Acknowledgements

This material is based upon work supported under a National Science Foundation Graduate Research Fellowship and National Science Foundation Grant No. 0547434. We also acknowledge the Wake Forest Translational Science Institute for their financial support.

5.6 References

1. Stewart, K.C., R. Kumar, J.J. Charonko, T. Ohara, P.P. Vlachos, and W.C. Little, *Evaluation of LV Diastolic Function From Color M-Mode Echocardiography.* JACC Cardiovascular Imaging, 2011. **4**(1): p. 37.
2. Quinones, M.A., *Assessment of diastolic function.* Progress in Cardiovascular Diseases, 2005. **47**(5): p. 340-355.
3. Asada-Kamiguchi, J., M. Jones, N.L. Greenberg, Z.B. Popovic, H. Tsujino, A.D. Zetts, J.X. Qin, M.J. Garcia, J.D. Thomas, and T. Shiota, *Intraventricular pressure gradients in left ventricular aneurysms determined by color M-mode Doppler method: An animal study.* Journal of the American Society of Echocardiography, 2006. **19**(9): p. 1112-1118.
4. Sessoms, M.W., J. Lisauskas, and S.J. Kovacs, *The left ventricular color M-mode Doppler flow propagation velocity V-p: In vivo comparison of alternative methods including physiologic implications.* Journal of the American Society of Echocardiography, 2002. **15**(4): p. 339-348.
5. Cohn, J.N., R. Ferrari, and N. Sharpe, *Cardiac remodeling--concepts and clinical implications: a consensus paper from an international forum on cardiac remodeling* 1.* Journal of the American College of Cardiology, 2000. **35**(3): p. 569-582.
6. Maron, B.J. and A. Pelliccia, *The heart of trained athletes: cardiac remodeling and the risks of sports, including sudden death.* Circulation, 2006. **114**(15): p. 1633.
7. Courtois, M., S.J. Kovacs Jr, and P. Ludbrook, *Transmitral pressure-flow velocity relation. Importance of regional pressure gradients in the left ventricle during diastole.* Circulation, 1988. **78**(3): p. 661.
8. Little, W.C., *Diastolic dysfunction beyond distensibility - Adverse effects of ventricular dilatation.* Circulation, 2005. **112**(19): p. 2888-2890.
9. Grewal, J., R. McCully, G. Kane, C. Lam, and P. Pellikka, *Left ventricular function and exercise capacity.* JAMA, 2009. **301**(3): p. 286.
10. Cheng, C.P., T. Noda, T. Nozawa, and W.C. Little, *Effect of heart failure on the mechanism of exercise-induced augmentation of mitral valve flow.* Circulation Research, 1993. **72**(4): p. 795.
11. Rovner, A., N.L. Greenberg, J.D. Thomas, and M.J. Garcia, *Relationship of diastolic intraventricular pressure gradients and aerobic capacity in patients with diastolic heart failure.* American Journal of Physiology-Heart and Circulatory Physiology, 2005. **289**(5): p. H2081-H2088.
12. Herbots, L., B. Lopez, A. Gonzalez, R.H. Fagard, and J. Diez, *Prevalence of Left Ventricular Diastolic Dysfunction in a General Population.* Circulation, 2009. **2**(2): p. 105-112.
13. Paulus, W.J., C. Tschope, J.E. Sanderson, C. Rusconi, F.A. Flachskampf, F.E. Rademakers, P. Marino, O.A. Smiseth, G. De Keulenaer, A.F. Leite-Moreira, A. Borbely, I. Edes, M.L. Handoko, S. Heymans, N. Pezzali, B. Pieske, K. Dickstein, A.G. Fraser, and D.L. Brutsaert, *How to diagnose diastolic heart failure: a consensus statement on the diagnosis of heart failure with normal left ventricular ejection fraction by the Heart Failure and Echocardiography Associations of the European Society of Cardiology.* European Heart Journal, 2007. **28**(20): p. 2539-2550.
14. Kilner, P.J., G.Z. Yang, A.J. Wilkes, R.H. Mohiaddin, D.N. Firmin, and M.H. Yacoub, *Asymmetric redirection of flow through the heart.* Nature, 2000. **404**(6779): p. 759-761.
15. Baccani, B., F. Domenichini, and G. Pedrizzetti, *Vortex dynamics in a model left ventricle during filling.* European Journal of Mechanics B-Fluids, 2002. **21**(5): p. 527-543.
16. Domenichini, F., G. Querzoli, A. Cenedese, and G. Pedrizzetti, *Combined experimental and numerical analysis of the flow structure into the left ventricle.* Journal of Biomechanics, 2007. **40**(9): p. 1988-1994.
17. Ishizu, T., Y. Seo, T. Ishimitsu, K. Obara, N. Moriyama, S. Kawano, S. Watanabe, and I. Yamaguchi, *The wake of a large vortex is associated with intraventricular filling delay in impaired left ventricles with a pseudonormalized transmitral flow pattern.* Echocardiography, 2006. **23**(5): p. 369-375.

18. Kheradvar, A., H. Houle, G. Pedrizzetti, G. Tonti, T. Belcik, M. Ashraf, J.R. Lindner, M. Gharib, and D. Sahn, *Echocardiographic Particle Image Velocimetry: A Novel Technique for Quantification of Left Ventricular Blood Vorticity Pattern.* Journal of the American Society of Echocardiography, 2010. **23**(1): p. 86-94.
19. Pedrizzetti, G. and F. Domenichini, *Nature optimizes the swirling flow in the human left ventricle.* Physical review letters, 2005. **95**(10): p. 108101.
20. Gharib, M., E. Rambod, A. Kheradvar, D.J. Sahn, and J.O. Dabiri, *Optimal vortex formation as an index of cardiac health.* Proceedings of the National Academy of Sciences of the United States of America, 2006. **103**(16): p. 6305-6308.
21. Gharib, M., E. Rambod, and K. Shariff, *A universal time scale for vortex ring formation.* Journal of Fluid Mechanics, 1998. **360**: p. 121-140.
22. Brun, P., C. Tribouilloy, A.M. Duval, L. Iserin, A. Meguira, G. Pelle, and J.L. Duboisrande, *Left-Ventricular Flow Propagation During Early Filling is Related to Wall Relaxation - A Color M-Mode Doppler Analaysis.* Journal of the American College of Cardiology, 1992. **20**(2): p. 420-432.
23. Yotti, R., J. Bermejo, J.C. Antoranz, M.M. Desco, C. Cortina, J.L. Rojo-Alvarez, C. Allue, L. Martin, M. Moreno, J.A. Serrano, R. Munoz, and M.A. Garcia-Fernandez, *A noninvasive method for assessing impaired diastolic suction in patients with dilated cardiomyopathy.* Circulation, 2005. **112**(19): p. 2921-2929.
24. Greenberg, N.L., S. Krucinski, J.D. Thomas, and I. Ieee. *Significance of color Doppler M-mode scanline orientation in the non-invasive assessment of intraventricular pressure gradients*. In *24th Annual Computers in Cardiology Conference*. 1997. Lund, Sweden.
25. Thomas, J.D. and Z.B. Popovic, *Intraventricular pressure differences - A new window into cardiac function.* Circulation, 2005. **112**(12): p. 1684-1686.
26. De Boeck, B.W.L., J.K. Oh, P.M. Vandervoort, J.A. Vierendeels, R. van der Aa, and M.J.M. Cramer, *Colour M-mode velocity propagation: a glance at intra-ventricular pressure gradients and early diastolic ventricular performance.* European Journal of Heart Failure, 2005. **7**(1): p. 19-28.
27. Ommen, S., R. Nishimura, C. Appleton, F. Miller, J. Oh, M. Redfield, and A. Tajik, *Clinical utility of Doppler echocardiography and tissue Doppler imaging in the estimation of left ventricular filling pressures: a comparative simultaneous Doppler-catheterization study.* Circulation, 2000. **102**(15): p. 1788.
28. Baccani, B., F. Domenichini, G. Pedrizzetti, and G. Tonti, *Fluid dynamics of the left ventricular filling in dilated cardiomyopathy.* Journal of Biomechanics, 2002. **35**(5): p. 665-671.
29. Ghosh, E., L. Shmuylovich, and S.J. Kovács, *Vortex formation time-to-left ventricular early rapid filling relation: model-based prediction with echocardiographic validation.* Journal of Applied Physiology, 2010. **109**(6): p. 1812.
30. Kheradvar, A. and M. Gharib, *On Mitral Valve Dynamics and its Connection to Early Diastolic Flow.* Annals of Biomedical Engineering, 2009. **37**(1): p. 1-13.

5.7 Methods

5.7.1 Echocardiography Acquisition

Echo-Doppler examinations were completed using an iE33 ultrasound imaging system with a multiple frequency transducer (Philips Medical Systems, Andover, MA). Standard 2-dimensional images were obtained in the parasternal long and short axes, and in the apical 4- and 2- chamber views. Pulsed-wave Doppler tracings of mitral valve inflow were recorded at the leaflet tips. Color M-mode ultrasound was obtained with a sweep speed of 100 mm/sec with a scale that optimized visualization of the isovelocity color contour as judged by the recording sonographer. Recordings of the mitral annular velocity were also obtained on the septal and lateral walls from an apical 4-chamber view. Left ventricular volumes and Doppler tracings were analyzed using a digital echocardiography workstation as previously described [1, 2].

5.7.2 Statistical Analysis

JMP Statistical Discovery Software (SAS Institute Inc., Cary, NC) was used for all statistical analysis. All calculated properties were averaged for each category and are expressed as mean ± 1 standard deviation. We analyzed statistical significance among groups using a one-way analysis of variance (ANOVA) and the Tukey-Kramer honest significant difference test.

5.7.3 Description of the Automated CMM Analysis Algorithm

An automated algorithm was developed to analyze CMM data and to calculate the pressure distributions within the LV. Details on the CMM analysis algorithm can be found in the methodology section and supplementary material in previous work by Stewart et al. [3].

5.7.4 Mitral Inflow and Mitral Annulus Doppler Analysis

In addition to the CMM echocardiography data for each patient within the study, the transmitral Doppler and mitral annulus Doppler data was acquired. These data provide independent measurements of the mitral inflow velocity and the mitral annulus velocity throughout diastole. With this independent information, a control volume analysis of the mitral annulus region was completed to calculate the relative pressure driving early diastolic filling using the momentum equation. Equations5.3 and 5.4 display the momentum equation for a deformable control volume around the mitral annulus as shown in Figure 5.5,

$$\sum Forces = \frac{\partial}{\partial t}\left(\int_{cv} U\rho dV\right) + \left(\int_{cs} U\rho\left(W \cdot n_1\right) dA_1\right), \tag{5.3}$$

$$\int_{cs}(-P_1)n_1 dA_1 + \int_{cs} P_2 n_2 dA_2 = \rho \frac{\partial(-U_J)}{\partial t} V + \left(\int_{cs}(-U_J)\rho\left(-(U_J - U_A)\cdot n\right) dA_1 \right). \quad 5.4$$

For this analysis we assumed that the flow is inertia dominant due to the high Reynolds number, therefore the shear stress contribution to the momentum equation was neglected. In these equations, U_J is the mitral inflow jet velocity, U_A is the mitral annulus velocity, W is the relative velocity of the deformable wall (U_J-U_A), ρ is the density, P_1 and P_2 are the pressures acting on the areas A_1 and A_2, and V is volume.

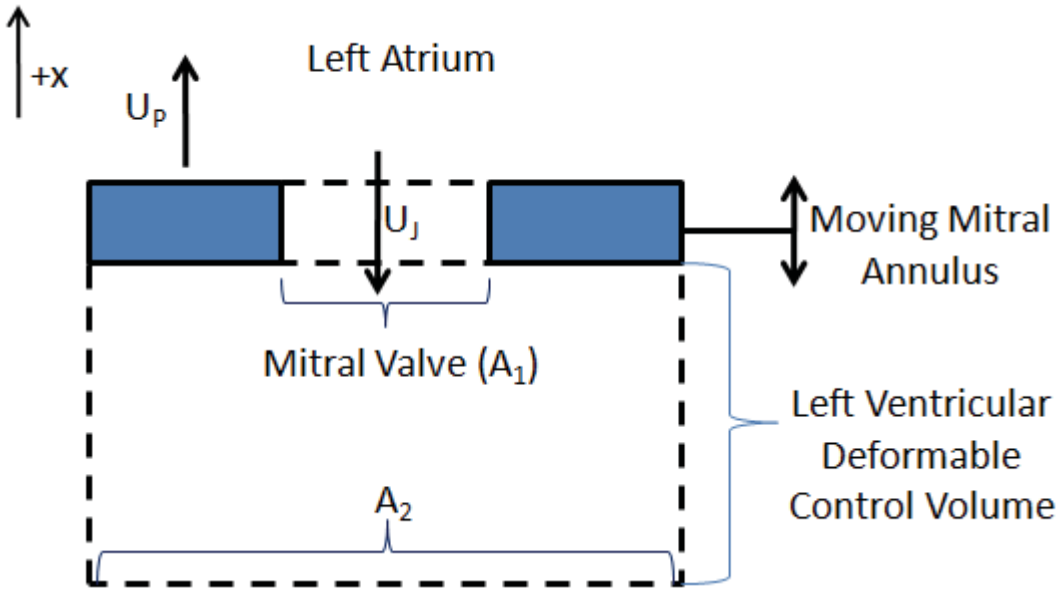

Figure 5.5: Deformable Control Volume analysis around the mitral annulus and left ventricle.

The relative pressure within the LV with respect to the pressure at the mitral annulus location was calculated, therefore P_1, the pressure at A_1 through the mitral annulus was set to zero in equation 5.5,

$$0 - P_2 A_2 = -\rho \frac{\partial U_J}{\partial t} V - \rho U_J \left(U_J - U_A\right) A_1, \quad 5.5$$

and we solve for the pressure within the ventricle in equation 5.6,

$$-P_2 = \frac{1}{A_2}\rho \frac{\partial U_J}{\partial t} V - \rho U_J (U_J - U_A) \frac{A_1}{A_2}. \quad 5.6$$

For this analysis we assumed the control volume deformed with mitral annulus motion. To determine the volume and height of the control volume with respect to time we introduce equations 5.7,

$$V(t) = A_2 h(t) = \int U_A A_1 dt, \tag{5.7}$$

and 5.8 where V(t) is the changing volume in time and h(t) is the varying height or length of the LV,

$$h(t) = \frac{A_1}{A_2} \int U_A dt. \tag{5.8}$$

After incorporating equations 5.7 and 5.8 into equation 5.6, the result is an equation for the pressure driving the early diastolic filling, as shown in equation 5.9

$$-P_2 = \rho \frac{\partial U_J}{\partial t} \frac{A_1}{A_2} (h_0 + \int_0^t U_A dt) - \rho U_J \left((U_J - U_A) \right) \frac{A_1}{A_2}. \tag{5.9}$$

The areas used for the mitral annulus area, A_1, and the LV area, A_2 are shown in equation 5.10 where D_{mv} is the mitral valve diameter as measured by the 4-chamber echocardiography image at peak diastolic inflow. The LV area was assumed to be twice the size of the mitral valve area,

$$A_1 = \frac{\pi D_{MV}^2}{4}, \qquad A_2 = 2A_1. \tag{5.10}$$

This analysis resulted in relative pressure waveforms over the duration of the cardiac cycle from the EKG signal T-wave to T-wave. For each relative pressure waveform there was a peak corresponding to the E-wave diastolic filling.

The pressure within the LV during early diastole was determined independently by analyzing the mitral inflow Doppler and mitral annulus tissue Doppler data. The deformable control volume (CV) analysis described above was used in combination with the time history of the Doppler velocities to calculate the peak IVPD within the LV driving early diastolic flow (refer to the supplemental methods section). The time of peak IVPD as calculated by the CV analysis, corresponds to the time of peak recoil force on the mitral annulus as calculated in the work of Kheradvar et al. [4, 5], which they experimentally showed occurs just before vortex ring pinch-off. Figure 5.6A shows the correlation between the nondimensional time of peak IVPD calculated from the CMM analysis and the corresponding

nondimensional time of peak IVPD calculated from the CV analysis. The two approaches for estimating the peak IVPD correlate with a slope of 0.92 (r^2=0.37 and p<0.0001). This result illustrates that the maximum recoil force on the mitral annulus corresponds to the development of the CMM estimated peak IVPD and hence it is physically consistent with the development of the maximum suction in the LV, which precedes pinch-off.

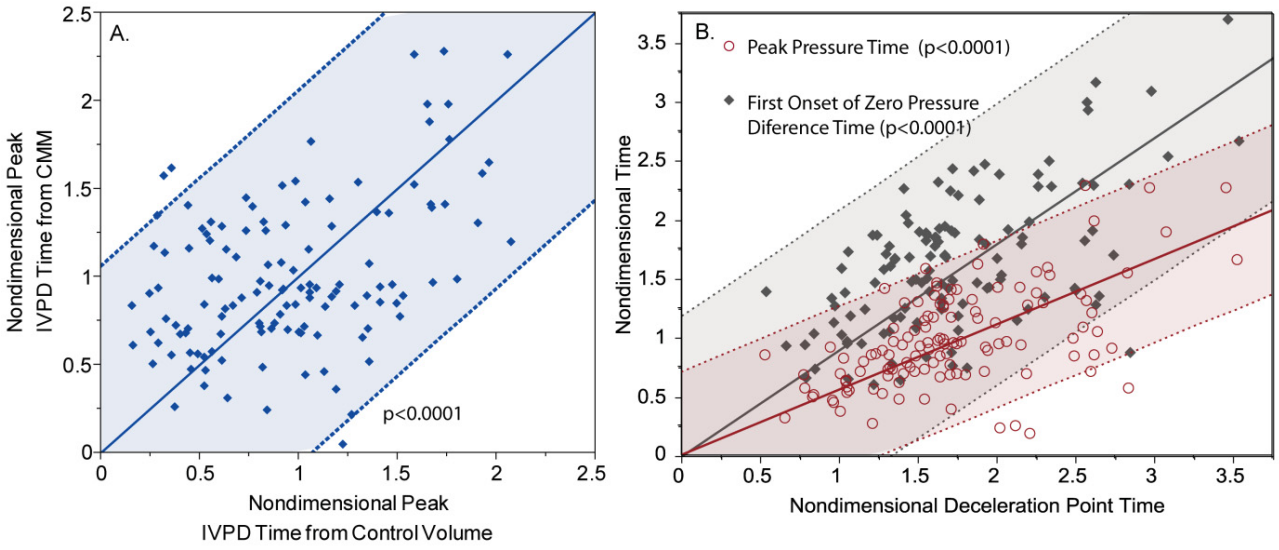

Figure 5.6: Nondimensional Time Plots A.) Nondimensional peak pressure time from CMM versus the nondimensional peak pressure time from the control volume analysis. B.) Nondimensional peak pressure time calculated from the CMM analysis and the nondimensional time of a zero pressure difference calculated from the CMM versus the nondimensional deceleration point time. The centerline displays the linear fit and the shaded region represents the 95% confidence interval.

Figure 5.6B displays the relationship of the CMM nondimensional deceleration point time (horizontal axis) with the CMM nondimensional peak IVPD time and the CMM nondimensional time of the first onset of a zero pressure difference (vertical axis, circle and diamond respectively). The solid lines represent the corresponding linear regressions, while the shaded areas capture the one standard deviation band of the data points. The CMM nondimensional peak IVPD time corresponds to the time of peak recoil force on the mitral annulus as in Kheradvar et al.'s work [4, 5]. Both the peak pressure time and the zero pressure difference time correlate well with the nondimensional deceleration point time (peak pressure time: slope=0.55, r^2=0.31, p<0.0001; zero pressure difference time: slope=0.90, r^2=0.27,

p<0.0001). The smaller slope of the regression line for the peak pressure time confirms that the time of the peak recoil force always precedes the deceleration point time. Figure 5.5B also displays that the nondimensional time of the onset of a zero pressure difference is nearly equivalent to the nondimensional deceleration point time as shown by a slope of 0.90 when the intercept is constrained to zero. This implies that the two times are associated with the same physical event. Baccani et al. performed a computational fluid dynamics study of filling for normal and dilated cardiomyopathy conditions. By performing a CMM type of analysis on the numerical data, they found two distinct propagation velocities and reported a decrease in the propagation velocity after the vortex ring detached from the mitral annulus [6]. The present study in combination with the work by Stewart et al. [3] provides support and validation, using clinical data, to Baccani et al. However they did not quantify the precise deceleration point time.

5.8 Patient Population

A total of 128 patients were used in this study and were selected from routine comprehensive echocardiography and Doppler evaluations at Wake Forest University Baptist Medical Center. Vp was calculated for each patient during regular clinical treatment according to the American Society of Echocardiography guidelines [7]. This study was conducted according to protocols approved by the Virginia Tech and Wake Forest University Internal Review Boards.

The patient population was selected using the inclusion criteria of no pre-existing cardiac conditions and good quality echocardiography scans. Previous work including these patients been published by Brucks et al. [8].

Table 5.1: Left Ventricular Echocardiography-Doppler and Patient Specific parameters. Values represent mean value ± 1 standard deviation (range).

Age	53.11±18.71 (16-91)
Ejection Fraction (EF)	51.17±13.77% (12.82-72.63)
E-wave Mitral Inflow, cm/s	88.57±20.56 (49-134)
A-wave Mitral Inflow	63.58±24.94 (7.18-143)
E/A*	1.57±0.80 (0.50-5.50)
E/e'†	11.33±5.92 (4.15-38.79)
IVPD‡, mmHg	2.86±1.22 (0.31-6.45)

* E wave to A wave transmitral velocity ratio

† E wave transmitral to E wave mitral annulus velocity ratio

‡ Intraventricular Pressure Difference

5.8.1 References

1. Gandhi, S.K., J.C. Powers, A. Nomeir, K. Fowle, D.W. Kitzman, K.M. Rankin, and W.C. Little, *The pathogenesis of acute pulmonary edema associated with hypertension.* New England Journal of Medicine, 2001. **344**(1): p. 17-22.
2. Warner, J.G., D.C. Metzger, D.W. Kitzman, D.J. Wesley, and W.C. Little, *Losartan improves exercise tolerance in patients with diastolic dysfunction and a hypertensive response to exercise.* Journal of the American College of Cardiology, 1999. **33**(6): p. 1567-1572.
3. Stewart, K.C., R. Kumar, J.J. Charonko, T. Ohara, P.P. Vlachos, and W.C. Little, *Evaluation of LV Diastolic Function From Color M-Mode Echocardiography.* JACC Cardiovascular Imaging, 2011. **4**(1): p. 37.
4. Kheradvar, A. and M. Gharib, *Influence of ventricular pressure drop on mitral annulus dynamics through the process of vortex ring formation.* Annals of Biomedical Engineering, 2007. **35**(12): p. 2050-2064.
5. Kheradvar, A., M. Milano, and M. Gharib, *Correlation between vortex ring formation and mitral annulus dynamics during ventricular rapid filling.* Asaio Journal, 2007. **53**(1): p. 8-16.
6. Baccani, B., F. Domenichini, G. Pedrizzetti, and G. Tonti, *Fluid dynamics of the left ventricular filling in dilated cardiomyopathy.* Journal of Biomechanics, 2002. **35**(5): p. 665-671.
7. Nagueh, S.F., C.P. Appleton, T.C. Gillebert, P.N. Marino, J.K. Oh, O.A. Smiseth, A.D. Waggoner, F.A. Flachskampf, P.A. Pellikka, A. Evangelisa, and E. Amer Soc, *Recommendations for the Evaluation of Left Ventricular Diastolic Function by Echocardiography.* European Journal of Echocardiography, 2009. **10**(2): p. 165-193.
8. Brucks, S., W.C. Little, T. Chao, D.W. Kitzman, D. Wesley-Farrington, S. Gandhi, and Z.K. Shihabi, *Contribution of left ventricular diastolic dysfunction to heart failure regardless of election fraction.* American Journal of Cardiology, 2005. **95**(5): p. 603-606.

6 New Method of Evaluating Left Ventricular Diastolic Function from Color M-mode Echocardiography

Kelley C. Stewart, MS[1], Rahul Kumar, MD[2], John J. Charonko, PhD[1], Takahiro Ohara, MD, PhD[2], Pavlos P. Vlachos, PhD[1], William C. Little, MD, FACC [2]

1Department of Mechanical Engineering and School of Biomedical Engineering and Sciences
Virginia Tech, Blacksburg, VA
2Cardiology Section, Wake Forest University School of Medicine
Winston-Salem, NC

Kelley C. Stewart, Rahul Kumar, M.D., John Charonko, Pavlos P. Vlachos, Ph.D., and William C. Little, M.D., New Method of Evaluating Left Ventricular Diastolic Function from Color M-mode Echocardiography. 4:37-46, doi:10.1016/j.jcmg.2010.09.020 (2011).[1]

6.1 Abstract

Background: Diastolic function can be evaluated from color M-mode (CMM) echocardiography by measuring the early diastolic flow propagation velocity (Vp) from the slope of a linear approximation of an isovelocity contour. However, this method has limitations and may not accurately represent diastolic filling.

Methods and Results: We used an automated objective analysis of CMM echocardiograms from 125 patients with varying diastolic function to quantify left ventricular filling velocities. Early diastolic flow propagation had a rapid initial velocity that abruptly decelerated to a slower terminal velocity. Compared to normal filling, severe diastolic dysfunction had a lower initial velocity (53 ± 21 vs 87 ± 29 cm/sec, $p<0.001$), and the deceleration point occurred closer to the mitral annulus (2.4 ± 0.6 cm vs 3.1 ± 0.7 cm, $p<0.05$). The product of the initial velocity and the distance to the deceleration point, indicating the strength of the early filling (Vs), was progressively reduced with diastolic dysfunction. In a separate validation cohort of 160 patients, Vs better recognized diastolic dysfunction (classified by reduced diastolic intraventricular pressure gradient, elevated pulmonary capillary wedge pressure, or elevated B-type natriuretic peptide) than Vp.

Conclusions: Early diastolic flow propagation occurs with an initial rapid velocity that abruptly decelerates to a terminal velocity. With diastolic dysfunction, the initial velocity is slower and the

[1] Reprinted from the Journal of the American College of Cardiology: Imaging, volume 4, issue 1, Kelley C. Stewart, Rahul Kumar, John J. Charonko, Takahiro Ohara, Pavlos P. Vlachos, and William C. Little, Evaluation of LV Diastolic Function From Color M-Mode Echocardiography, Pages 37-46, January 2011, with permission from Elsevier.

deceleration point occurs closer to the mitral annulus. A new parameter that combines these two effects (Vs) provides a more accurate assessment of diastolic function than Vp.

Key words: Diastole, echocardiography, heart failure, imaging

Abbreviations List

LV = left ventricular; CMM = color M-mode; Vp = propagation velocity; E = E-wave inflow velocity; HCM = hypertrophic cardiomyopathy; IVPD = intraventricular pressure difference; BNP = B-type natriuretic peptide; ROC = receiver operator characteristic; Vs = early filling strength; PCW = pulmonary capillary wedge

6.2 Introduction

Left ventricular (LV) diastolic function can be non-invasively evaluated from LV filling dynamics determined by Doppler echocardiography [1-3]. Color M-mode (CMM) echocardiography provides a spatio-temporal map of the velocities of the blood flow along the scan line from the mitral annulus to the LV apex [4, 5]. The current method of analyzing this data is to calculate the propagation velocity (Vp) of the inflow jet traveling toward the apex during early diastole [1-3, 5-11]. Vp is measured as the slope of a linear approximation of an isovelocity contour. Vp is reduced in patients with diastolic dysfunction, and the ratio of peak transmitral E-wave velocity (E) to Vp is elevated when left atrial pressure is increased [3, 12-16].

There are several potential limitations to the use of Vp as a measure of LV diastolic function. First, in many situations, the isovelocity contour may not be accurately described by a straight line [17-19]. Thus, assignment of a single slope (i.e., Vp) may not be accurate. Furthermore, Vp is subject to variation based on how the isovelocity contour is determined [1, 17, 20]. Finally, Vp has been found to be normal in patients with hypertrophic cardiomyopathy (HCM) who have diastolic dysfunction apparent by other methods [21].

Under normal circumstances, early diastolic filling results from a progressive pressure gradient from the left atrium [4, 22] that extends towards the LV apex. With diastolic dysfunction, the magnitude of the pressure gradient is reduced, and it does not extend as deeply into the left ventricle [9]. Thus, we hypothesized that with diastolic dysfunction, the initial Vp of the filling wave is reduced and that it would decelerate to a lower velocity prior to reaching the apex. In contrast, in normals, the initial velocity would be higher and deceleration would occur closer to the LV apex.

Accordingly, we evaluated early diastolic filling using CMM echocardiograms from 125 patients with a range of diastolic function. Consistent with our hypothesis, we found that the early diastolic flow velocities were not accurately described by a single slope. We used this information to develop a new

metric of early diastolic filling that more accurately recognized diastolic dysfunction. We then tested this new measure in a second cohort of 160 patients.

6.3 Methods

6.3.1 Echo-Doppler

Echo-Doppler examinations were completed using an iE33 ultrasound imaging system with a multiple frequency transducer (Philips Medical Systems, Andover, MA). Standard 2-dimensional images were obtained in the parasternal long and short axes and in the apical 4- and 2-chamber views. Pulsed-wave Doppler tracings of mitral valve inflow were recorded at the leaflet tips. CMM ultrasound was obtained in the apical long axis view with a sweep speed of 100 mm/sec with a scale that optimized visualization of the isovelocity color contour as judged by the recording sonographer. Recordings of the septal and lateral mitral annular velocities were averaged. LV volumes and Doppler tracings were analyzed using a digital echocardiography workstation as previously described [23, 24].

6.3.2 Brief Description of the Automated Algorithm

An automated data analysis algorithm was developed to examine the CMM echocardiograph images. Original CMM images were analyzed in MATLAB (The Mathworks, Natic, MA) using in-house developed image processing algorithms. The algorithm is used to crop a region of interest (Figure1B) and the velocity color scale region. With this information, a point-by-point velocity reconstruction is completed on the ROI (see the supplemental material for additional information).

The image was reconstructed using a de-aliasing technique similar to that used by Thomas et al. and Rovner et al. [25, 26] (Figure 6.1D). Through the use of image processing tools, the E-wave velocity field was reduced to a series of twenty-seven isovelocity contours evenly spaced between 45% and 55% of the peak E-wave transmitral velocity shown in Figure1E. The reconstructed velocity contours are shown in Figure1F with the 45% to 55% isovelocity contours shown from light to dark.

A de-aliasing technique similar to the techniques used by Thomas et al. and Rovner et al. [25, 26] was used to reconstruct the image shown in Figure 6.1D. Through the use of image processing tools, the E-wave velocity field was reduced to a series of twenty-seven isovelocity contours evenly spaced between 45% and 55% of the peak E-wave transmitral velocity shown in Figure 6.1E. The reconstructed velocity contours are shown in Figure 6.1F with the 45% to 55% isovelocity contours shown from light to dark.

6.3.3 Ensemble Contour Methodology

A smoothing spline was fit to the series of isovelocity contours and is referred to as the ensemble contour in the remaining analysis (see supplemental material for additional information).

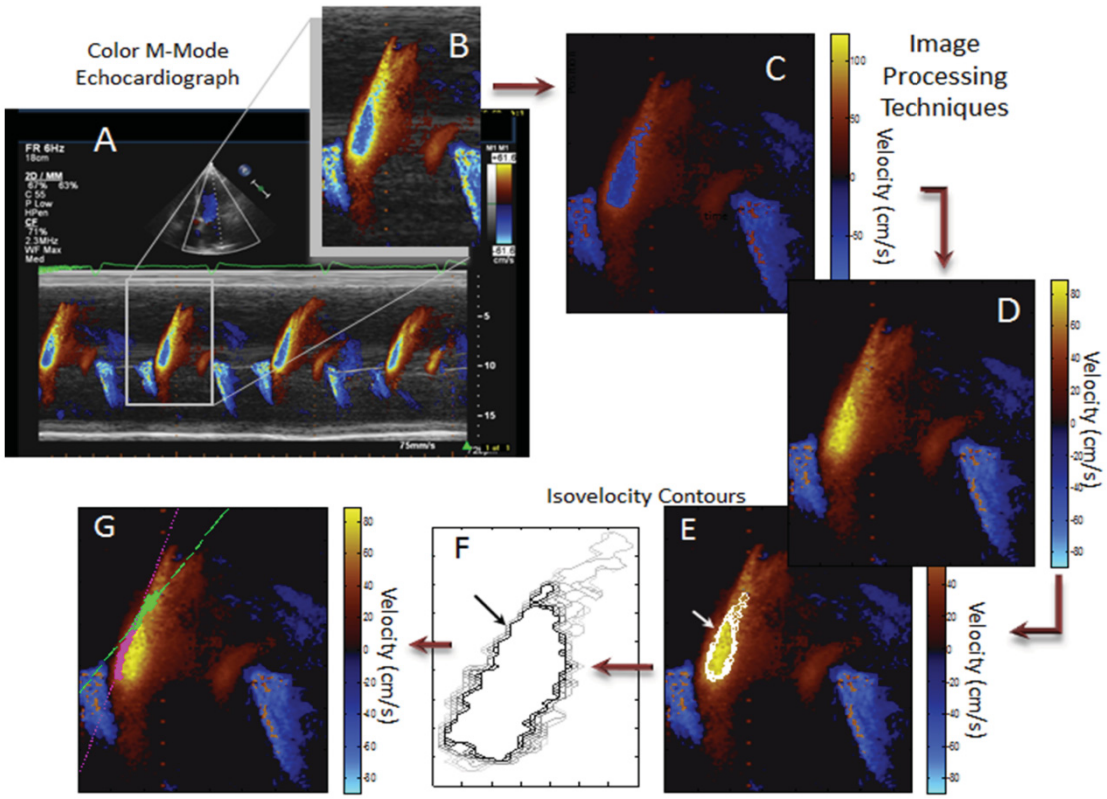

Figure 6.1: Method of analysis of a restrictive filling patient color M-mode echocardiograph. A: Original color M-mode image. B: Region of interest extracted from the color M-mode image containing a complete diastolic cycle. C: Region of interest after a point-by-point velocity reconstruction. D: Anti-aliased region of interest. E: Region of interest displaying the location of the series of isovelocity contours from 45% to 55% of the E wave peak transmitral velocity. F: Isovelocity contours shown from 45% to 55% of the peak E wave transmitral velocity from light to dark.

6.3.4 Change-Point Methodology

Previous observations of a change in slope or curvilinear isovelocity contour [17-19] are consistent with an abrupt deceleration of the LV filling wave. We used a statistical change-point analysis method [27, 28] on the derivative of the ensemble contour (Figures 2C and 2G) to objectively determine the deceleration point. The method is based on a cumulative sum of the difference between the value of interest (x_i) and the mean value ($\bar{x}$). Equation 6.1 displays the cumulative sum equation:

$$CumulativeSum_i = CumulativeSum_{i-1} + (x_i - \bar{x}). \quad 6.1$$

The waveform produced by the output of the cumulative sum equation was plotted to determine the significance of the change throughout the signal (Figures 2D and 2H). The peaks within this cumulative sum waveform were sorted according to their magnitude. The peak with the highest magnitude signifies the most statistically significant change and was labeled as the *"deceleration point."*

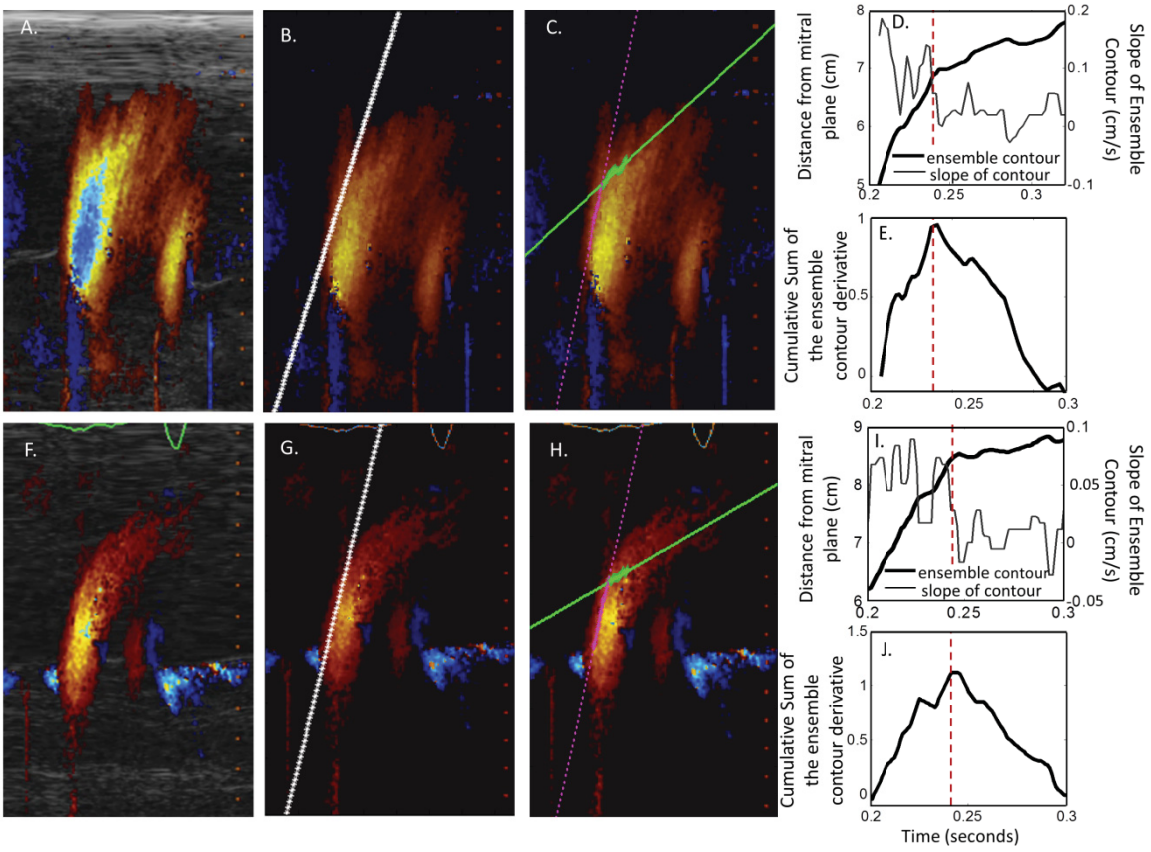

Figure 6.2: A and E: Color M-mode echocardiogram of a normal subject and a patient with a restrictive filling pattern. B and F: Dealiased region of interest showing the initial (pink) and terminal (green) propagation velocity with the deceleration point located at their intersection. C and G: Ensemble contour and calculated slopes of the ensemble contour. D and H: Cumulative sum plot calculated from the derivative of the ensemble contour values. The dotted line represents the deceleration point determined at the time of the peak cumulative sum.

6.3.5 Pressure Calculations

The one-dimensional incompressible Euler equation, shown in equation 6.2, where p is the pressure, ρ is constant blood density, and v is velocity, was used to calculate the relative pressures within the ROI from the reconstructed velocity field. The pressure at each point along a scan line was calculated relative to the position of the mitral annulus just prior to mitral valve opening calculating the line integral between them [9, 29],

$$\frac{\partial p}{\partial s} = -\rho\left(\frac{\partial v}{\partial t} + v\frac{\partial v}{\partial s}\right). \qquad 6.2$$

From the relative pressures, the peak diastolic intraventricular pressure difference (IVPD) from the left atrium to the LV apex was calculated similar to Greenberg et al. and Rovner et al. [26, 30]. This method has been validated by comparison to direct measurements with micromanometers [9, 25]. The IVPD provides a measure of the strength of LV diastolic suction. We used an IVPD of 2.2 mmHg as the lower limit of normal based on the observations of the IVPD in healthy volunteers by Yotti et al [9].

6.3.6 Early Filling Velocity Strength

We observed that early filling is characterized by a point at which the Vp abruptly decelerates (see below) indicating that a single straight line is not an accurate approximation for the Vp parameter. The ensemble contour was divided at the deceleration point into two segments, the initial propagation region and the terminal propagation region. A line was fit to the ensemble contour for each filling region to calculate the propagation velocities before (initial Vp) and after the deceleration point (Terminal Vp), as shown in Figure 6.2B and F as the two intersecting lines where the junction is the deceleration point.

We calculated the distance from the position of the mitral annulus just prior to the opening of the mitral valve to the deceleration point, L_i. The product of this distance and the initial Vp represents the strength of early filling (Vs),

$$V_s = \text{Initial Vp} * L_i. \qquad 6.3$$

6.3.7 Patient Population

Two independent groups of patients were used in this study: a development cohort consisting of 125 patients and a validation cohort consisting of 160 patients. These were selected from patients undergoing clinically-indicated comprehensive echocardiography and Doppler evaluation at the Wake Forest University Baptist Medical Center. The study was conducted according to protocols approved by the Virginia Tech and Wake Forest University Baptist Medical Center Institutional Review Boards.

Diastolic dysfunction stages were assigned based on the mitral valve inflow, tissue Doppler mitral annular velocities, and conventional Vp was measured according to the American Society of Echocardiography guidelines [3].

6.3.8 Development Cohort

The patients in the development cohort were selected to create five equally-sized categories. Due to the wide range of ages, the healthy filling category was divided into two categories, one group younger than thirty years old and the second group thirty years and older. The remaining three categories were composed of 25 patients with each of the three stages of diastolic dysfunction: delayed relaxation filling (stage 1), pseudonormal filling (stage 2), and restrictive filling (stage 3) (Table 1). Seventeen patients from the development cohort were randomly selected for the assessment of parameter reproducibility. The patients were analyzed three independent times by three different observers to assess the inter- and intra-observer variability.

Table 6.1: Clinical Characteristics of the Testing Cohort. Patients are classified based on clinically diagnosed diastolic dysfunction stage. Values represent mean ± one standard deviation.

Diastolic Dysfunction Stage	Number of Patients	Age (years)	E/A*	E/E' †	Ejection Fraction
0 – Healthy, age < 30 yrs	25	24.36±4.25	1.98±0.69	6.53±1.47	0.57±0.05
0 – Healthy, age > 30 yrs	25	47.36±14.33	1.54±0. 31	7.88±2.66	0.62±0.05
1 – Delayed Relaxation	25	68.32±9.62	0.79±0.11	13.00±4.22	0.57±0.13
2 – Pseudonormal	25	66.20±12.94	1.58±0.31	16.40±5.27	0.40±0.15
3 – Restrictive Filling	25	59.44±18.50	2.91±1.02	18.77±7.38	0.28±0.08

* E wave to A wave transmitral velocity ratio

† E wave transmitral to E wave mitral annulus velocity ratio

6.3.9 Validation Cohort

The patient population for the validation cohort consisted of 160 patients, including 10 patients with HCM (Table 2). It is important to note that development cohort CMM data included only good image quality scans, and that CMM images with merged E and A waves were not included. The validation cohort CMM selection criteria were less strict and patients with fair to poor image quality and merged E and A waves were included in the analysis. Other analysis of observations in some of the validation patient population has been previously published by Brucks et al. [31].

Table 6.2: Clinical Characteristics of the Validation Cohort.

a) Subset with IVPD measurement

n	Age, y	Gender, n (%)		EF<0.4, n (%)	Diastolic function, n (%)	
160	57±13	Male	91 (57)	29 (18)	Normal	52 (33)
		Female	68 (43)		Impaired relaxation	51 (32)
					Pseudonormal filling	26 (16)
					Restricted filling	24 (15)
					Not determined	7 (4)

b) Subset with BNP measurement

n	Age	Gender, n (%)		EF<0.4, n (%)	Diastolic function, n (%)	
117	58±14	Male	61 (52)	25 (21)	Normal	40 (34)
		Female	56 (48)		Impaired relaxation	43 (37)
					Pseudonormal filling	18 (15)
					Restricted filling	15 (13)
					Not determined	1 (0.9)

c) Subset with PCW Pressure measurement

	Age	Gender, n (%)		Period between echo and catheterization, hours	EF<0.4, n (%)	Diastolic Function, n (%)	
56	56±19	Male	37 (66)	20±15	14 (25)	Normal	20 (36)
		Female	18 (32)			Impaired relaxation	8 (14)
		Not Determined	1 (0.02)			Pseudonormal filling	9 (16)
						Restricted filling	13 (23)
						Not determined	6 (11)

IVPD = intraventricular pressure difference; EF=ejection fraction; HCM = hypertrophic cardiomyopathy; BNP = B-type natriuretic peptide; PCW = pulmonary capillary wedge

Each of these patients had a clinically-indicated Echo-Doppler examination. Fifty-six of these patients had undergone cardiac catheterization with measurement of the pulmonary capillary wedge (PCW) within two days of the echo; 117 of the patients had a serum B-type natriuretic peptide (BNP) determination on the same day as the echo. In the validation cohort, we assessed the ability of CMM parameters to recognize diastolic dysfunction defined in three different ways. These included: 1) elevated mean PCW pressure > 18 mmHg; 2) elevated serum BNP > 100 pg/ml [31-33]; and 3) reduced IVPD < 2.2 mmHg indicating reduced LV suction [9].

6.3.10 Statistical Analysis

Data are expressed as mean ± 1 standard deviation. We analyzed statistical significance among groups using a one-way analysis of variance (ANOVA) and the Tukey-Kramer honest significant difference test.

The ability to distinguish patients with diastolic dysfunction from normal filling was analyzed by receiver operator characteristic (ROC) curves. The diagnostic ability of the parameters was assessed by comparing the area under the ROC curves [34]. JMP Statistical Discovery Software (SAS Institute Inc., Cary, NC) was used for the statistical analysis.

6.4 Results

6.4.1 Analysis of the Development Cohort

The isovelocity contours were not linear as the two stage initial and terminal fit provided considerably better fits than a single linear approximation (Table 3). This non-linearity was also present by visual inspection. Since the slope abruptly decreased at the discontinuity point, we termed this the "*deceleration point.*" Using a change-point analysis, the location of the deceleration point occurred furthermost into the LV for healthy patients and patients with delayed relaxation filling (3.1 ± 0.7cm and 3.3±0.8cm respectively) and progressively decreased with increased diastolic dysfunction (2.4 ± 0.6 cm for restrictive filling), shown in Figure 6.3A.

Table 6.3: Coefficient of Determination of Linear and Two Stage Initial and Terminal Contour Fits

Diastolic Dysfunction Stage	Linear Fit r^2 Value	Initial and Terminal Fit r^2 Value	p-value
Healthy, age < 30 yrs	0.77	0.84	0.0098
Healthy, age > 30 yrs	0.77	0.87	0.0328
Delayed Relaxation	0.76	0.84	0.0461
Pseudonormal	0.82	0.89	0.0716
Restrictive Filling	0.78	0.84	0.1065

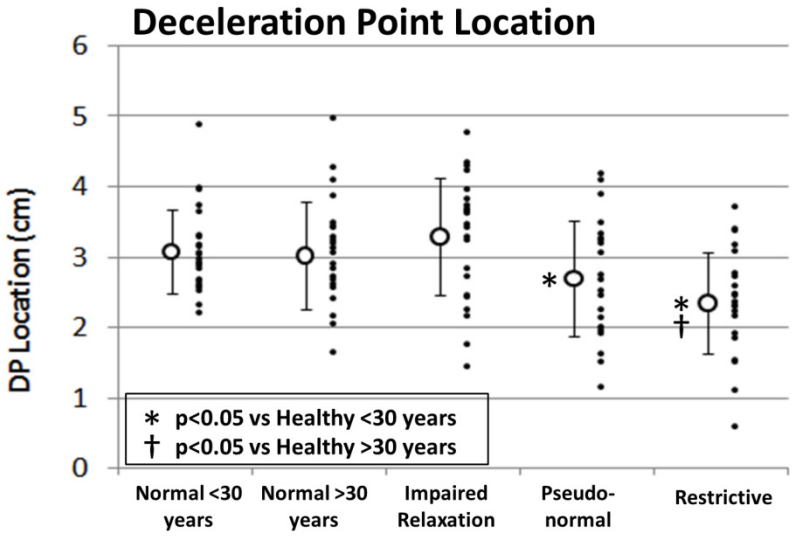

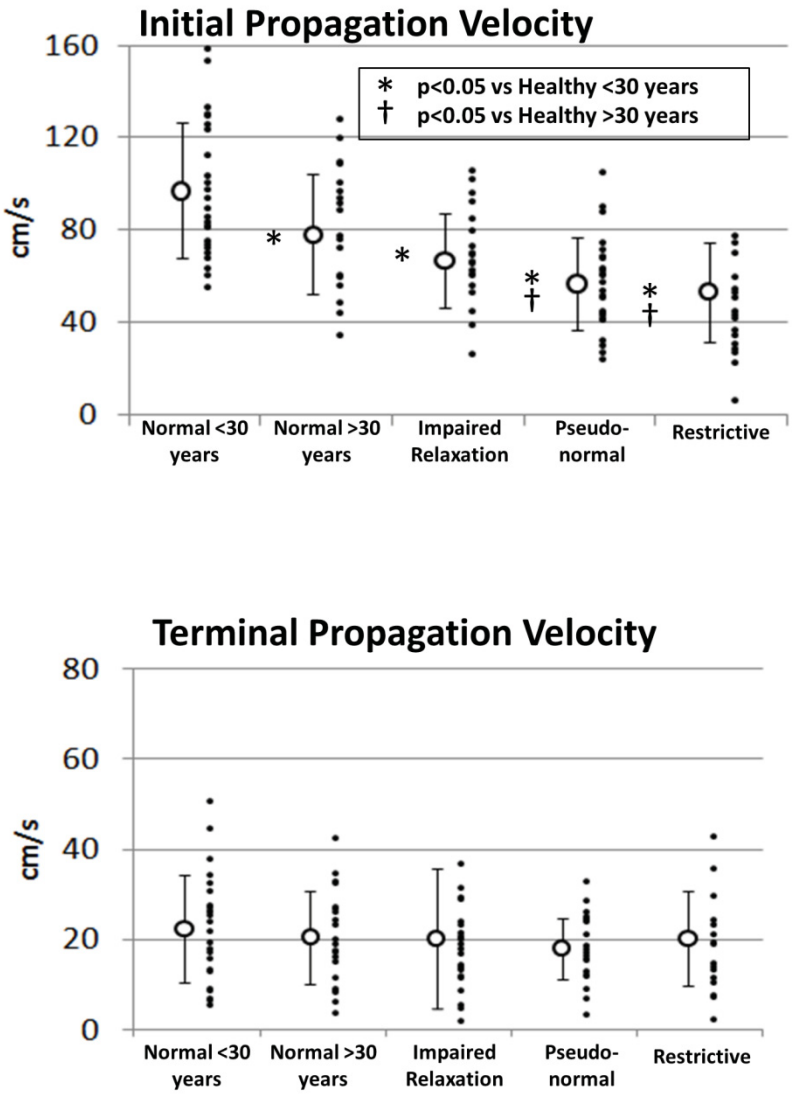

Figure 6.3: The distance into the left ventricle where the velocity deceleration point (DP) occurs is progressively decreased with more severe diastolic dysfunction, as is the initial propagation velocity. In contrast, the terminal propagation velocity is similar in all groups.

The inflow wave was split into an initial and terminal section before and after the deceleration point. The initial Vp progressively decreased with diastolic dysfunction shown in Figure 3B. The terminal Vp was lower than the initial Vp and was similar in normals and patients with increasing diastolic dysfunction shown in Figure 3C. Since both the initial Vp and the distance to the deceleration

point decreased with increasing diastolic dysfunction, we calculated their product as a potential new diastolic parameter. This product indicates the strength of the initial flow propagation (Vs) and represents the magnitude of LV suction. Vs was progressively decreased with increasing diastolic dysfunction (Figure 6.4B). In the development cohort, Vs was better at distinguishing patients with diastolic dysfunction from normals than conventional Vp (Figure 5).

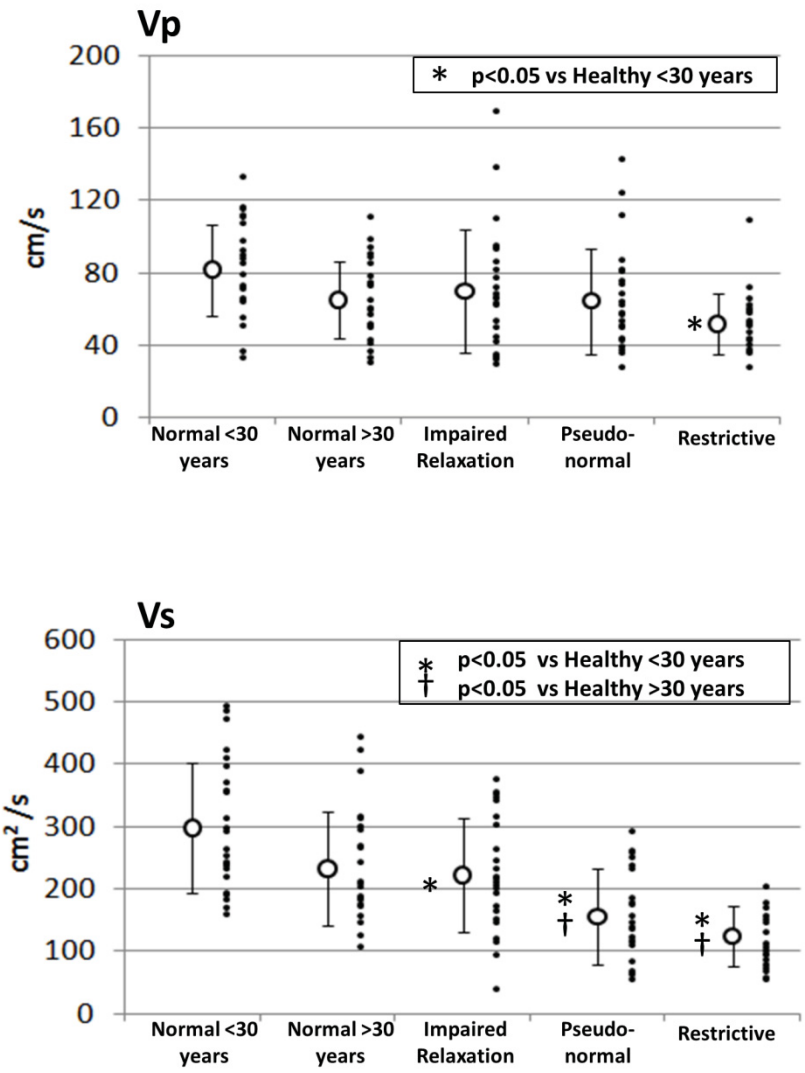

Figure 6.4: The conventional flow propagation velocity (Vp) is reduced in patients with restricted filling patterns. The early filling strength (Vs) progressively declines with increasing diastolic dysfunction.

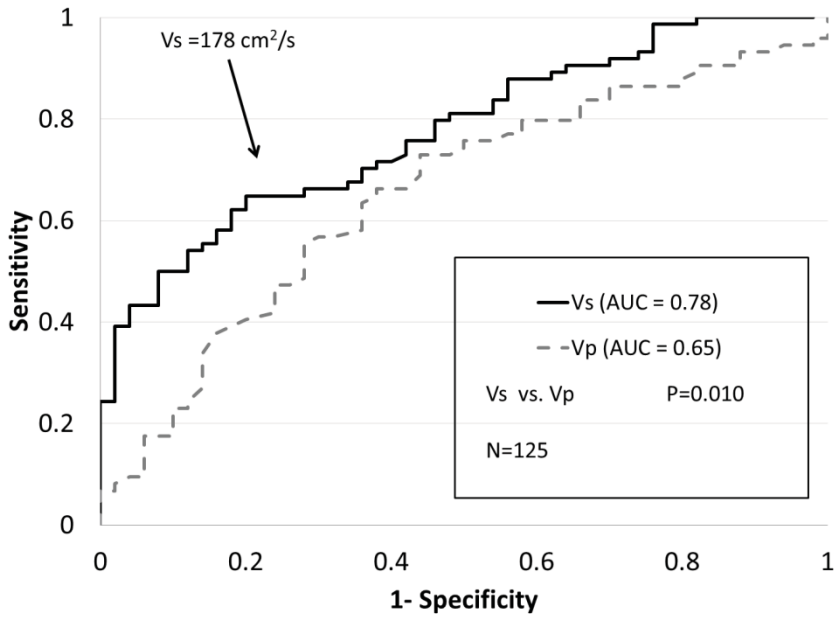

Figure 6.5: Receiver operator characteristic curves displaying the ability of conventional flow propagation velocity (Vp) and early filling strength (Vs) to discriminate normals from subjects with abnormal diastolic filling patterns. Vs performs better than Vp.

The variability of repeated measures of Vs was 9.9% for intraobserver and 13.8% for interobserver. Additional analysis of the intra and inter-observer variability values of Vs parameter, deceleration point location, initial Vp and terminal Vp values are in the supplemental materials.

Analysis of the Validation Cohort

In the validation cohort, Vs was consistently better at recognizing diastolic dysfunction than conventional Vp whether diastolic dysfunction was defined as a reduced IVPD, elevated PCW pressure, or elevated BNP (Figure 6).

Reduced Intraventricular Pressure Difference <2.2 mmHg

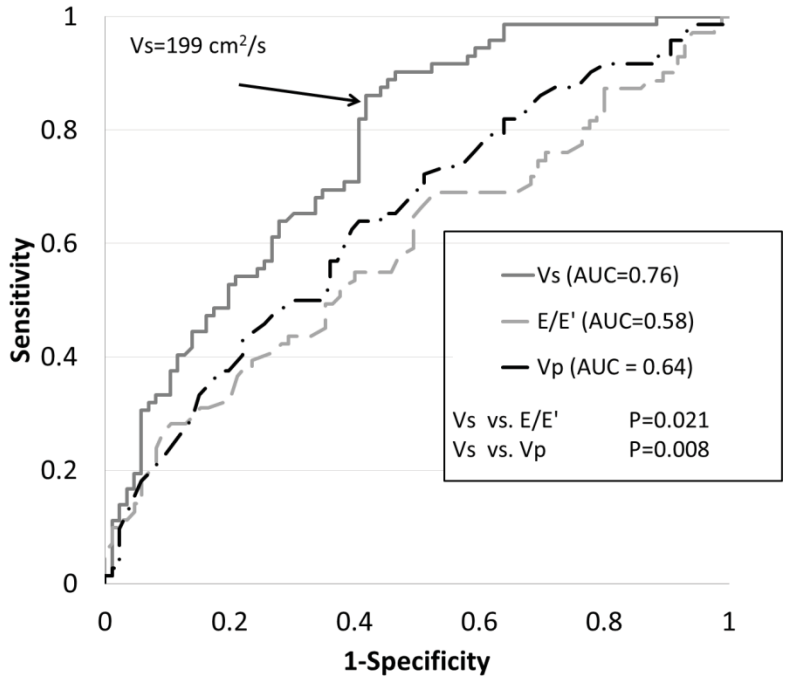

Elevated Pulmonary Capillary Wedge Pressure >18 mmHg

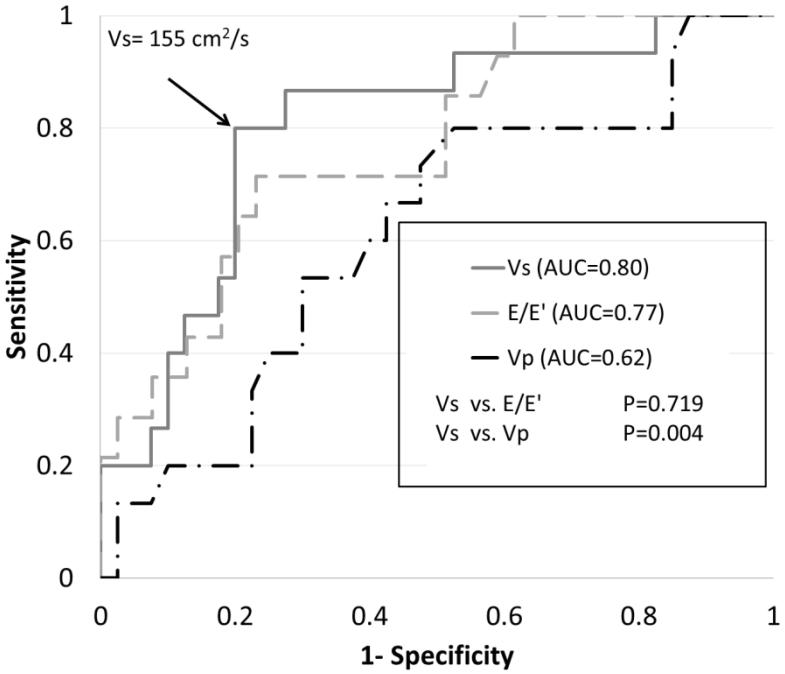

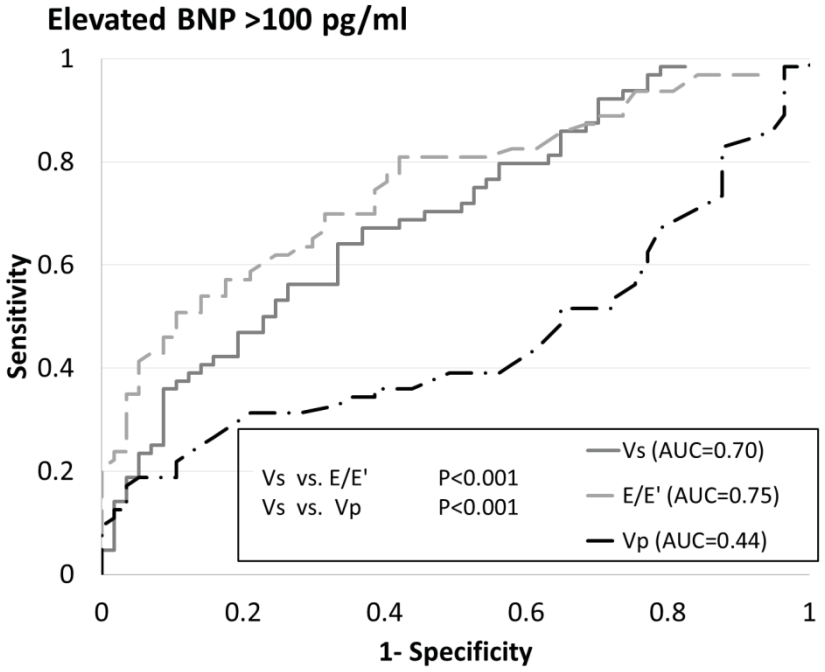

Figure 6.6: Receiver operator characteristic curves displaying the ability of color M-mode parameters to detect diastolic dysfunction recognized as: A) a reduced intraventricular pressure gradient (IVPD) < 2.2 mmHg, B) an elevated pulmonary capillary wedge pressure > 18 mmHg, and C) an elevated BNP > 100 pg/ml. Regardless of how diastolic dysfunction is defined, early filling strength (Vs) was superior to flow propagation velocity (Vp).

We separately analyzed 10 patients with HCM who had abnormal diastolic filling patterns and 50 normal subjects with normal filling pattern. Vs (AUC = 0.76) was superior to conventional Vp (AUC = 0.58, p =0.022) in detecting the 7 patients with HCM who had diastolic dysfunction(IVPD<2.2 mmHg).

6.5 Discussion

CMM echocardiography provides a spatial-temporal map of early diastolic filling. Conventionally, this has been evaluated by calculating the slope of an isovelocity contour representing the Vp. Using an objective quantitative analysis of the CMM data, we found that a single slope does not accurately represent the Vp for normals or patients with diastolic dysfunction. Instead, the flow

propagation is characterized by a more rapid initial slope indicating rapid flow propagation that abruptly slows after a deceleration point. In the presence of diastolic dysfunction, the initial slope is reduced and the deceleration point moves progressively closer to the mitral annulus. The terminal slope is much lower than the initial slope and is similar regardless of diastolic function. The product of the initial slope and the distance to the deceleration point (Vs) provides a measure of the strength of early diastolic LV suction and may provide a better measure of diastolic function than the conventional Vp.

Under normal circumstances, early diastolic filling results from a progressive pressure gradient from the left atrium [4, 22] that extends most of the way to the LV apex. This results in a rapid initial Vp that extends 3.1±0.7 cm from the mitral annulus towards the LV apex. With diastolic dysfunction, the magnitude of the pressure gradient is reduced, and it does not extend as deeply into the left ventricle [9]. Thus, we observed with diastolic dysfunction that the initial Vp is reduced and that filling wave decelerates to a lower velocity closer to the mitral annulus. After termination of the pressure gradient, the terminal Vp is reduced to similar levels in all subjects patients regardless of diastolic function. This terminal Vp represents slower inertial flow in the absence of a pressure gradient.

Vp is conventionally calculated as the linear slope of an isovelocity contour from the mitral annulus to 4 cm into the LV. Patients with normal filling display a deceleration point which occurs 3.1±0.7 cm from the annulus. Accordingly the initial Vp and conventional Vp for normal filling are similar. In contrast in restrictive filling, the deceleration point occurs closer to the mitral annulus (2.4±0.6 cm). Thus, in this circumstance the conventional Vp will be determined by both the initial Vp and the terminal Vp, further decreasing the conventional Vp below the initial Vp alone.

The conventional Vp is frequently normal in severely hypertrophied ventricles that have clear evidence of diastolic dysfunction [3]. Accordingly, we assessed the new Vs parameter in ten patients with HCM and found that its performance was superior to conventional Vp in accurately detecting diastolic dysfunction in HCM. These results should be interpreted with caution because of the small sample size.

We analyzed the degree of diastolic dysfunction in the development cohort based on the mitral inflow and tissue Doppler. In the validation cohort, we used BNP, IVPD, and invasively determined PCW pressure to provide three independent means of recognizing diastolic dysfunction. However, none of these standards is a perfect method of evaluating LV diastolic dysfunction. Increased BNP values are correlated with diastolic dysfunction [32]; however, BNP values can be influenced by other factors [35]. The IVPD provides another objective measure of the degree of diastolic dysfunction. We used a method to calculate the IVPD that has been validated by comparison to micromanometer pressure measurements [9, 29]. However, the values are not completely independent of the echocardiography analysis because

relative pressures were calculated from CMM using the Euler relationship. The PCW measurements were not performed simultaneously with the echocardiograms, thus diminishing the accuracy of the measurement is assessing diastolic dysfunction at the time of the echo / Doppler examination. Despite the potential limitations of the three methods of independently defining diastolic function, we found that Vs consistently performed better than Vp. This suggests that Vs provides a superior method of recognizing diastolic dysfunction from CMM echocardiography.

We used an algorithm to analyze a single beat of previously acquired clinical studies. It is possible that the algorithm could be implemented online as data are being acquired and applied to multiple beats. This has the potential to improve its accuracy. Although we used a quantitative analysis algorithm, the initial Vp and the distance to the deceleration point can be recognized by visual inspection (Figure 2).

In the development cohort, we included only patients with high quality CMM images. However, in the evaluation cohort, we did not exclude patients based on the quality of the images. This demonstrates the robustness of the analysis algorithm and the potential utility of Vs.

In conclusion, the propagation of flow into the left ventricle in early diastole does not have a single velocity. The initial rapid flow velocity suddenly slows at a deceleration point. Diastolic dysfunction is characterized by a reduction of the initial Vp and the deceleration point occurring closer to the mitral annulus. The product of these two parameters, Vs, which reflects the strength of early diastolic filling, provides a more accurate assessment of diastolic function than conventional measurement of Vp from CMM echocardiography.

Funding Sources

This work is partially supported by the National Science Foundation Graduate Research Fellowship and National Science Foundation Grant No. 0547434. Any opinions, findings, conclusions, or recommendations expressed in this publication are those of the authors and do not necessarily reflect the views of the National Science Foundation. We also acknowledge the Wake Forest Translational Science Institute for their financial support.

Disclosures

An application for a provisional patent covering the analysis program has been filed by Virginia Tech and Wake Forest Universities which employ the authors.

6.6 References

1. Thomas, J.D. and Z.B. Popovic, *Assessment of left ventricular function by cardiac ultrasound.* Journal of the American College of Cardiology, 2006. **48**(10): p. 2012-2025.
2. Oh, J.K., L. Hatle, A.J. Tajik, and W.C. Little, *Diastolic heart failure can be diagnosed by comprehensive two-dimensional and Doppler echocardiography.* Journal of the American College of Cardiology, 2006. **47**(3): p. 500-506.
3. Nagueh, S.F., C.P. Appleton, T.C. Gillebert, P.N. Marino, J.K. Oh, O.A. Smiseth, A.D. Waggoner, F.A. Flachskampf, P.A. Pellikka, A. Evangelisa, and E. Amer Soc, *Recommendations for the Evaluation of Left Ventricular Diastolic Function by Echocardiography.* European Journal of Echocardiography, 2009. **10**(2): p. 165-193.
4. Little, W.C., *Diastolic dysfunction beyond distensibility - Adverse effects of ventricular dilatation.* Circulation, 2005. **112**(19): p. 2888-2890.
5. Brun, P., C. Tribouilloy, A.M. Duval, L. Iserin, A. Meguira, G. Pelle, and J.L. Duboisrande, *Left-Ventricular Flow Propagation During Early Filling is Related to Wall Relaxation - A Color M-Mode Doppler Analaysis.* Journal of the American College of Cardiology, 1992. **20**(2): p. 420-432.
6. Stugaard, M., N.L. Greenberg, J.H. Zhou, and J.D. Thomas. *Automated eigenvector analysis for quantification of color M-mode Doppler filling patterns of the left ventricle in an ischemic canine model*. In *24th Annual IEEE Computers in Cardiology Conference*. 1997. Lund, Sweden.
7. Takatsuji, H., T. Mikami, K. Urasawa, J.I. Teranishi, H. Onozuka, C. Takagi, Y. Makita, H. Matsuo, H. Kusuoka, and A. Kitabatake, *A new approach for evaluation of left ventricular diastolic function: Spatial and temporal analysis of left ventricular filling flow propagation by color M-mode Doppler echocardiography.* Journal of the American College of Cardiology, 1996. **27**(2): p. 365-371.
8. Moller, J.E., E. Sondergaard, J.B. Seward, C.P. Appleton, and K. Egstrup, *Ratio of left ventricular peak E-wave velocity to flow propagation velocity assessed by color M-mode Doppler echocardiography in first myocardial infarction - Prognostic and clinical implications.* Journal of the American College of Cardiology, 2000. **35**(2): p. 363-370.
9. Yotti, R., J. Bermejo, J.C. Antoranz, M.M. Desco, C. Cortina, J.L. Rojo-Alvarez, C. Allue, L. Martin, M. Moreno, J.A. Serrano, R. Munoz, and M.A. Garcia-Fernandez, *A noninvasive method for assessing impaired diastolic suction in patients with dilated cardiomyopathy.* Circulation, 2005. **112**(19): p. 2921-2929.
10. De Mey, S., J. De Sutter, P. Vandervoort, M. De Buyzere, and P. Verdonck, *Assessment of LV Diastolic Filling Using Color M-Mode Doppler Echocardiography: Validation in a New Hydraulic Model*, in *Biomechan Model Mechanobiol*. 2004. p. 127-138.
11. Oh, J.K., *Echocardiography in heart failure: Beyond diagnosis.* European Journal of Echocardiography, 2007. **8**(1): p. 4-14.
12. Chapman, J.N., J. Mayet, R.A. Foale, and S.A. Thom, *Intraventricular dispersion of E wave velocity: an alternative measure of left ventricular diastolic function in hypertensive patients?* Journal of Human Hypertension, 1999. **13**(12): p. 867-869.
13. Bella, J.N., V. Palmieri, M.J. Roman, J.E. Liu, T.K. Welty, E.T. Lee, R.R. Fabsitz, B.V. Howard, and R.B. Devereux, *Mitral ratio of peak early to late diastolic filling velocity as a predictor of mortality in middle-aged and elderly adults - The strong heart study.* Circulation, 2002. **105**(16): p. 1928-1933.
14. Galderisi, M., *Diastolic dysfunction and diastolic heart failure: diagnostic, prognostic and therapeutic aspects.* Cardiovascular Ultrasound 2005. **3**(9).
15. Garcia, M., FACC, MJ, M. Ares, MA, M. Asher, C, M. Rodriguez, L, M. Vandervoort, P, and M. Thomas, FACC, JD, *An index of early left ventricular filling that combined with pulsed Doppler peak E velocity may estimate capillary wedge pressure.* Journal of the American College of Cardiology, 1997. **29**(2): p. 448-454.

16. Claessens, T.E., J. De Sutter, D. Vanhercke, P. Segers, and P.R. Verdonck, *New echocardiographic applications for assessing global left ventricular diastolic function.* Ultrasound in Medicine and Biology, 2007. **33**(6): p. 823-841.
17. Quinones, M.A., *Assessment of diastolic function.* Progress in Cardiovascular Diseases, 2005. **47**(5): p. 340-355.
18. Sessoms, M.W., J. Lisauskas, and S.J. Kovacs, *The left ventricular color M-mode Doppler flow propagation velocity V-p: In vivo comparison of alternative methods including physiologic implications.* Journal of the American Society of Echocardiography, 2002. **15**(4): p. 339-348.
19. Asada-Kamiguchi, J., M. Jones, N.L. Greenberg, Z.B. Popovic, H. Tsujino, A.D. Zetts, J.X. Qin, M.J. Garcia, J.D. Thomas, and T. Shiota, *Intraventricular pressure gradients in left ventricular aneurysms determined by color M-mode Doppler method: An animal study.* Journal of the American Society of Echocardiography, 2006. **19**(9): p. 1112-1118.
20. Seo, Y., T. Ishimitsu, T. Ishizu, K. Obara, N. Moriyama, S. Kawano, S. Watanabe, and I. Yamaguchi, *Assessment of propagation velocity by contrast echocardiography for standardization of color Doppler propagation velocity measurements.* Journal of the American Society of Echocardiography, 2004. **17**(12): p. 1266-1274.
21. Barbier, P., A. Grimaldi, M. Alimento, G. Berna, and M.D. Guazzi, *Echocardiographic determinants of mitral early flow propagation velocity.* American Journal of Cardiology, 2002. **90**(6): p. 613-619.
22. Little, W.C. and J.K. Oh, *Echocardiographic Evaluation of Diastolic Function Can Be Used to Guide Clinical Care.* Circulation, 2009. **120**(9): p. 802-809.
23. Gandhi, S.K., J.C. Powers, A. Nomeir, K. Fowle, D.W. Kitzman, K.M. Rankin, and W.C. Little, *The pathogenesis of acute pulmonary edema associated with hypertension.* New England Journal of Medicine, 2001. **344**(1): p. 17-22.
24. Warner, J.G., D.C. Metzger, D.W. Kitzman, D.J. Wesley, and W.C. Little, *Losartan improves exercise tolerance in patients with diastolic dysfunction and a hypertensive response to exercise.* Journal of the American College of Cardiology, 1999. **33**(6): p. 1567-1572.
25. Thomas, J.D., N.L. Greenberg, P.M. Vandervoort, D.S. Aghassi, and B.F. Hunt. *Digital analysis of transmitral color Doppler M-mode data: a potential new approach to the noninvasive assessment of diastolic function*. In *Computers in Cardiology 1992. Proceedings.* 1992.
26. Rovner, A., R. Smith, N.L. Greenberg, E.M. Tuzcu, N. Smedira, H.M. Lever, J.D. Thomas, and M.J. Garcia. *Improvement in diastolic intraventricular pressure gradients in patients with HOCM after ethanol septal reduction*. In *Annual Meeting of the American-College-of-Cardiology*. 2002. Atlanta, Georgia.
27. Hinkley, D.V., *Inference about the Change-Point from Cumulative Sum Tests* Biometrika 1971. **58**(3): p. 509-523
28. Taylor, W.A. *Change-Point Analysis: A Powerful New Tool For Detecting Changes*. 2000 7/16/2008]; Available from: http://www.variation.com/cpa/tech/changepoint.html.
29. Thomas, J.D. and Z.B. Popovic, *Intraventricular pressure differences - A new window into cardiac function.* Circulation, 2005. **112**(12): p. 1684-1686.
30. Greenberg, N.L., P.M. Vandervoort, M.S. Firstenberg, M.J. Garcia, and J.D. Thomas, *Estimation of diastolic intraventricular pressure gradients by Doppler M-mode echocardiography.* American Journal of Physiology-Heart and Circulatory Physiology, 2001. **280**(6): p. H2507-H2515.
31. Brucks, S., W.C. Little, T. Chao, D.W. Kitzman, D. Wesley-Farrington, S. Gandhi, and Z.K. Shihabi, *Contribution of left ventricular diastolic dysfunction to heart failure regardless of election fraction.* American Journal of Cardiology, 2005. **95**(5): p. 603-606.
32. Dokainish, H., W.A. Zoghbi, N.M. Lakkis, F. Al-Bakshy, M. Dhir, M.A. Quinones, and S.F. Nagueh, *Optimal noninvasive assessment of left ventricular filling pressures - A comparison of tissue Doppler echocardiography and B-type natriuretic peptide in patients with pulmonary artery catheters*. Circulation, 2004. **109**(20): p. 2432-2439.

33. Maeda, K., T. Tsutamoto, A. Wada, T. Hisanaga, and M. Kinoshita, *Plasma brain natriuretic peptide as a biochemical marker of high left ventricular end-diastolic pressure in patients with symptomatic left ventricular dysfunction.* American Heart Journal, 1998. **135**(5): p. 825-832.
34. Hanley, J.A. and B.J. McNeil, *A Method of Comparing the Areas Under Receiver Operating Characteristic Curves Derived from the Same Cases.* Radiology, 1983. **148**(3): p. 839-843.
35. Cowie, M.R. and G.F. Mendez, *BNP and congestive heart failure.* Current Problems in Cardiology, 2003. **28**(4): p. 264-311.

6.7 Supplemental Material

6.7.1 Description of the Automated Algorithm

An automated data analysis algorithm was developed to determine the Vp from CMM echocardiograph images. Original CMM images were analyzed in MATLAB (The Mathworks, Natick, MA) using in-house developed image processing algorithms. From the original CMM image (Figure 6.1A), the velocity color scale region was selected and a single beat region of interest was selected from the CMM image shown in Figure 6.1B. From this ROI, the E-wave, A-wave, and the vertical position of the mitral plane were selected for orientation of the algorithm. The grayscale values from the CMM image background were removed, thus leaving only the velocity color scale image (Figure 6.1C). Color scale cubic spline values were then used to create a point-by-point velocity reconstruction of the remaining image.

A de-aliasing technique similar to the techniques used by Thomas et al. and Rovner et al. [1, 2] was used to reconstruct the image shown in Figure 6.1D. Through the use of image processing tools, the E-wave velocity field was reduced to a series of twenty-seven isovelocity contours evenly spaced between 45% and 55% of the peak E-wave transmitral velocity shown in Figure 6.1E. The reconstructed velocity contours are shown in Figure 6.1F with the 45% to 55% isovelocity contours shown from light to dark.

6.7.2 Ensemble Contour Methodology

A smoothing spline was fit to a series of isovelocity contours and is referred to as the ensemble contour in the remaining analysis. Error analysis using 25 representative patients spanning the five categories considered in this study was performed to determine the optimum number of ensemble contours required for the reconstruction. This analysis showed that a minimum of 27 velocity waveforms should be used for the optimal reconstruction and ensured that, in all representative cases, there was no more than a 1% change in r^2 values with an increasing number of waveforms.

6.7.3 Change-Point Methodology

Preliminary analysis of the isovelocity contours revealed the presence of an apparent decrease in the slope of the velocity ensemble contours indicating deceleration of the filling wave. This is consistent with previous observations of a change in slope or curvilinear isovelocity contour [3-5]. We used a statistical change-point analysis method [6, 7] on the derivative of the ensemble contour to determine the deceleration point. The method is based on a cumulative sum of the difference between the value of interest (x_i) and the mean value ($\bar{x}$). Equation 6.3 displays the cumulative sum equation:

$$\text{Cumulative Sum}_i = \text{Cumulative Sum}_{i-1} + (x_i - \bar{x}). \quad 6.4$$

The waveform produced by the output of the cumulative sum equation was plotted to determine the significance of the change throughout the signal. The peaks within this cumulative sum waveform were sorted according to their magnitude. The peak with the highest magnitude signifies the most statistically significant change and was labeled as the *"deceleration point."*

6.7.4 Intra and Inter-observer Variability Analysis

Seventeen patients were analyzed three times by three different observers. With this data we have completed inter-observer and intra-observer variability analysis. The table below displays the average of the mean percent error of the three observations for all of the patients for the intraobserver variability. The interobserver variability is the average of the mean percent error of the mean value of each patient per observer. The mean percent error is shown in equation 6.4. Where n is the number of observation pairs analyzed,

$$\text{mean \% error} = \frac{1}{n}\sum_{t=1}^{n} \frac{\left|observation_t - observation_{t+1}\right|}{\left(\frac{observation_t - observation_{t+1}}{2}\right)}. \quad 6.5$$

Development Cohort Reproducibility

	Vs	Deceleration Point	Initial Vp	Terminal Vp
Intra-observer Variability (%	9.9 ± 13.2	6.4 ± 10.4	9.2 ± 15.1	9.4 ± 15.8
Inter-observer Variability (%	13.8 ± 11.5	7.1 ± 9.2	4.6 ± 14.3	9.1 ± 21.5

6.7.5 References

1. Thomas, J.D., N.L. Greenberg, P.M. Vandervoort, D.S. Aghassi, and B.F. Hunt. *Digital analysis of transmitral color Doppler M-mode data: a potential new approach to the noninvasive assessment of diastolic function*. In *Computers in Cardiology 1992. Proceedings.* 1992.
2. Rovner, A., R. Smith, N.L. Greenberg, E.M. Tuzcu, N. Smedira, H.M. Lever, J.D. Thomas, and M.J. Garcia. *Improvement in diastolic intraventricular pressure gradients in patients with HOCM after ethanol septal reduction*. In *Annual Meeting of the American-College-of-Cardiology*. 2002. Atlanta, Georgia.
3. Quinones, M.A., *Assessment of diastolic function.* Progress in Cardiovascular Diseases, 2005. **47**(5): p. 340-355.
4. Sessoms, M.W., J. Lisauskas, and S.J. Kovacs, *The left ventricular color M-mode Doppler flow propagation velocity V-p: In vivo comparison of alternative methods including physiologic implications.* Journal of the American Society of Echocardiography, 2002. **15**(4): p. 339-348.
5. Asada-Kamiguchi, J., M. Jones, N.L. Greenberg, Z.B. Popovic, H. Tsujino, A.D. Zetts, J.X. Qin, M.J. Garcia, J.D. Thomas, and T. Shiota, *Intraventricular pressure gradients in left ventricular aneurysms determined by color M-mode Doppler method: An animal study.* Journal of the American Society of Echocardiography, 2006. **19**(9): p. 1112-1118.
6. Hinkley, D.V., *Inference about the Change-Point from Cumulative Sum Tests* Biometrika 1971. **58**(3): p. 509-523
7. Taylor, W.A. *Change-Point Analysis: A Powerful New Tool For Detecting Changes*. 2000 7/16/2008]; Available from: http://www.variation.com/cpa/tech/changepoint.html.

7 Conclusions

This dissertation has provided an integrated analysis of vortex ring dynamics within in-vivo and in-vitro data. We hypothesized that variation in vortex ring dynamics within the LV were caused by changes in ventricular geometry. Therefore impaired LV relaxation, which causes a decrease in LV volume during filling, results in a more rapid decay of early diastolic hydrodynamic circulation, which is a measure of the vortex strength. Vortex ring have previously been examined in-vitro within compliant mock ventricles; however a fundamental understanding of confined vortex ring dynamics has not been previously established. Within this work we investigated vortex rings generated with varying Reynolds numbers and within a range of confinement domains. The characteristics of laminar vortex rings in-vitro were independently studied in order to develop a new analytical model for the evolution of the vortex ring circulation subject to the effect of the confinement. This improved understanding of the dynamics within simple radially confined domains was essential to more completely comprehend the role of vortex rings in diastolic filling.

This work was the first to investigated vortex ring formation and decay within radially confined domains, as in the filling left ventricle. The Reynolds numbers, based on circulation, for the vortex rings within the left ventricle are approximated between 4,000 and 10,000. For this reason we investigated radially confined vortex rings over a range of Reynolds numbers. We found that the vortex ring formation process was unaffected by the introduction of the confinement domain. However, the vortex rings with increased confinement displayed an onset of enhanced circulation decay after the time of vortex ring formation. The circulation decay rate after pinch-off remained constant for all vortex rings generated within a single severe confinement with varying generation conditions, implying the decay rate is dependent on the ratio of piston cylinder to confinement diameters. Radially confined laminar vortex rings were further investigated and we discovered that the circulation decay rate increased exponentially with increasing vortex ring confinement. The development of a method for estimating the rate of vortex ring circulation decay within significant physical processes was very important. The analytical model developed within this work can be used to predict the rate of circulation decay within the filling LV subject to changing physiological characteristics of the LV. Therefore this model may be used with clinical pcMRI data to more completely understand the filling dynamics and potentially lead to improved diagnostic techniques.

The role of vortex ring formation within the left ventricle was further investigated using clinical color M-mode echocardiography and Doppler data. This work was the first to demonstrate that the nondimensional vortex ring pinch-off time does not vary with age or diastolic dysfunction condition. In

contrast with the previously hypothesized concept that variations in vortex ring dynamics may reflect the decline of diastolic function [1], the results suggested that vortex ring formation beyond the mitral valve remains invariant to pathophysiological changes associated with diastolic dysfunction. These findings enhance our understanding of early diastolic physics, potentially leading to improved diagnostic techniques [1-4]. After understanding the role of vortex ring pinch-off within early diastolic filling and observing a deceleration during early diastolic propagation velocity, we investigated the validity of the assumptions utilized in the conventional propagation velocity parameter. We found that the propagation of flow into the left ventricle in early diastole does not have a single velocity, as conventionally assumed. Instead, the initial rapid flow velocity suddenly slows at a deceleration point. Patients suffering from diastolic dysfunction are characterized by a reduction of the initial propagation velocity and the deceleration point occurring closer to the mitral annulus. In contrast, patients with normal filling display a high initial propagation velocity and a deceleration point towards the apex. The product of these two parameters, the early filling strength parameter (Vs), which reflects the strength of early diastolic filling, provides a more accurate assessment of diastolic function than conventional measurement of propagation velocity from Color M-mode echocardiography.

This work represents an important step towards a more complete understanding of early diastolic filling dynamics and the role of vortex rings within this filling. First, this work studied the effects of downstream confinement on vortex ring dynamics and showed conclusively that the vortex ring dynamics are greatly altered by the confined domain and specifically the ratio of the vortex ring diameter to the confinement diameter. Work which compares unconfined vortex rings generated within semi-infinite domains to vortex rings generated within the left ventricle are severely neglecting the effects of the left ventricular walls. Second, the formation time of the vortex rings formed within the left ventricle was accurately determined within this study, as opposed to assuming the vortex ring pinch-off occurs at the end of early diastolic filling. This work found that the deceleration of the early diastolic propagation wave and correspondingly the onset of the lack of a favorable pressure difference within the left ventricle were directly related to the pinch-off of the vortex ring. This allowed us for the first time to accurately calculate the vortex ring formation time and conclude that this time is invariant to variations in diastolic function and suggests that the heart is constantly adapting to physiological changes in order to remain as efficient as possible.

7.1 Future Work

There are several areas in which work must continue to further understand the filling dynamics of the left ventricle throughout the progression of diastolic dysfunction and advance this current work.

- The experiments in Chapter 3 should be completed by varying the piston velocity in order to generate the range of Reynolds number as opposed to varying the piston stroke length. This should be completed to confirm the results in Chapter 3.

- The model presented in Chapter 4 should be applied to clinical phase contrast magnetic resonance imaging (pcMRI) data over the early filling duration. The analytical model can be used to predict the rate of circulation decay within the filling LV subject to changing physiological characteristics of the LV, and may be used to more completely understand the filling dynamics and potentially lead to improved diagnostic techniques.

- The vortex ring studies presented within this work should be examined using dynamically expanding walls to study vortex ring dynamics during the relaxation phase of the heart. Similarly, vortex rings should be studied in a model compliant left ventricle with compliant and dynamically expanding left ventricular walls.

- The work in Chapter 4 should be completed with varying Reynolds numbers for each confinement domain case. This is necessary to determine if the conclusions stated in Chapter 4 are dependent on the confinement domain, the Reynolds number or both.

- A large number of additional patients must be analyzed using the techniques presented in Chapter 6 and calculating the early filling strength, Vs, parameter in combination with other clinically diagnostic tests and parameters to test the diagnostic strength of the parameter and move towards clinical trials.

7.2 References

1. Gharib, M., E. Rambod, A. Kheradvar, D.J. Sahn, and J.O. Dabiri, *Optimal vortex formation as an index of cardiac health.* Proceedings of the National Academy of Sciences of the United States of America, 2006. **103**(16): p. 6305-6308.
2. Ishizu, T., Y. Seo, T. Ishimitsu, K. Obara, N. Moriyama, S. Kawano, S. Watanabe, and I. Yamaguchi, *The wake of a large vortex is associated with intraventricular filling delay in impaired left ventricles with a pseudonormalized transmitral flow pattern.* Echocardiography, 2006. **23**(5): p. 369-375.
3. Baccani, B., F. Domenichini, G. Pedrizzetti, and G. Tonti, *Fluid dynamics of the left ventricular filling in dilated cardiomyopathy.* Journal of Biomechanics, 2002. **35**(5): p. 665-671.
4. Kheradvar, A. and M. Gharib, *On Mitral Valve Dynamics and its Connection to Early Diastolic Flow.* Annals of Biomedical Engineering, 2009. **37**(1): p. 1-13.

8 Appendix

8.1 IRB Approval Letters

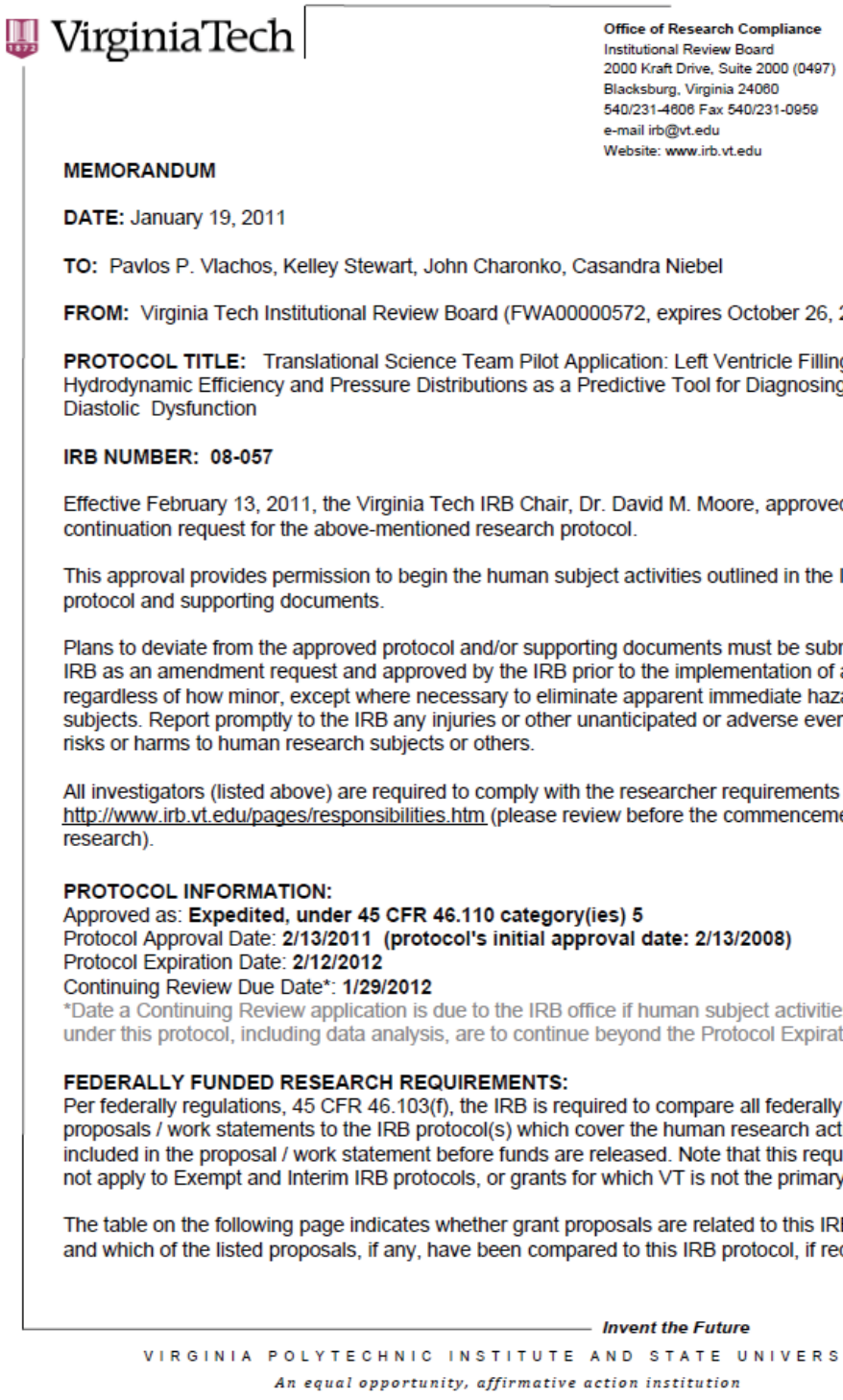

VirginiaTech

Office of Research Compliance
Institutional Review Board
2000 Kraft Drive, Suite 2000 (0497)
Blacksburg, Virginia 24060
540/231-4606 Fax 540/231-0959
e-mail irb@vt.edu
Website: www.irb.vt.edu

MEMORANDUM

DATE: January 19, 2011

TO: Pavlos P. Vlachos, Kelley Stewart, John Charonko, Casandra Niebel

FROM: Virginia Tech Institutional Review Board (FWA00000572, expires October 26, 2013)

PROTOCOL TITLE: Translational Science Team Pilot Application: Left Ventricle Filling Hydrodynamic Efficiency and Pressure Distributions as a Predictive Tool for Diagnosing Cardiac Diastolic Dysfunction

IRB NUMBER: 08-057

Effective February 13, 2011, the Virginia Tech IRB Chair, Dr. David M. Moore, approved the continuation request for the above-mentioned research protocol.

This approval provides permission to begin the human subject activities outlined in the IRB-approved protocol and supporting documents.

Plans to deviate from the approved protocol and/or supporting documents must be submitted to the IRB as an amendment request and approved by the IRB prior to the implementation of any changes, regardless of how minor, except where necessary to eliminate apparent immediate hazards to the subjects. Report promptly to the IRB any injuries or other unanticipated or adverse events involving risks or harms to human research subjects or others.

All investigators (listed above) are required to comply with the researcher requirements outlined at http://www.irb.vt.edu/pages/responsibilities.htm (please review before the commencement of your research).

PROTOCOL INFORMATION:
Approved as: **Expedited, under 45 CFR 46.110 category(ies) 5**
Protocol Approval Date: **2/13/2011 (protocol's initial approval date: 2/13/2008)**
Protocol Expiration Date: **2/12/2012**
Continuing Review Due Date*: **1/29/2012**
*Date a Continuing Review application is due to the IRB office if human subject activities covered under this protocol, including data analysis, are to continue beyond the Protocol Expiration Date.

FEDERALLY FUNDED RESEARCH REQUIREMENTS:
Per federally regulations, 45 CFR 46.103(f), the IRB is required to compare all federally funded grant proposals / work statements to the IRB protocol(s) which cover the human research activities included in the proposal / work statement before funds are released. Note that this requirement does not apply to Exempt and Interim IRB protocols, or grants for which VT is not the primary awardee.

The table on the following page indicates whether grant proposals are related to this IRB protocol, and which of the listed proposals, if any, have been compared to this IRB protocol, if required.

VirginiaTech

Office of Research Compliance
Institutional Review Board
2000 Kraft Drive, Suite 2000 (0497)
Blacksburg, Virginia 24061
540/231-4991 Fax 540/231-0959
e-mail moored@vt.edu
www.irb.vt.edu
FWA00000572(expires 1/20/2010)
IRB # is IRB00000667

DATE: January 19, 2010

MEMORANDUM

TO: Pavlos P. Vlachos
Kelley Stewart
John Charonko

Approval date: 2/13/2010
Continuing Review Due Date:1/29/2011
Expiration Date: 2/12/2011

FROM: David M. Moore

SUBJECT: **IRB Expedited Continuation 2:** "Translational Science Team Pilot Application: Left Ventricle Filling Hydrodynamic Efficiency and Pressure Distributions as a Predictive Tool for Diagnosing Cardiac Diastolic Dysfunction" , IRB # 08-057

This memo is regarding the above referenced protocol which was previously granted expedited approval by the IRB. The proposed research is eligible for expedited review according to the specifications authorized by 45 CFR 46.110 and 21 CFR 56.110. Pursuant to your request, as Chair of the Virginia Tech Institutional Review Board, I have granted approval for extension of the study for a period of 12 months, effective as of February 13, 2010.

Approval of your research by the IRB provides the appropriate review as required by federal and state laws regarding human subject research. As an investigator of human subjects, your responsibilities include the following:

1. Report promptly proposed changes in previously approved human subject research activities to the IRB, including changes to your study forms, procedures and investigators, regardless of how minor. The proposed changes must not be initiated without IRB review and approval, except where necessary to eliminate apparent immediate hazards to the subjects.
2. Report promptly to the IRB any injuries or other unanticipated or adverse events involving risks or harms to human research subjects or others.
3. Report promptly to the IRB of the study's closing (i.e., data collecting and data analysis complete at Virginia Tech). If the study is to continue past the expiration date (listed above), investigators must submit a request for continuing review prior to the continuing review due date (listed above). It is the researcher's responsibility to obtain re-approval from the IRB before the study's expiration date.
4. If re-approval is not obtained (unless the study has been reported to the IRB as closed) prior to the expiration date, all activities involving human subjects and data analysis must cease immediately, except where necessary to eliminate apparent immediate hazards to the subjects.

cc: File

VirginiaTech

Office of Research Compliance
Institutional Review Board
2000 Kraft Drive, Suite 2000 (0497)
Blacksburg, Virginia 24061
540/231-4991 Fax 540/231-0959
e-mail moored@vt.edu
www.irb.vt.edu
FWA00000572(expires 1/20/2010)
IRB # is IRB00000667

DATE: January 21, 2009

MEMORANDUM

TO: Pavlos P. Vlachos
Kelley Stewart
John Charonko

FROM: David M. Moore

Approval date: 2/13/2009
Continuing Review Due Date:1/29/2010
Expiration Date: 2/12/2010

SUBJECT: **IRB Expedited Continuation 1:** "Translational Science Team Pilot Application: Left Ventricle Filling Hydrodynamic Efficiency and Pressure Distributions as a Predictive Tool for Diagnosing Cardiac Diastolic Dysfunction" , IRB # 08-057

This memo is regarding the above referenced protocol which was previously granted expedited approval by the IRB. The proposed research is eligible for expedited review according to the specifications authorized by 45 CFR 46.110 and 21 CFR 56.110. Pursuant to your request, as Chair of the Virginia Tech Institutional Review Board, I have granted approval for extension of the study for a period of 12 months, effective as of February 13, 2009.

Approval of your research by the IRB provides the appropriate review as required by federal and state laws regarding human subject research. As an investigator of human subjects, your responsibilities include the following:

1. Report promptly proposed changes in previously approved human subject research activities to the IRB, including changes to your study forms, procedures and investigators, regardless of how minor. The proposed changes must not be initiated without IRB review and approval, except where necessary to eliminate apparent immediate hazards to the subjects.
2. Report promptly to the IRB any injuries or other unanticipated or adverse events involving risks or harms to human research subjects or others.
3. Report promptly to the IRB of the study's closing (i.e., data collecting and data analysis complete at Virginia Tech). If the study is to continue past the expiration date (listed above), investigators must submit a request for continuing review prior to the continuing review due date (listed above). It is the researcher's responsibility to obtain re-approval from the IRB before the study's expiration date.
4. If re-approval is not obtained (unless the study has been reported to the IRB as closed) prior to the expiration date, all activities involving human subjects and data analysis must cease immediately, except where necessary to eliminate apparent immediate hazards to the subjects.

cc: File

VirginiaTech

Office of Research Compliance
Institutional Review Board
2000 Kraft Drive, Suite 2000 (0497)
Blacksburg, Virginia 24061
540/231-4991 Fax 540/231-0959
e-mail moored@vt.edu
www.irb.vt.edu
FWA00000572(expires 1/20/2010)
IRB # is IRB00000667

DATE: February 14, 2008

MEMORANDUM

TO: Pavlos P. Vlachos
Kelley Stewart
John Charonko

Approval date: 2/13/2008
Continuing Review Due Date:1/29/2009
Expiration Date: 2/12/2009

FROM: David M. Moore

SUBJECT: **IRB Expedited Approval:** "Translational Science Team Pilot Application: Left Ventricle Filling Hydrodynamic Efficiency and Pressure Distributions as a Predictive Tool for Diagnosing Cardiac Diastolic Dysfunction" , IRB # 08-057

This memo is regarding the above-mentioned protocol. The proposed research is eligible for expedited review according to the specifications authorized by 45 CFR 46.110 and 21 CFR 56.110. As Chair of the Virginia Tech Institutional Review Board, I have granted approval to the study for a period of 12 months, effective February 13, 2008.

As an investigator of human subjects, your responsibilities include the following:

1. Report promptly proposed changes in previously approved human subject research activities to the IRB, including changes to your study forms, procedures and investigators, regardless of how minor. The proposed changes must not be initiated without IRB review and approval, except where necessary to eliminate apparent immediate hazards to the subjects.
2. Report promptly to the IRB any injuries or other unanticipated or adverse events involving risks or harms to human research subjects or others.
3. Report promptly to the IRB of the study's closing (i.e., data collecting and data analysis complete at Virginia Tech). If the study is to continue past the expiration date (listed above), investigators must submit a request for continuing review prior to the continuing review due date (listed above). It is the researcher's responsibility to obtained re-approval from the IRB before the study's expiration date.
4. If re-approval is not obtained (unless the study has been reported to the IRB as closed) prior to the expiration date, all activities involving human subjects and data analysis must cease immediately, except where necessary to eliminate apparent immediate hazards to the subjects.

Important:
If you are conducting **federally funded non-exempt research**, this approval letter must state that the IRB has compared the OSP grant application and IRB application and found the documents to be consistent. Otherwise, this approval letter is invalid for OSP to release funds. Visit our website at http://www.irb.vt.edu/pages/newstudy.htm#OSP for further information.

cc: File

8.2 Copyright Permission Letter

ELSEVIER LICENSE
TERMS AND CONDITIONS
Apr 13, 2011

This is a License Agreement between Kelley C Stewart ("You") and Elsevier ("Elsevier") provided by Copyright Clearance Center ("CCC"). The license consists of your order details, the terms and conditions provided by Elsevier, and the payment terms and conditions.

All payments must be made in full to CCC. For payment instructions, please see information listed at the bottom of this form.

Supplier	Elsevier Limited The Boulevard,Langford Lane Kidlington,Oxford,OX5 1GB,UK
Registered Company Number	1982084
Customer name	Kelley C Stewart
Customer address	928 Kabrich Street Blacksburg, VA 24060
License number	2647070380678
License date	Apr 13, 2011
Licensed content publisher	Elsevier
Licensed content publication	JACC: Cardiovascular Imaging
Licensed content title	Evaluation of LV Diastolic Function From Color M-Mode Echocardiography
Licensed content author	Kelley C. Stewart, Rahul Kumar, John J. Charonko, Takahiro Ohara, Pavlos P. Vlachos, William C. Little
Licensed content date	January 2011
Licensed content volume number	4
Licensed content issue number	1
Number of pages	10
Start Page	37
End Page	46
Type of Use	reuse in a thesis/dissertation
Portion	full article

Format	electronic
Are you the author of this Elsevier article?	Yes
Will you be translating?	No
Order reference number	
Title of your thesis/dissertation	Hydrodynamics of Cardiac Diastole
Expected completion date	May 2011
Estimated size (number of pages)	100
Elsevier VAT number	GB 494 6272 12
Permissions price	0.00 USD
VAT/Local Sales Tax	0.00 USD / GBP
Total	0.00 USD
Terms and Conditions	

INTRODUCTION

1. The publisher for this copyrighted material is Elsevier. By clicking "accept" in connection with completing this licensing transaction, you agree that the following terms and conditions apply to this transaction (along with the Billing and Payment terms and conditions established by Copyright Clearance Center, Inc. ("CCC"), at the time that you opened your Rightslink account and that are available at any time at http://myaccount.copyright.com).

GENERAL TERMS

2. Elsevier hereby grants you permission to reproduce the aforementioned material subject to the terms and conditions indicated.

3. Acknowledgement: If any part of the material to be used (for example, figures) has appeared in our publication with credit or acknowledgement to another source, permission must also be sought from that source. If such permission is not obtained then that material may not be included in your publication/copies. Suitable acknowledgement to the source must be made, either as a footnote or in a reference list at the end of your publication, as follows:

"Reprinted from Publication title, Vol /edition number, Author(s), Title of article / title of chapter, Pages No., Copyright (Year), with permission from Elsevier [OR APPLICABLE SOCIETY COPYRIGHT OWNER]." Also Lancet special credit - "Reprinted from The Lancet, Vol. number, Author(s), Title of article, Pages No., Copyright (Year), with permission from Elsevier."

4. Reproduction of this material is confined to the purpose and/or media for which permission is hereby given.

5. Altering/Modifying Material: Not Permitted. However figures and illustrations may be altered/adapted minimally to serve your work. Any other abbreviations, additions, deletions and/or any other alterations shall be made only with prior written authorization of Elsevier Ltd. (Please contact Elsevier at permissions@elsevier.com)

6. If the permission fee for the requested use of our material is waived in this instance, please be advised that your future requests for Elsevier materials may attract a fee.

7. Reservation of Rights: Publisher reserves all rights not specifically granted in the combination of (i) the license details provided by you and accepted in the course of this licensing transaction, (ii) these terms and conditions and (iii) CCC's Billing and Payment terms and conditions.

8. License Contingent Upon Payment: While you may exercise the rights licensed immediately upon issuance of the license at the end of the licensing process for the transaction, provided that you have disclosed complete and accurate details of your proposed use, no license is finally effective unless and until full payment is received from you (either by publisher or by CCC) as provided in CCC's Billing and Payment terms and conditions. If full payment is not received on a timely basis, then any license preliminarily granted shall be deemed automatically revoked and shall be void as if never granted. Further, in the event that you breach any of these terms and conditions or any of CCC's Billing and Payment terms and conditions, the license is automatically revoked and shall be void as if never granted. Use of materials as described in a revoked license, as well as any use of the materials beyond the scope of an unrevoked license, may constitute copyright infringement and publisher reserves the right to take any and all action to protect its copyright in the materials.

9. Warranties: Publisher makes no representations or warranties with respect to the licensed material.

10. Indemnity: You hereby indemnify and agree to hold harmless publisher and CCC, and their respective officers, directors, employees and agents, from and against any and all claims arising out of your use of the licensed material other than as specifically authorized pursuant to this license.

11. No Transfer of License: This license is personal to you and may not be sublicensed, assigned, or transferred by you to any other person without publisher's written permission.

12. No Amendment Except in Writing: This license may not be amended except in a writing signed by both parties (or, in the case of publisher, by CCC on publisher's behalf).

13. Objection to Contrary Terms: Publisher hereby objects to any terms contained in any purchase order, acknowledgment, check endorsement or other writing prepared by

you, which terms are inconsistent with these terms and conditions or CCC's Billing and Payment terms and conditions. These terms and conditions, together with CCC's Billing and Payment terms and conditions (which are incorporated herein), comprise the entire agreement between you and publisher (and CCC) concerning this licensing transaction. In the event of any conflict between your obligations established by these terms and conditions and those established by CCC's Billing and Payment terms and conditions, these terms and conditions shall control.

14. Revocation: Elsevier or Copyright Clearance Center may deny the permissions described in this License at their sole discretion, for any reason or no reason, with a full refund payable to you. Notice of such denial will be made using the contact information provided by you. Failure to receive such notice will not alter or invalidate the denial. In no event will Elsevier or Copyright Clearance Center be responsible or liable for any costs, expenses or damage incurred by you as a result of a denial of your permission request, other than a refund of the amount(s) paid by you to Elsevier and/or Copyright Clearance Center for denied permissions.

LIMITED LICENSE

The following terms and conditions apply only to specific license types:

15. **Translation**: This permission is granted for non-exclusive world **English** rights only unless your license was granted for translation rights. If you licensed translation rights you may only translate this content into the languages you requested. A professional translator must perform all translations and reproduce the content word for word preserving the integrity of the article. If this license is to re-use 1 or 2 figures then permission is granted for non-exclusive world rights in all languages.

16. **Website**: The following terms and conditions apply to electronic reserve and author websites:
Electronic reserve: If licensed material is to be posted to website, the web site is to be password-protected and made available only to bona fide students registered on a relevant course if:
This license was made in connection with a course,
This permission is granted for 1 year only. You may obtain a license for future website posting,
All content posted to the web site must maintain the copyright information line on the bottom of each image,
A hyper-text must be included to the Homepage of the journal from which you are licensing at http://www.sciencedirect.com/science/journal/xxxxx or the Elsevier homepage for books at http://www.elsevier.com , and
Central Storage: This license does not include permission for a scanned version of the material to be stored in a central repository such as that provided by Heron/XanEdu.

17. **Author website** for journals with the following additional clauses:

All content posted to the web site must maintain the copyright information line on the bottom of each image, and
he permission granted is limited to the personal version of your paper. You are not allowed to download and post the published electronic version of your article (whether PDF or HTML, proof or final version), nor may you scan the printed edition to create an electronic version,
A hyper-text must be included to the Homepage of the journal from which you are licensing at http://www.sciencedirect.com/science/journal/xxxxx , As part of our normal production process, you will receive an e-mail notice when your article appears on Elsevier's online service ScienceDirect (www.sciencedirect.com). That e-mail will include the article's Digital Object Identifier (DOI). This number provides the electronic link to the published article and should be included in the posting of your personal version. We ask that you wait until you receive this e-mail and have the DOI to do any posting.
Central Storage: This license does not include permission for a scanned version of the material to be stored in a central repository such as that provided by Heron/XanEdu.

18. **Author website** for books with the following additional clauses:
Authors are permitted to place a brief summary of their work online only.
A hyper-text must be included to the Elsevier homepage at http://www.elsevier.com

All content posted to the web site must maintain the copyright information line on the bottom of each image
You are not allowed to download and post the published electronic version of your chapter, nor may you scan the printed edition to create an electronic version.
Central Storage: This license does not include permission for a scanned version of the material to be stored in a central repository such as that provided by Heron/XanEdu.

19. **Website** (regular and for author): A hyper-text must be included to the Homepage of the journal from which you are licensing at http://www.sciencedirect.com/science/journal/xxxxx. or for books to the Elsevier homepage at http://www.elsevier.com

20. **Thesis/Dissertation**: If your license is for use in a thesis/dissertation your thesis may be submitted to your institution in either print or electronic form. Should your thesis be published commercially, please reapply for permission. These requirements include permission for the Library and Archives of Canada to supply single copies, on demand, of the complete thesis and include permission for UMI to supply single copies, on demand, of the complete thesis. Should your thesis be published commercially, please reapply for permission.

21. **Other Conditions**:

v1.6

Gratis licenses (referencing $0 in the Total field) are free. Please retain this printable license for your reference. No payment is required.

If you would like to pay for this license now, please remit this license along with your payment made payable to "COPYRIGHT CLEARANCE CENTER" otherwise you will be invoiced within 48 hours of the license date. Payment should be in the form of a check or money order referencing your account number and this invoice number RLNK10968676.

Once you receive your invoice for this order, you may pay your invoice by credit card. Please follow instructions provided at that time.

Make Payment To:
Copyright Clearance Center
Dept 001
P.O. Box 843006
Boston, MA 02284-3006

For suggestions or comments regarding this order, contact Rightslink Customer Support: customercare@copyright.com or +1-877-622-5543 (toll free in the US) or +1-978-646-2777.
